University of Nottingham
UK | CHINA | MALAYSIA

Computational Study on Polarisation Behaviour of Functionalised Endohedral Metallofullerenes

Thesis submitted to the University of Nottingham for the degree of
Doctor of Philosophy

Matthew Halstead

Supervised by

Professor Elena Besley
Professor Tony Stace

April 2023

Declaration

I hereby declare that the research in this thesis is the result of my own work, which has been undertaken during my period of registration for this degree at the University of Nottingham.

Matthew J. Halstead

Abstract

This work focused on investigating the potential for selected functionalised endohedral metallofullerene isomers to be viable candidates for a molecular polarisation switch, with a particular focus on the $Ca@C_{60}$ system. This work combines classical electrostatic analysis and Density Functional Theory (DFT) to investigate the correlation between the encapsulated calcium metal ion position and distribution of surface charge that results in polarisation on the fullerene cage. In addition, the modification of internal potential energy barriers through functionalisation of the fullerene cage was investigated as a route to developing a bistable polarisation switch.

A classical electrostatic analysis of a point charge within a dielectric sphere was undertaken to produce an analytical solution describing how the surface charge polarisation responds to the precise position of an encapsulated point charge. The analytical solution shows that for a positive point charge, the surface charge is attracted to the positive calcium ion as it is displaced across the fullerene cage, "following" the point charge across the cage. This was verified through DFT calculations on the $Ca@C_{60}$ system. This analytical solution was then extended to present an analytical solution for the case of a dipole inside an endohedral fullerene, verified through DFT calculations on $HF@C_{60}$.

Hydrogenated and fluorinated functionalised C_{60} candidates were selected for testing on the basis that these molecules could be experimentally produced with a reasonable degree of isomer specificity and selection. DFT computational parameters were rigorously tested against experimental evidence to ensure the calculations were "fit-for-purpose" using these parameters. DFT calculations provided insight into how functionalisation affects the internal potential energy barriers experienced by the encapsulated calcium. In particular, how an energy gap is created between minima in the Mexican-hat potential and how increasing degrees of functionalisation impact the position of the energy barriers within the fullerene cage. Partial charge analysis clearly demonstrated that the motion of the encapsulated calcium, confined within the selected functionalised fullerene cages, was strongly correlated to the distribution of charge density on the cage surface, with measurements of changes in surface charge polarisation.

Comparing and contrasting the candidate hydrogenated and fluorinated endohedral fullerenes against specific switching criteria enabled the selection of 1,2-Ca@$C_{60}H_2$ as the most promising candidate to develop a polarisation switch – a high yield functionalised endohedral fullerene with a sufficient and minimally shifted energy barrier and energy gap between minima that leads to a clearly defined change in surface charge polarisation. A potential route to scalability is discussed, through the creation of stable binary endohedral fullerene lattices that could lead to novel large-scale molecular switching arrays and nanomaterials with novel optical and electronic properties.

List of Publications

"Designing stable binary endohedral fullerene lattices"

A. Miller, M. Halstead, E. Besley and A. J. Stace, Physical Chemistry Chemical Physics, 2022, 24, 10044–10052.

Acknowledgements

I honestly can't quite believe I've got to the end... starting when I was fresh-faced and unmarried, and finishing eight years later, wooden anniversary celebrated with a four-year-old daughter. Undertaking this PhD alongside full-time work and family life has certainly tested my limits of perseverance, and I am truly grateful to my wife Thea who has been with me every step of the way – your patience, love, and kindness have no bounds. I am forever grateful to my Mum and Dad, who have always encouraged my curiosity and my grandmother, "Great Jeanno", who keeps reminding me that all we can do is our very best, but that best is not gifted, only achieved through hard work.

I would like to give my infinite thanks to my supervisors, Professor Elena Besley and Professor Tony Stace, for believing in me when I did not, and frankly for putting up with me for 8 years – I am ever grateful for their wise counsel, knowledge, and guidance that ultimately helped me crawl over the finish line.

I would like to dedicate this thesis to my daughter, Kairie, so when she is old enough to read, show her that a little curiosity, perseverance, imagination, and risk can take you on adventures you never thought possible...

Contents

Abbreviations

CHELPG Charges from the Electrostatic Potential on a Grid.
CM5 Charge Model 5.
DDEC Density Derived Electrostatic and Chemical.
DFT Density Functional Theory.
GGA General Gradient Approximation.
HF Hartree-Fock.
HK Hohenberg-Kohn.
HPLC High-Performance Liquid Chromatography.
ISC Inter-System Crossing.
JT Jahn-Teller.
KS Kohn-Sham.
LDA Local Density Approximation.
LSDA Local Spin Density Approximation.
LUMO Lowest Unoccupied Molecular Orbital.
NMR Nuclear Magnetic Resonance.
PES Photoelectron Spectroscopy.
SAMO Super-Atom Molecular Orbitals.
STO Slater-Type Orbital.
UHF Unrestricted Hartree-Fock.

Chapter 1

Introduction

This chapter provides an overview on the origins of nanotechnology, molecular switches, and endohedral fullerenes as potential candidates for a molecular switch. Research hypotheses are discussed in the final section.

1.1 Nanotechnology and molecular switches

Over the last six decades, computing technology has progressed quickly from room-sized computing machines to personal computers and handheld devices. The demand for computing power has increased exponentially, and with it, the need for ever-smaller computing components. The field of molecular electronics has successfully developed microscopic counterparts to macroscopic electronic components such as wires, switches, and transistors as a means to move beyond the current limits of semiconducting materials and technology that power current portable devices [1]. But can we go any smaller? Microscopic components at the nanometre scale open new possibilities to improve and innovate on the electronic systems that power our world.

The concept of nanotechnology was introduced in 1959 by Richard Feynman in his lecture, *"There's Plenty of Room at the Bottom"* [2], asking, *"why can't we write the entire 24 volumes of the Encyclopedia Britannica on the head of a pin?"* This lecture describes a vision of designing ever-smaller machines down to the molecular level. In 1974, Norio Taniguchi, was the first person to use the term *"nanotechnology"* describing the field as *"mainly consisting of the processing of separation, consolidation, and deformation of materials by one atom or molecule"* [3]. Nanotechnology has become a leading scientific field in academia and industry – the National Nanotechnology Initiative (NNI) in the United States of America defines Nanotechnology as *"science, engineering, and technology conducted at the nanoscale (1 to 100 nm), where unique phenomena enable novel applications in a wide range of fields, from chemistry, physics and biology, to medicine, engineering, and electronics"* [4]. At the nanometre scale, the properties of matter differ significantly from macroscopic states due to quantum effects. At this level, electrostatic, quantum and Brownian motion dominate interactions and so the design of molecular systems with precisely defined translational and rotational motion is the main challenge for those working to create molecular electronics to improve the efficiency and effectiveness of novel micro-electronic systems [5].

One of these micro-electronic components are molecular switches. A molecular switch influences the state of a molecular system, switching between two or more, often equilibrium, states [6]. Molecular switches show promise in the field of data storage as an innovation to supersede and miniaturise silicon technologies that currently require millions of atoms to store one binary bit of information. Several atoms and molecular structures that facilitate the toggling between two states, for example, between magnetic, electronic or polarisation states, have demonstrated the potential to store

single bits of information across individual atoms or molecules [1, 7–13]. These innovations could lead to significant increases in data storage density and capacity. State switching is also vital for the implementation of logic gates within classical and quantum computing systems [14] operating on bits and qubits to perform logical functions. Quantum computing components by their nature must be small enough to operate within the quantum scale, and so molecular switches are important components to manipulate information at the quantum level.

Operating at the quantum scale requires intricate experimental setups that minimise external "noise" that naturally interfere with fragile quantum systems. Endohedral fullerenes, and in particular, endohedral metallofullerenes, have shown particular promise over other molecules due to their stable carbon shells that shield the encapsulated species and allow the trapped species to be manipulated without compromising molecular integrity [15–18], whilst retaining some degree of quantum character. Wave-particle duality has been observed in C_{60} molecules by diffraction at a material absorption grating [19] making it an exciting choice of molecule to study at the boundary of quantum and classical mechanics.

The C_{60} "Buckminsterfullerene" molecule, was discovered in 1985 as a by-product of experiments aimed at understanding the mechanisms that form long-chain carbon molecules in interstellar space and circumstellar shells [20]. Laboratory experiments, attempting to replicate these interstellar processes, produced a 60-carbon atom structure *"arranged in a truncated icosahedral structure of 60 vertices and 32 faces, 12 of which are pentagonal and 20 hexagonal"*. One week after the discovery of C_{60}, a group at Texas University obtained evidence that a single lanthanum atom could be trapped inside the carbon shell [21]. This endohedral metallofullerene was produced in small quantities by laser evaporation of a graphite target

impregnated with $LaCl_3$. In 1990 an arc reactor, using arc-discharge between two graphite rods, produced a meaningful quantity of solid C_{60} [22]. Since this discovery an enormous amount of research has been undertaken to understand the properties of C_{60} and its derivatives with a large body of research, both experimental and theoretical, focusing on doping fullerene cages with metals [21, 23–32].

An example of an endohedral metallofullerene molecular switch is $Gd@C_{82}$, recently observed as a gate-controlled single-molecule electret switch between two electronic states [33]. An electret is a dielectric material that has a quasi-permanent dipole polarisation. A single-molecule electret is a highly desirable molecule that can be applied to miniaturised non-volatile memory storage devices, switching between two electric dipole states through the action of an electric field. However, single-molecule electrets are difficult to produce, as single molecules often possess poor electric stabilisation properties and configurations. In the case of $Gd@C_{82}$, experimental and computational research has demonstrated the significant advantage of the fullerene cage as it shields and stabilises an electric dipole from external interference, enabling two electric dipole states to exist at different sites within the cage, separated by a transition energy barrier of 11 meV.

1.2 Polarisation charge switching in $Ca@C_{60}$

$Ca@C_{60}$ was first produced for study in 1993 following the production of macroscopic quantities of the metallofullerene $La@C_{60}$ by laser vaporisation of a La_2O_3/graphite composite rod in a high temperature tube furnace [34]. $Ca@C_{60}$ was similarly produced using the laser vaporisation / high temperature furnace technique using a CaO/graphite composite rod. The authors

note the CaO concentration (0.3% by atom) in the composite rod was crucial to achieving an abundant yield of Ca@C_{60}. Since 1993 there has been continued research on metallofullerenes, however, only recently has research into Ca@C_{60} moved away from academia to understand its chemical properties, and towards potential applications in the field of molecular switches [17, 35]. Computational studies have greatly assisted in predicting the electronic properties of Ca@C_{60}. Spin-polarised and self-consistent calculations by Broclawik et al. [36] predicted a neutral electronic configuration of $a_{1g}^{0.5}t_{1u}^{1.5}$ and a charge of +1.27 on the calcium ion. The non-integer partial charge in the above calculations is interpreted as a degree of delocalisation and overlap of the fullerene electron density and central atom, which results in a small "back-donation" effect. This "back-donation" effect was also noted by Srivastava et al. in a comparative DFT study of Li@C_{60} and F@C_{60} [37]. Restricted Hartree-Fock calculations performed in 1991 by Chang et al.[24], using relativistic effective core potentials with the icosahedral symmetry (I_h), predicted an electronic ground state of Ca@C_{60} to be the triplet $^3T_{1u}$ ($a_g^1t_{1u}^1$, where the a_g orbital is from the Ca 4s orbital and t_{1u} is the C_{60} LUMO) [34]. However, this prediction was inconsistent with Photoelectron Spectroscopy (PES) spectra, produced by Wang et al. [30], which showed that unless the a_g and t_{1u} orbitals are degenerate, a $a_g^1t_{1u}^1$ configuration would result in two separate peaks in the PES spectra which was not observed. To counter this, Wang et al. performed Hartree Fock calculations that predicted the ground state of Ca@C_{60} to be a triplet $^3A_2$ (e_1^2) state. These calculations also showed that the valence 4s electrons of the encapsulated calcium ion are energetically close to the LUMO of C_{60} which allows the transfer of none, one or both 4s electrons to the C_{60} cage. In this case, they found that for the triplet $^3A_2$ state, both calcium 4s electrons were transferred to the carbon shell to form $Ca^{2+}@C_{60}^{2-}$, and the calcium ion located 0.7 Å from the centre of the fullerene cage, a reduced

symmetry of C_{5v}. A further study by Lu et al. [26] using I_h symmetry with the calcium located at the cage centre, predicted a net charge distribution of $Ca^{1.67+}@C_{60}^{1.67-}$. The authors noted the possibility that the ground state may be of a lower symmetry because of Jahn-Teller (JT) distortion. The Jahn-Teller theorem states that a degenerate state for a non-linear molecule is unstable against non-symmetric molecular vibrations. C_{60} was found to become JT-active upon addition or removal of one electron, which suggests that the encapsulation of a species that adds or removes one electron from C_{60} result in a Jahn-Teller distortion. Consequently, the calcium naturally adopts an off-centre position to remove this Jahn-Teller instability. Raggi et al. performed Density Functional Theory (DFT) calculations on $Ca@C_{60}$ in 2014 at the B3LYP / 6-31G* [38–41] level of theory and found the electronic ground state to be the triplet state, reinforcing previous findings, with calcium located at a radial distance of 1.22 Å from the centre of C_{60} and facing the midpoint of an edge between two adjacent hexagons [35].

Property	**Ground-state**
Electronic configuration	$^3A_2$ (e_1^2)
Symmetry	C_{5v}
Calcium partial charge	1.27e – 2.00e
Calcium position	0.70 Å - 1.22 Å

Table 1.1: Literature summary of $Ca@C_{60}$ ground state electronic and geometric properties

It is clear from the literature that results are sensitive to the level of theory adopted by researchers, however, in general there exists a good amount of evidence to conclude that the encapsulation of a metal atom leads to electron transfer to the cage, resulting in a metal cation located at an off-centre position with respect to the fullerene cage. The potential energy surface within $Ca@C_{60}$ takes the form of a "Mexican-hat" with the cation

confined within a potential well at the ground-state minimum position. This has implications for $Ca@C_{60}$, firstly that the free radial motion may give rise to a low-frequency rattling mode, as the calcium moves around the potential well, which could be observed using infrared and Raman spectroscopy [23].

The facilitation of charge switching through the motion of atomic or molecular species has been demonstrated for an Sc_3N cluster encapsulated within a fullerene cage [8] which Raggi et al. suggested extending by controlling the state of an encapsulated species within a fullerene cage by means of electronic or optical stimulation. $Ca@C_{60}$ is a particularly interesting system because the calcium ion has an optical transition at 397 nm [42] making it readily accessible using laser radiation. Recent research focusing on $Li@C_{60}$ [1, 43] demonstrated that resonant tunnelling via the super-atom molecular orbitals (SAMO) resulted in the display of 14 molecular states which could be statistically accessed. In addition, another design for a molecular switch using endohedral fullerenes has been proposed by Foroutan-Nejad et al. [16] - applying an external electric field to a range of dipolar molecules (NaF, NaCl, LiCl and LiF) encapsulated within C_{70} at room-temperature to switch between two bi-stable molecular dipole states, being two distinct potential energy minima locations within the fullerene cage.

Polarisation charge switching, the focus of this research, was predicted to occur in $Ca@C_{60}$ through the motion of the calcium ion trapped in the fullerene cage [17]. As discussed above, endohedral metallofullerene formation leads to charge transfer from the metal atom to the fullerene cage, resulting in a positively charged encapsulated metal ion that influences the distribution of charge density on the fullerene cage through electrostatic interactions. A preliminary analytical form of the polarised charge distribution was proposed through classical electrostatic modelling of the surface

charge on a dielectric sphere due to the presence of an external point charge [44]. In this configuration, the solution describes how the sphere's surface charge is polarised into regions of positive and negative charge due to the presence of an external point charge. The degree of polarisation was found to vary as a function of the separation between the dielectric sphere and the charge, particularly significant at very short separations. This led to the hypothesis that an encapsulated charge would also produce similar polarisation effects. The external charge solution was in qualitative agreement with DFT calculations reported in the same paper, accurately predicting the form of surface charge polarisation on C_{60} and C_{240} fullerene cages due to the presence of an external point charge. This led to the conclusion that from an electrostatic point of view, C_{60} and C_{240} are dielectric in character. This is juxtaposed by an earlier paper concluding that the most accurate analytical solution to describe the electronic response of C_{60} is found using a metallic sphere model [45]. A further study exploring polarisation charge switching through the motion of metal atoms trapped in fullerene cages, supported by DFT calculations, showed that for a charge encapsulated within C_{60} "*the sign and magnitude of the polarisation response depend very strongly on the precise position of the ion trapped inside the encapsulating cage.*" [17]. These insights led to the idea that exploitation of calcium ion motion, being strongly correlated to the distribution of surface charge density on the fullerene cage, could lead to a promising design for a polarisation molecular switch.

To create a switching environment, an experiment would need to precisely control the motion of the encapsulated metal ion. It was previously proposed through DFT analysis [35] that tethered and functionalised metallofullerenes qualify as suitable candidates for a bi-stable molecular switch through hydrogen or fluorine atom addition on one hemisphere of

the fullerene cage surface. Functionalisation was found to significantly reduce the internal energy barriers with respect to the translational motion of the calcium ion, enabling the encapsulated ion to be restricted to a single hemisphere and then stimulated into the other hemisphere, leading to a measurable change in surface charge polarisation. Raggi showed that "*changes in electronegativity accompanying a transition in hybridization for carbon from sp^2 to sp^3 influence the interaction between the calcium atom and the fullerene cage*". In particular, the addition of hydrogen or fluorine increases the number of sp^3 hybrid carbons on the cage surface, leading to extensive modifications to the internal potential energy profile - changing the relative stability between bi-stable states or even removing the barrier completely - depending on the isomer or configuration chosen. The polarisation effects appeared to be driven by the significant reduction in electronegativity of the sp^3 hybrid carbons, reducing the degree of electron donation from the calcium atom which leads to a diminished attractive electrostatic interaction between the calcium ion and the fullerene cage, responsible for the creation of the internal potential energy barriers.

Observing these effects across multiple isomers of $Ca@C_{60}H_4$, the difference in the degree of polarisation response to the motion of a calcium atom appeared to be as a consequence of the presence or absence of sp^3 carbon atoms, their positions on the cage and the influence they have on electron-acceptance as the calcium moved across the cage. These insights led to a second hypothesis that appropriately selected functionalised endohedral fullerene isomers could form the basis of a polarisation switch due to the symmetry breaking of internal energy barriers (with respect to motion) as a response to functionalisation.

Whilst there is significant interest in designing a single molecule switch, the idea that these switches could be scaled up to multi-molecular switches

as part of a larger more complex switching system or array is a fascinating thought experiment, with potential applications to memory devices and molecular transistors to achieve novel logic gates [1, 17]. Recent work by Miller et al. [46] (including DFT calculation contributions from this author) proposed designs for stable nanoparticle lattices composed of binary collections of endohedral fullerenes. The calculations involved a combination of van der Waals and many-body electrostatic interactions to predict that certain binary combinations, for example a metal (A) and a halogen (B), could result in the formation of stable nanoparticle lattices with familiar AB and AB_2 stoichiometries. Much of the stability was found to be due to Coulomb interactions, however, charge-induced and van der Waals interactions, which always enhance stability, were found to extend the range of charge on a cage over which lattices were stable with some lattice types shown to be three or four times more stable than an equivalent neutral C_{60} structure. Consequently, the optical and electronic properties of endohedral fullerenes, including polarisation switching, could be incorporated into new materials fabricated into the regular lattice structures known to be adopted by nanoparticles [47–49].

Giminez-Lopez et al. [50] also demonstrated the insertion of multiple functionalised endohedral fullerenes into single-walled carbon nanotubes. A fascinating and useful insight of this work was the observation that "*the endohedral Sc_3N cluster exhibits near free rotation in an unmodified $Sc_3N@C_{80}$, but when a functional group is attached to the C_{80} cage, the rotation of Sc_3N is more restricted*". This provides further evidence of the findings by Raggi et al. that functionalisation modifies the internal potential energy barriers, thus restricting the internal motion of the encapsulated species.

1.3 Research hypotheses

This thesis investigates and tests the validity of two hypotheses:

- That the motion of an encapsulated metal confined within a fullerene cage is strongly correlated to the distribution of charge density on the cage surface.
- That appropriately selected functionalised endohedral fullerene isomers could form the basis of a polarisation switch.

This work represents eight years of part-time research across three research projects, (1) the classical electrostatic analysis of surface charge for metallofullerenes, (2) computational validation of $Ca@C_{60}$ polarisation properties and (3) polarisation properties of hydrogenated and fluorinated metallofullerenes.

This thesis is organised into six chapters; this chapter, Chapter 1, provides an introduction into nanotechnology and endohedral fullerenes, particularly $Ca@C_{60}$, in the context of designing a viable molecular switch. Chapter 2 discusses the theoretical methods used in this research, being computational quantum chemical methods, particularly Density Functional Theory, and analytical classical electrostatics. The combination of classical electrostatic analysis and quantum chemical analysis, aligned to experimental evidence, is used to give confidence that the results and conclusions presented in this thesis are robust and valid. Chapter 3 presents an electrostatic analytical solution of a point charge within a dielectric particle as a basis for modelling the surface charge polarisation for metallofullerenes. This chapter is presented first to give the reader a good mental picture of $Ca@C_{60}$ in the context of a potential polarisation switch, before diving into the depths

of the quantum chemical analysis and results. Chapter 4 delves into the literature to select specific hydrogenated and fluorinated fullerene isomers as candidates for a functionalised $Ca@C_{60}$ polarisation switch and then presents the process to derive robust and validated computational parameters for the $Ca@C_{60}$ system, with the final section providing DFT calculated properties relevant to polarisation. Chapter 5 uses the defined computational parameters to predict a range of polarisation properties across the selected hydrogenated and fluorinated $Ca@C_{60}$ isomers. The hydrogenated and fluorinated molecules are then compared with recommendations as to which specific functionalised $Ca@C_{60}$ molecule would be the most viable choice for a polarisation switch. The final section in Chapter 5 then discusses recent work undertaken to predict stable nanoparticle lattices with a view to scaling up an endohedral molecular switch into a multi-molecular switching system. Chapter 6 explores how the analytical solution presented in Chapter 3 can be extended for the case of a dipole inside an endofullerene with a particular focus on $HF@C_{60}$, acknowledging recent active research activity in the study of dipolar endohedral fullerenes.

Chapter 2

Theoretical methods

This chapter introduces the theoretical methods used in this research – Density Functional Theory (computational) and classical electrostatics (analytical).

2.1 Introducing quantum chemical methods

Understanding the electronic properties of encapsulated materials is crucial for many industrial applications. These properties are often derived from the quantum mechanical analysis of a molecule's electronic structure using computational methods. But what exactly do these methods do?

The main goal of most quantum chemical approaches is to find an approximate solution of the time-independent and non-relativistic Schrödinger equation [51] described in Eq. (2.1) in compacted form:

$$\widehat{H}\Psi(\{\mathbf{r}_i\},\{\mathbf{R}_I\}) = E\Psi(\{\mathbf{r}_i\},\{\mathbf{R}_I\}) \tag{2.1}$$

where the wave function, Ψ contains all information about the quantum system which depends on 3N spatial coordinates of the electrons $\mathbf{r_i}$ and 3M spatial coordinates of the nuclei, $\mathbf{R_I}$. $\widehat{H}$ is the Hamiltonian differential operator for a molecular system of M nuclei and N electrons, in the absence of magnetic or electric fields:

$$\widehat{H} = -\frac{1}{2}\sum_{i=1}^{N}\nabla_i^2 - \frac{1}{2}\sum_{A=1}^{M}\frac{1}{m_A}\nabla_A^2 - \sum_{i=1}^{N}\sum_{A=1}^{M}\frac{Z_A}{r_{iA}} + \sum_{i=1}^{N}\sum_{j>i}^{N}\frac{1}{r_{ij}} + \sum_{A=1}^{M}\sum_{B>A}^{M}\frac{Z_A Z_B}{R_{AB}} \tag{2.2}$$

The first two terms of the Hamiltonian operator describe the kinetic energy of the electrons and nuclei, respectively. m_A is the mass of a nucleus A in multiples of the mass of an electron (in atomic units – explained below). A and B run over the M nuclei while i and j denote the N electrons in the system. The Laplacian operator ∇^2 is the sum of differential operators in Cartesian coordinates:

$$\nabla^2 = \frac{\partial^2}{\partial x^2} + \frac{\partial^2}{\partial y^2} + \frac{\partial^2}{\partial z^2} \tag{2.3}$$

The additional three terms in Eq. (2.2) define the potential part of the Hamiltonian. From left to right, (1) the attractive electrostatic interaction between the nuclei and electrons, (2) the repulsive potential due to the electron-electron interaction and (3) the repulsive potential due to the nucleus-nucleus interaction, where Z is the nuclear charge on each respective nucleus in the system. In these expressions, r and R represent the distance between electrons, i and j and nuclei, A and B respectively, where $r_{ij} = |\mathbf{r_i} - \mathbf{r_j}|$ as an example. Figure 2.1 visualises a molecular system for the case of M=2 nuclei and N=2 electrons as an example:

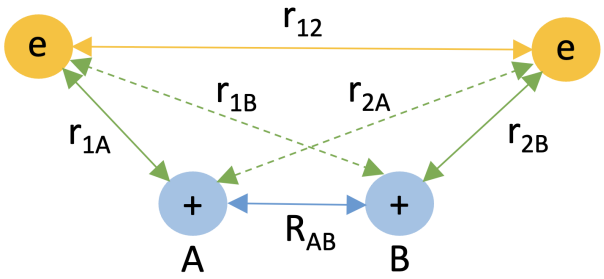

Figure 2.1: Geometric representation of an M=2 nuclei and N=2 electron molecular system, showing the distances relevant to the time-independent and non-relativistic Schrödinger equation.

The compacted form of the time-independent and non-relativistic Schrödinger equation and its parameters are described in atomic units. In this system the mass of an electron m_e, the modulus of electron charge $|e|$, Planck's constant h divided by 2π and the permittivity of a vacuum $4\pi\epsilon_0$ are all set to unity. Physical quantities such as mass and charge are expressed as multiples of these constants and are therefore dropped from the equations [51].

The approximate solutions to Eq. (2.1) enable the calculation of E_i, the numerical value of the energy of the system state described by Ψ_i. It should be noted that solving the time-independent and non-relativistic Schrödinger equation calculates the lowest energy and therefore most stable configuration of the system, known as the "ground-state" which enable the calculation of ground-state chemical properties.

The Schrödinger equation can be simplified by taking advantage of the significant differences between the masses of nuclei and electrons. Given the nuclei weigh so much more than electrons, they consequently move much slower and so, in the extreme case, a good approximation is that the nuclei are static, and the electrons move in a field of fixed nuclei. This is known as the Born-Oppenheimer approximation. In this approximation, if the nuclei are fixed, then their kinetic energy is zero and the repulsion due

to nuclei-nuclei repulsion is a constant. This enables the Hamiltonian to be reduced to what is known as the electronic Hamiltonian [51].

$$\widehat{H}_{elec} = -\frac{1}{2}\sum_{i=1}^{N}\nabla_i^2 - \sum_{i=1}^{N}\sum_{A=1}^{M}\frac{Z_A}{r_{iA}} + \sum_{i=1}^{N}\sum_{j>i}^{N}\frac{1}{r_{ij}} = \widehat{T} + \widehat{V}_{Ne} + \widehat{V}_{ee} \tag{2.4}$$

Note that V_{Ne} is also known as the external potential, V_{ext} in Density Functional Theory (DFT), discussed later. The solution to the electronic Schrödinger equation is Ψ_e, the electronic wave function dependent on just the electron coordinates and E_e, the electronic energy:

$$\widehat{H}_e\Psi_e(\{\mathbf{r}_i\}) = E_e\Psi_e(\{\mathbf{r}_i\}) \tag{2.5}$$

Under the Born-Oppenheimer approximation, the total energy of the system is the sum of E_e and the now constant nuclear repulsion term, $E_n = \sum_{A=1}^{M}\sum_{B>A}^{M}\frac{Z_A Z_B}{R_{AB}}$:

$$E_{tot} = E_e + E_n \tag{2.6}$$

Please note that given that the remainder of this section will focus on the calculation of the electronic Hamiltonian and associated electronic energies, the subscript "e" will be dropped from now on.

Given the wave function is not itself observable, a physical interpretation can only be achieved by the modulus squared, $|\Psi|^2$ which represents the probability that electrons $1, 2, ..., N$ are found simultaneously in a volume element $d\tau$ that contain three spatial coordinates and one spin coordinate. As electrons are indistinguishable, this probability must be the same if the

coordinates of any two electrons (i and j) switch. It can be shown that the only possibilities occurring in nature are symmetric wave functions (applies to particles known as bosons with integer or zero spin) or wave functions where the switch results in a sign change, known as an antisymmetric wave function (applies to particles known as fermions with spin =1/2). Given electrons are fermions, their wave functions must be antisymmetric with respect to the interchange of spatial and spin coordinates [51]. This is known as the antisymmetry principle, which generalises Pauli's exclusion principle that no two electrons can occupy the same space at the same time. The consequence of this probabilistic interpretation is that the probability of finding the N electrons in space must be exactly unity:

$$\int |\Psi|^2 \, d\tau = 1 \tag{2.7}$$

A wave function that satisfies Eq. (2.7) is said to be *normalised*. From now on, all wave function descriptions shall be exclusively normalised wave functions.

In order to calculate the molecular energy, the electronic Schrödinger equation is simply rearranged with the respective components and integrated with respect to the volume element $d\tau$ that contains the three spatial coordinates and one spin coordinate, calculated by:

$$E = \frac{\int \Psi^* \widehat{H} \Psi d\tau}{\int \Psi^* \Psi d\tau} \tag{2.8}$$

Given that normalised wave functions are now being exclusively used, the denominator becomes unity and so:

$$E = \int \Psi^* \widehat{H} \Psi d\tau \tag{2.9}$$

Or more conveniently expressed through Dirac notation:

$$E = \left\langle \Psi \left| \widehat{H} \right| \Psi \right\rangle \tag{2.10}$$

Aside from a few simple exceptions, there is currently no known strategy to solve the electronic Schrödinger equation exactly for large molecular systems due to the enormously challenging task of finding exact wave functions (eigenfunctions) and the associated energies (eigenvalues) of the electronic Hamiltonian that enable the calculation of the properties of the molecular system. In practice, this would require searching through all acceptable wave-functions that result in the true ground state of the molecular system, which is currently practically impossible. However, a strategy known as the "*variational principle*" simplifies this challenge by enabling a systematic approach to find the wave function that approaches the ground state Ψ_0 that results in the lowest energy for the system E_0. The variational principle states that the energy computed as the expectation value of $\widehat{H}$ from any guessed wave function Ψ_{trial} will always be an upper bound to the true ground state energy [51]:

$$\langle \Psi_{trial} \left| \widehat{H} \right| \Psi_{trial} \rangle = E_{trial} \geq E_0 = \langle \Psi_0 \left| \widehat{H} \right| \Psi_0^* \rangle \tag{2.11}$$

Therefore, using the variational principle, the strategy required to solve the electronic Schrödinger equation becomes the requirement to minimize the functional $E[\Psi]$ by searching through all acceptable N-electron wave functions. Note that "*acceptable*" in this context means that the trial wave

functions need to satisfy certain criteria to ensure they make physical sense. The functional that gives the lowest energy will be Ψ_0 and the energy will be the true ground state energy E_0 [51] described succinctly in Eq. (2.12).

$$E_0 = min_{\Psi \to N} E[\Psi] = min_{\Psi \to N} \left\langle \Psi \left| \widehat{T} + \widehat{V}_{Ne} + \widehat{V}_{ee} \right| \Psi \right\rangle \tag{2.12}$$

In practice, "*searching across all acceptable wave functions*" is almost impossible, however, the variational principle can be applied to subsets of possible functions to find the best approximation to the exact wave function. Note that the exact wave function is unlikely to be found, unless it is part of the subset, which is unlikely. One of these approximations is known as the Hartree-Fock approximation that is the foundation of Hartree-Fock (HF) theory, where the subset of functions consists of all antisymmetric products composed of N spin orbitals [51].

In summary, once the number of electrons N and V_{ext} are known (determined by Z_A and R_A) the electronic Hamiltonian $\widehat{H}$ can be constructed. Through the variational method described in Eq. (2.12) the ground state approximate wave function can be obtained which enables the determination of the ground state energy and all other system properties, shown as the summarised logical flow:

$$\{N, Z_A, R_A\} \Rightarrow \widehat{H} \Rightarrow \Psi_0 \Rightarrow E_0 \tag{2.13}$$

Since the 1930s computational methods have been developed to approximately solve the electronic Schrödinger equation, beginning with HF theory [52] and progressing to post-HF methods such as Møller–Plesset Perturbation Theory [53], configuration interaction methods [54] and DFT, the

quantum chemical tool used in this research. HF theory will be discussed to introduce the key ideas that laid the foundation for DFT [51].

2.1.1 Hartree-Fock theory

Hartree-Fock (HF) theory was developed to solve the electronic Schrödinger equation under the Born-Oppenheimer approximation. HF is the cornerstone of almost all wave function based quantum chemical methods [51] and is known as an "*ab initio*" (from the beginning) method as all wave function solutions are calculated from first principles without using experimental data. In the HF scheme, the simplest and physically robust approximation to the exact N-electron wave function is known as the Slater determinant [51]. The Slater determinant is an "*antisymmetrised*" product of one-electron wave functions taking into account the antisymmetry principle, more commonly known as the Pauli principle:

$$\Psi_0 \approx \Phi_{SD} = \frac{1}{\sqrt{N!}} \begin{vmatrix} \psi_1(1) & \psi_2(1) & ... & \psi_N(1) \\ \psi_1(2) & ... & ... & ... \\ ... & ... & ... & ... \\ \psi_1(N) & \psi_2(N) & ... & \psi_N(N) \end{vmatrix} \tag{2.14}$$

where N is the number of electrons and $\psi_1, ..., \psi_N$ are the one-electron molecular orbitals known as spin orbitals containing a spatial orbital and one of two spin functions α or β [51].

$$\psi_i(k) = \psi_i(\mathbf{r}_k)\sigma(\omega_k) \qquad \sigma = \alpha, \beta \tag{2.15}$$

where $\mathbf{r}$ are the spatial coordinates, ω is the spin coordinate and $\psi_i(k)$

relates to the i'th molecular orbital that depends on the coordinates of the k'th electron. The spin orbitals have a special property that they are orthonormal, i.e. $< \alpha \mid \alpha >=< \beta \mid \beta >= 1$ and $< \alpha \mid \beta >=< \beta \mid \alpha >= 0$ which is generalised to equate to $< \Psi_i(k) \mid \Psi_j(k) >= \delta_{ij}$ which equals 1 for i=j and 0 otherwise [51].

Now the form of the wave function has been selected, the next step is to find the best Slater determinant that provides the lowest energy. The HF approach varies the spin orbitals under the constraint that they remain orthonormal so that the energy obtained is minimised.

$$E_{HF} = min_{\Phi_{SD} \to N} E[\Phi_{SD}] \tag{2.16}$$

The determination of the HF energy, the expectation value of the Hamiltonian operator, can be derived by substituting in the Slater determinant Eq. (2.14) and the electronic Hamiltonian (2.4) into Eq. (2.10), the final result shown in Eq. (2.17).

$$E_{HF} = \left\langle \Phi_{SD} \left| \widehat{H} \right| \Phi_{SD} \right\rangle = \sum_{i}^{N} (i \left| \widehat{h} \right| i) + \frac{1}{2} \sum_{i}^{N} \sum_{j}^{N} (ii \mid jj) - (ij \mid ji) + V_{nn} \tag{2.17}$$

comprising $(i \left| \widehat{h} \right| i)$, the kinetic energy and nuclear-electron attraction integral, $(ii \mid jj)$ known as the Coulomb integral and $(ij \mid ji)$, known as the exchange integral, and the nuclear repulsion term V_{nn} to calculate the kinetic, Coulomb, exchange and nuclear energies respectively. The Coulomb and exchange components relate to the interaction between two electrons. As mentioned previously, under the Born-Oppenheimer approximation the nuclear repulsion term is calculated separately and then added

(Eq. (2.6)) after the electronic energy has been calculated. The kinetic, nuclear-electron attraction, Coulomb, and exchange integrals are defined further in equations (2.18), (2.19), and (2.20).

$$(i \left|\widehat{h}\right| i) = \langle \psi_i \left| h \right| \psi_i \rangle = \int \psi_i^*(\mathbf{r}) \left(-\frac{1}{2}\nabla_i^2 - \sum_A \frac{Z_A}{r_{Ai}} \right) \psi_i(\mathbf{r}) d\mathbf{r} \tag{2.18}$$

$$(ii \mid jj) = \int\int \frac{\psi_i^*(\mathbf{r}_1)\psi_i(\mathbf{r}_1)\psi_j^*(\mathbf{r}_2)\psi_j(\mathbf{r}_2)}{r_{12}} d\mathbf{r}_1 d\mathbf{r}_2 \tag{2.19}$$

$$(ij \mid ij) = \int\int \frac{\psi_i^*(\mathbf{r}_1)\psi_j(\mathbf{r}_1)\psi_j^*(\mathbf{r}_2)\psi_i(\mathbf{r}_2)}{r_{12}} d\mathbf{r}_1 d\mathbf{r}_2 \tag{2.20}$$

Rewriting Eq. (2.17) in terms of the Coulomb and exchange operators leads to:

$$E_{HF} = \sum_{i=1}^{N} \langle \psi_i \left| h \right| \psi_i \rangle + \frac{1}{2} \sum_{i}^{N} \left\langle \psi_i \left| \widehat{J} - \widehat{K} \right| \psi_i \right\rangle \tag{2.21}$$

where the Coulomb operator J represents the potential that an electron at the position $\mathbf{r}$ experiences as a result of the average charge distribution of another electron in spin orbital ψ_j and is defined as:

$$\widehat{J}\psi_i(1) = \sum_j \int \frac{\psi_j^*(2)\psi_j(2)}{r_{12}} d\mathbf{r}_2 \psi_i(1) \tag{2.22}$$

and the exchange operator K, which has no classical interpretation, rather interpreted through its effect when operating on a spin orbital [51] is defined as:

$$\widehat{K}\psi_i(1) = \sum_j \int \frac{\psi_j^*(2)\psi_i(2)}{r_{12}} d\mathbf{r}_2 \psi_j(1) \tag{2.23}$$

Applying the variational principle to equations (2.21), (2.22) and (2.23) results in the HF equations which determine the spin orbitals for which E_{HF} yields the lowest value.

$$\widehat{F}\psi_i(\mathbf{r}) = \epsilon_i\psi_i(\mathbf{r}) \qquad i = 1, 2, ..., N. \tag{2.24}$$

where

$$\widehat{F}(1) = h(1) + \widehat{J} - \widehat{K} \tag{2.25}$$

$\widehat{F}$ is a one-electron operator known as the Fock operator and ϵ_i are Lagrangian multipliers, the eigenvalues of the Fock operator representing orbital energies. $\widehat{J} - \widehat{K}$ is known as the HF potential V_{HF}, the average repulsive potential experienced by the i'th electron due to the remaining N-1 electrons [51].

The HF equations (Eq. (2.24) and (2.25)) are known as pseudoeigenvalue equations as the Fock operator is not dependent on ψ_i on which it acts, rather depends through the HF potential on the spin orbitals i.e. it depends on the solutions of the eigenvalue problem that needs to be solved. This circular consequence means that the equations cannot be solved in closed form, rather through an iterative approach that is known as the "*self-consistent field*" (SCF) procedure. The SCF technique starts with a first "*guessed*" set of orbitals, that are derived from their own effective potential, and are used to solve the HF equations to produce a new set of orbitals that are then used as the inputs for the next HF energy calculation iteration. This is repeated until the input and output orbitals differ by less than a predetermined threshold, known as the convergence threshold [51].

However, the initial guessed set of molecular orbitals are a complicated mathematical and physical problem unto themselves. In 1951 Roothaan [55] and Hall [56] proposed that this problem could be solved by introducing a finite basis set to expand the molecular orbitals. These finite basis sets are linear combinations of known functions called basis functions:

$$\psi_i = \sum_{\alpha}^{N_b} c_{\alpha i}\chi_\alpha \tag{2.26}$$

where ψ_i is the i'th molecular orbital, $c_{\alpha i}$ is the coefficient of the α'th basis function of the i'th molecular orbital and χ_α is the α'th basis function and N_b is the number of basis functions. Basis functions usually reside on atoms, and the coordinates of the atomic nucleus defines the molecular coordinates. As each basis function can be regarded as a type of atomic orbital, the linear combination of basis functions is often known as the linear combination of atomic orbitals (LCAO) representation of molecular orbitals.

Using this Roothaan-Hall approach, Eq. (2.26) can be substituted into the HF equation Eq. (2.24):

$$\sum_{\alpha}^{N_b} c_{\alpha i}\mathbf{F}\chi_\alpha = \epsilon_i \sum_{\alpha}^{N_b} c_{\alpha i}\chi_\alpha \tag{2.27}$$

Given $\mathbf{F}$ only operates on χ and not c, multiplying by χ_β and integrating provides the Roothaan-Hall version of the HF equations:

$$\sum_{\alpha}^{N_b} c_{\alpha i}(F_{\beta\alpha} - \epsilon_i S_{\beta\alpha}) = 0, \qquad \beta = 1, 2, ..., N_b \tag{2.28}$$

which can be written in matrix notation:

$$\mathbf{FC} = \mathbf{SC}\epsilon \tag{2.29}$$

where $S_{\beta\alpha} = \langle \chi_\beta \mid \chi_\alpha \rangle$ is the basis functions overlap matrix, C is the matrix containing coefficients $c_{\alpha i}$, ϵ is a diagonal matrix of the orbital energies and $F_{\beta\alpha} = \left\langle \chi_\beta \left| \widehat{F} \right| \chi_\alpha \right\rangle$ with $\widehat{F}$ being the Fock operator.

The Roothaan-Hall equations can be solved using the SCF approach mentioned previously and use a basis set to calculate the coefficients c to determine (via the LCAO approach), the molecular orbitals ψ and energy levels ϵ. The SCF iterative procedure, applied to the Roothaan Hall equations, is shown in the flow diagram, Figure 2.2.

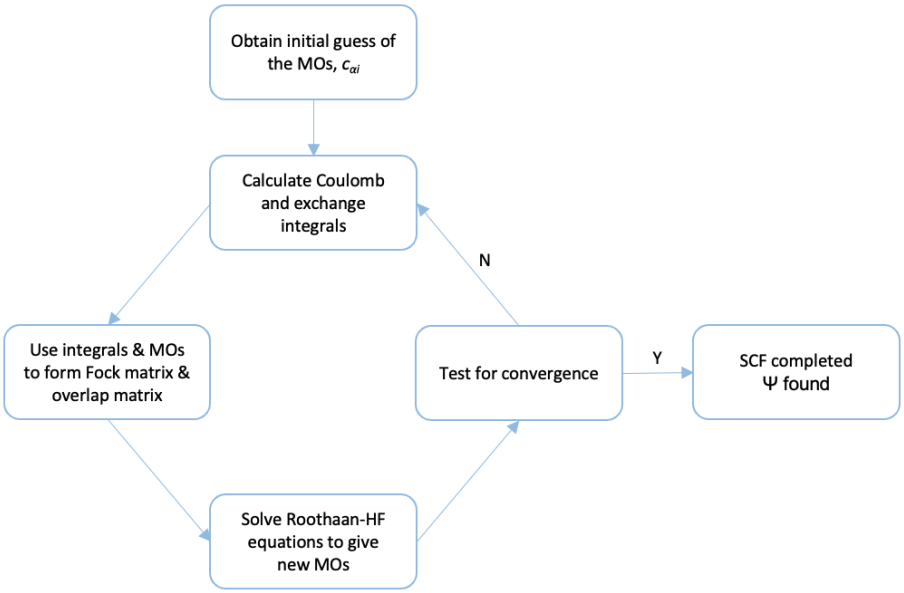

Figure 2.2: Self-consistent field (SCF) iterative flow diagram, using the Roothaan-Hall HF equations to determine the ground state wave function [51]

The test for convergence tests the output against a predetermined convergence limit, a measure of how close solutions need to be before the solution is determined to have converged. If the convergence criteria are not met, then the new MO's are substituted back into the Coulomb and exchange integral calculation step and the cycle continues until such a time as the

convergence criteria is met, or a defined cycle limit has been reached yielding no output. Provided the convergence criteria are met, the converged solution found ψ consists of a Slater determinant with ψ_i and $c_{\alpha i}$ coefficients that are used to calculate the orbital energies ϵ_i which are then used to calculate the final ground-state HF energy, E_{HF}.

The physical interpretation of the orbital energies ϵ is provided by Koopmans' theorem [57], stating that the orbital energy ϵ_i obtained from HF theory is an approximation of minus the ionisation energy associated with the removal of an electron from that particular orbital, $\epsilon_i \approx E_N - E^i_{N-1} = IE(i)$ [51].

The HF approach can be used on a restricted and unrestricted basis, depending on the electronic state of the system. For doubly occupied orbitals holding even pairs of electrons (closed-shell systems of a singlet state), the two spin orbitals share the same spatial orbital. This restriction leads to the "*restricted Hartree-Fock approximation*" (RHF). For systems with an odd number of electrons, i.e. a triplet state with unpaired electrons, there are two approaches to solve the HF equations. Firstly, stating explicitly that only certain orbitals are singly occupied, known as the "*restricted open-shell HF scheme*" (ROHF) and secondly, to remove any restriction and allow each spin orbital to have its own spatial orbital, known as the "*unrestricted Hartree-Fock variant*" (UHF) [51]. In UHF, the α and β orbitals experience different potentials and therefore have different spatial characteristics. A discussion regarding unrestricted and restricted methods is discussed later in the specific context of the C_{60} system.

As mentioned previously, in the HF method, the electron-electron repulsion is constructed by each electron experiencing an electrostatic potential averaged across all the other electrons in the system. However, in reality,

each electron moves due to instantaneous repulsion rather than the influence of an average repulsive electron cloud. The consequence of this is that HF theory predicts the electrons to be too close to each other with the calculated electron-electron repulsion being smaller than the true repulsion, which leads to an overestimation of the energy of the system. However, this is expected by the nature of the HF approach using an approximate wave function (the Slater determinant) to capture the majority of the physics of the many-electron system. The gap between the calculated HF energy and the true ground state energy E_0 is called the correlation energy, and it is a measure of the error introduced as a result of using the HF method [51].

$$E_C^{HF} = E_0 - E_{HF} \tag{2.30}$$

A major shortcoming of the HF method is that it does not properly account for electron correlation effects [51, 58], leading to inaccuracies when calculating molecular properties. Attempts to address the inaccuracies in correlation energy are tackled in different ways by post-HF methods, but are often too computationally expensive when studying larger systems. However, since the publication of the Hohenberg-Kohn (HK) theorems [59] in 1964, DFT has flourished as a computationally cost-effective electronic structure method to determine ground state properties for many-body chemical systems.

Basis sets

As discussed above, the use of basis sets provides a useful way to calculate the HF energy via the Roothaan-Hall HF equations. Basis sets are also used extensively in DFT, and so will be discussed first before introducing

the DFT methodology.

Basis sets are a set of mathematical functions known as basis functions that are used to represent atomic orbitals. The linear combination of these atomic orbitals (LCAO) produce molecular orbitals, describing the overall electron distribution of a molecule. There are several types of functions that are used to represent the electron distribution around an atom based on solutions to the Schrödinger equation for a hydrogen atom [60], plane waves, Slater functions and Gaussian functions. Slater and Gaussian functions are the simplest and widely used across quantum chemistry [61]. Slater functions, of the form $e^{-\alpha r}$ provide an accurate representation of the electron distribution's radial dependence, however, due to the two-electron integral components they are computationally expensive to use with *ab initio* methods. Therefore, linear combination of Gaussian functions, of the form $e^{-\alpha r^2}$, are used to approximate Slater functions. However, single Gaussian functions do not provide the accurate radial dependence at short and long distances and so several Gaussian functions, known as contracted basis functions or Slater-Type Orbitals (STO), are used in combination to better model the radial dependence [61], taking the form:

$$\chi(\mathbf{r}) = c_1 e^{-a_1 r^2} + c_2 e^{-a_2 r^2} + c_3 e^{-a_3 r^2} \tag{2.31}$$

For example, STO-1G and STO-3G, using one Gaussian and 3 Gaussian functions respectively, each with contracting coefficients used to control the width of the orbital [60], are shown in Eq. (2.32) with the Slater function presented for comparison:

$$
\begin{aligned}
\phi_{Slater} &= 0.7790e^{-1.24r} \\
\phi_{STO-1G} &= 0.3696e^{-0.4166r^2} \\
\phi_{STO-2G} &= 0.6789e^{-0.1516r^2} + 0.4301e^{-0.9518r^2} \\
\phi_{STO-3G} &= 0.0835e^{-0.1689r^2} + 0.2678e^{-0.6239r^2} + 0.2679e^{-3.4253r^2}
\end{aligned}
\tag{2.32}
$$

Figure 2.3, from Szabo and Ostlund's excellent book "Modern Quantum Chemistry" [62] compares Slater, STO-1G, STO-2G and STO-3G basis sets and demonstrates the improving radial dependence of Slater-Type Orbitals as more contracted basis functions are added as better approximations to the Slater function.

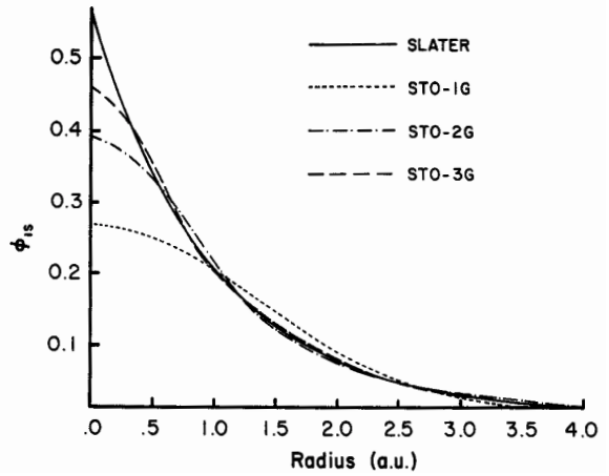

Figure 2.3: Comparison of the quality of the least-squares fit of a 1s Slater function $\zeta = 1.0$ obtained at the STO-1G, STO-2G and STO-3G levels [62].

As this approach has developed, numerous other basis sets have been developed to more accurately model the electron distribution of molecular systems. For example, Pople Basis Sets, developed by John Pople, are split valence sets, recognising that much chemistry can be understood through the interaction of valence orbitals [63]. For example, the 6-31G basis uses a linear combination of 6 contracted Gaussian functions for each inner shell,

with each valence shell STO split into an inner and outer part (double zeta) using 3 and 1 contracted Gaussian's respectively. These split-valence basis sets can be expanded to included polarisation functions to take into account the polarisability of electron distributions (denoted by an asterisk, e.g. 6-31G*) and diffuse functions to account for expanded electron clouds i.e. lone pair electrons that are loosely bound to the atomic nucleus (denoted by a "+" sign, e.g. 6-31+G*. Usually polarisation and diffuse functions do not include hydrogen or helium, however, if they are included this is indicated by a "**" or a "++" e.g. 6-31++G**.

In addition, Dunning basis sets [64] are another commonly used group of basis sets, designed for correlation consistency, e.g. cc-pVDZ and cc-pVTZ, where "cc-p" stands for correlation-consistent polarisation, "V" stands for valence only, "D" represents double zeta and "T" represents triple zeta. The main idea behind correlation consistency is that functions which contribute approximately the same amount of correlation energy are grouped together when considering the mixture of orbital basis functions to use. This enables these basis sets to converge smoothly towards the complete and infinite basis set limit.

2.1.2 Density Functional Theory

DFT, at its most simple, is a theoretical method of obtaining an approximate solution to the Schrödinger equation of a many-body system [51] and provides a computationally low-cost ground state electronic structure method in which the energy is determined by the electron density. A key feature of DFT, compared to HF and alternative post-HF methods, is the utilisation of electron density to compute molecular properties which can be measurable e.g. by X-ray diffraction.

The electron density is given by:

$$\rho(\mathbf{r}) = \sum_{i=1}^{N} |\Psi_i(\mathbf{r})|^2 \tag{2.33}$$

where $\rho(\mathbf{r})$ determines the probability of finding any of the system's electrons within a set of molecular orbitals ($\Psi_i(\mathbf{r})$) and the volume $d\mathbf{r}$ [65]. The integral of the electron density gives the number of electrons (N):

$$\int \rho(\mathbf{r}) d\mathbf{r} = N \tag{2.34}$$

The integral defines the electron density as a function of position only (three variables; x, y, z), as opposed to three position variables and one spin coordinate ($4N$ variables for the wave function of an N-electron system) used in other wave-function computational methods. This provides a significant scaling advantage when looking at ever-larger systems, where the electron density will always be a function of just three spatial variables [66].

The electron density is determined by the HK theorems [59]. Theorem 1 states that "*the ground state of any interacting many-particle system with a given fixed inter-particle interaction is a unique functional of the electron density*". A functional is a function whose argument is itself a function. A functional is described by the use of square brackets for the argument, $F[f]$, compared to a function of an arbitrary variable x being $f(x)$. Therefore, if we know the ground state electron density functional, we can theoretically determine all the ground state properties of a molecule and calculate the energy, given by:

$$E[\rho_0] = E_0 \tag{2.35}$$

However, the problem with this theorem is that despite proving rigorously that a functional of the electron density exists, the theorem is silent about the form of the functional, and so we must infer that an approximate or trial functional only gives an approximate solution [67].

Theorem 2 states that "*the ground state energy can be obtained variationally: the density that minimises the total energy is the exact ground state density*" [67]. Therefore, any approximate or trial electron density functional will give a solution to the energy greater than or equal to the true ground state energy.

$$E_v[\rho_t] \geq E_0[\rho_0] \tag{2.36}$$

where E_v is the electronic energy from a trial electron density ρ_t moving under the external potential $v(r)$ of the system's atomic nuclei. $E_0[\rho_0]$ corresponds to the true ground state energy and the true electron density.

Under the Born-Oppenheimer approximation, used to reduce the number of degrees of freedom of a many-body system, the total energy of the system (formulated as a functional of the electron density) is separated into three parts, the electron kinetic energy, the attractive nuclei-electron potential energies and the repulsive electron-electron potential energies.

$$E_0 = T[\rho_0] + V_{Ne}[\rho_0] + V_{ee}[\rho_0] \tag{2.37}$$

The nuclear-electron attraction potential can be written as:

$$V_{Ne} = \int \rho_0(\mathbf{r}) v(\mathbf{r}) d\mathbf{r} \tag{2.38}$$

and so:

$$E_0 = \int \rho_0(\mathbf{r}) v(\mathbf{r}) dr + T[\rho_0] + V_{ee}[\rho_0] \tag{2.39}$$

Difficulties arise when attempting to derive the exact functionals of these terms, which lead to insufficient accuracy for applications [68]. To overcome this, Kohn and Sham [69] presented a reformulation to deal with two problems, firstly that $T[\rho_o]$ and $V_{ee}[\rho_0]$ are unknown and secondly that treatment of the kinetic energy functional was difficult without using orbitals [70]. To deal with the first problem, Kohn and Sham introduced the idea of collecting the unknown terms, $T[\rho_o]$ and $V_{ee}[\rho_0]$, into one term and then computing the remaining terms. This was achieved by defining $\Delta T[\rho_0]$ as the deviation of the real kinetic energy $T[\rho_0]$ from a reference kinetic energy $T_r[\rho_0]$, being a reference system of non-interacting electrons.

$$\Delta T[\rho_0] = T[\rho_0] - T_r[\rho_0] \tag{2.40}$$

and defining $\Delta V_{ee}[\rho_0]$ as the deviation of the true electron-electron repulsion energy from the Coulomb repulsion energy, $J[\rho_0]$:

$$\Delta V_{ee}[\rho_0] = V[\rho_0] - J[\rho_0] \tag{2.41}$$

where

$$J[\rho_0] = \frac{1}{2} \int \int \frac{\rho_0(\mathbf{r}_1)\rho_0(\mathbf{r}_2)}{r_{12}} d\mathbf{r}_1 d\mathbf{r}_2 \tag{2.42}$$

The sum of Eq. (2.40), the deviation of kinetic energy and Eq. (2.41), the deviation from the Coulomb repulsion, is called the exchange correlation

energy functional, constituting the grouped unknown terms [71].

$$E_{XC}[\rho_0(\mathbf{r})] = \Delta T[\rho_0] + \Delta V_{ee}[\rho_0] \tag{2.43}$$

Substituting Eq. (2.40), Eq. (2.41), Eq. (2.42) and Eq. (2.43) into Eq. (2.39) yields the energy of the system.

$$E_0 = \int \rho_0(\mathbf{r}) v(\mathbf{r}) dr + T_r[\rho_0] + \frac{1}{2} \int \int \frac{\rho_0(\mathbf{r}_1)\rho_0(\mathbf{r}_2)}{r_{12}} d\mathbf{r}_1 d\mathbf{r}_2 + E_{XC}[\rho_0] \tag{2.44}$$

These equations are used to derive the energy of the system, Kohn-Sham (KS) orbitals and energy levels using the Hohenberg-Kohn theorems. The electron density of the reference system is the same as the electron density of the real system, given by:

$$\rho_0 = \rho_r = \sum_{i=1}^{2n} |\Psi_i^{KS}(1)|^2 \tag{2.45}$$

where Ψ_i^{KS} are the KS orbitals, n is the number of occupied KS spatial orbitals and $2n$ is the number of electrons in the system. The introduction of KS orbitals was a major insight [70], enabling the KS energy to be calculated computationally. Substituting into Eq. (2.44) and varying E_0 with respect to the KS spatial orbitals leads to the KS equations:

$$\left[-\frac{1}{2} \bigtriangledown_i^2 - \sum_A \frac{Z_A}{\mathbf{r}_{1A}} + \int \frac{\rho(\mathbf{r}_2)}{\mathbf{r}_{12}} d\mathbf{r}^2 + \nu_{XC}(1) \right] \Psi_i^{KS}(1) = \epsilon_i^{KS} \psi_i^{KS}(1) \tag{2.46}$$

The KS equations are one-electron equations, where ϵ_i^{KS} are the Kohn Sham energy levels and $\nu_{XC}(1)$ is the exchange correlation potential (for electron number 1), defined by:

$$\nu_{XC}(\mathbf{r}) = \frac{\delta E_{XC}[\rho(\mathbf{r})]}{\delta \rho(\mathbf{r})} \tag{2.47}$$

In a more concise format, Eq (2.46) can be written as:

$$\hat{h}^{KS}(1)\Psi_i^{KS}(1) = \epsilon_i^{KS}\psi_i^{KS}(1) \tag{2.48}$$

where $\hat{h}^{KS}(1)$ is the KS operator (defined in Eq. (2.46)). These KS eigenvalue equations are expanded in terms of basis functions known as basis sets.

$$\Psi_i^{KS} = \sum_{s=1}^{Nb} c_{si}\chi_s \qquad i = 1, 2, 3, ..., N_b \tag{2.49}$$

χ_s are the basis functions and c_{si} are the coefficients of the basis functions. When this basis set expansion is substituted into the KS equations (Eq. (2.46) and Eq. (2.48)) a matrix, with size dependent on the number of basis sets, N_b, is generated. In order to solve the KS equations computationally in DFT, an approximation of the density function $\rho(r)$ is calculated by summing a "guess" of the electron densities of the individual atoms. The KS operator $\hat{h}^{KS}$ is then calculated from this approximation, from which the KS Fock matrix elements are calculated. The matrix is diagonalised and orthogonalised to give the initial guesses of the coefficients c in Eq. (2.49) and values of ϵ. These coefficients are then used in Eq. (2.46) to calculate a better density function, where the new density function is used to calculate improved matrix elements. This process continues iteratively until the electron density converges, from which the final KS orbitals are used to calculate the energy from Eq. (2.44).

Over the last six decades, much research and resource has focused on designing more accurate approximations to the exchange-correlation functionals that describe electron density and the basis sets used to describe the electronic wave functions [71, 72]. The success and accuracy of functionals often depend on the molecular system and chemical properties under in-

vestigation; a functional that works well to predict kinetics may not be successful when predicting energetics or thermochemistry. Therefore, a careful selection of computational parameters (functionals, basis sets, dispersion correction etc.) is an important consideration in providing reasonable assurance that the DFT calculations are sufficiently accurate to predict the chemical properties of molecular systems. In an ideal world, once the DFT level of theory has been validated, testing the predicted properties against experimental evidence provides greater assurance that the functional and basis set combination chosen is sufficiently accurate to predict the structural, ground-state energetics and electronic properties of the molecular system in question.

Exchange correlation functionals

As stated previously, the electron density function $E_{XC}[\rho(\mathbf{r})]$ is the sum of the unknown deviations in kinetic energy and Coulomb repulsion (Eq. (2.43)) [71], and so a better approximation of this term leads to a better approximation of the KS electron density and energy. In order to achieve this, the exchange-correlation potential $\nu_{XC}(\mathbf{r})$ requires calculation, being the functional derivative of the exchange-correlation functional acting on the electron density function $E_{XC}[\rho(\mathbf{r})]$. Several approximations of $E_{XC}[\rho(\mathbf{r})]$ exist, grouped by a Jacob's ladder of approximations [73, 74]. Each rung of the ladder represents a different level of approximation that improves on the last rung by adding capabilities.

The first rung of Jacob's ladder of approximations is the simplest model being the local density approximation (LDA) proposed by Kohn and Sham [75] and assumes that the density can be treated as a uniform electron gas only depending on the density at position $\mathbf{r}$:

$$E_{XC}^{LDA}[\rho] = \int \rho(\mathbf{r})\epsilon_{XC}[\rho(\mathbf{r})]d\mathbf{r} \tag{2.50}$$

where $\epsilon_{XC}[\rho(\mathbf{r})$ is the exchange-correlation energy per particle of a uniform electron gas of density $\rho(\mathbf{r})$ [71] which can be further defined as the summation of the exchange and correlation contributions:

$$\rho(\mathbf{r})\epsilon_{XC}[\rho(\mathbf{r})] = \epsilon_X[\rho(\mathbf{r})] + \epsilon_C[\rho(\mathbf{r})] \tag{2.51}$$

where $\epsilon_X[\rho(\mathbf{r})]$ is the exchange contribution and $\epsilon_C[\rho(\mathbf{r})]$ is the correlation contribution.

Note that the LDA can be improved upon by assigning different KS orbitals, ψ_α^{KS} and ψ_β^{KS}, for electrons of different spin, α and β, known as the local spin density approximation (LSDA) [39, 71].

Given that the electron density within atoms or molecules usually varies greatly across the molecular system, the LDA and LSDA are generally poor approximations to the form of the actual electron density. The majority of exchange correlation functionals used in DFT tend to use the electron density at a specific position and also the gradient at $\mathbf{r}$, $\nabla\rho$, known as generalised-gradient approximation functionals (GGA) [71], the next rung of Jacob's ladder, summarised as:

$$E_{XC}^{GGA}[\rho] = \int \rho(\mathbf{r})\epsilon_{XC}[\rho(\mathbf{r}), \nabla\rho]d\mathbf{r} \tag{2.52}$$

Popular GGA functionals include BLYP [39, 76] and PBE [77].

On the next rung, Meta-GGA (mGGA) functionals improve upon GGA by

introducing a dependency on the second derivative of the density, $\nabla^2\rho$, the KS kinetic energy density:

$$E_{XC}^{mGGA}[\rho] = \int \rho(\mathbf{r})\epsilon_{XC}[\rho(\mathbf{r}), \nabla\rho, \nabla^2\rho(\mathbf{r})]d\mathbf{r} \tag{2.53}$$

A common example of a meta-GGA is TPSS [78].

Next comes hybrid-GGA functions that mix an exact HF exchange contribution (calculated from HF theory) with a GGA contribution. One of the most common hybrid-GGA functionals is B3LYP [38], a hybrid functional that separates the exchange correlation functional into the "*Becke*" exchange functional and "*Lee Yang Parr*" correlation functional, with additional corrective components to improve the accuracy of the approximation:

$$E_{XC}[\rho] = a_0 E_{HF}^X + (1 - a_0 - a_x)E_{LDA}^X + a_x E_B^X + (1 - a_c)E_{VWN}^C + a_c E_{LYP}^C \tag{2.54}$$

where E_{HF}^X is the HF component of the exact exchange, E_{LDA}^X is the LDA exchange component and E_B^X is the Becke GGA exchange. E_{VWN}^C is the Vosko, Wilk, Nusair correlation function [79] and E_{LYP}^C is the LYP functional mentioned previously. The coefficients a weight each component and in B3LYP $a_0 = 0.20$, $a_x = 0.72$ and $a_c = 0.81$ [38]. Other common hybrid-GGA's are the PBE0 functional [80] and ωB97X-V, a 10 parameter and range-separated hybrid GGA [81] that incorporates a long-range correction, and B3P86 which is B3LYP with LYP being replaced by a non-local correlation contribution provided by Perdew in 1986 [82].

Dispersion correction

A major issue with conventional functionals is that they could not describe long range van-der Waals dispersion interactions, which are important for larger molecular systems. This was solved by an empirical correction known as "*dispersion correction*" to the overall energy of the system:

$$E_{DFT-D} = E_{DFT} + E_{disp} \tag{2.55}$$

One of the first empirical dispersion corrections introduced into DFT was in 2002 [83], tested against four functionals, B3LYP, BLYP, BPW91 and PW91, being:

$$E_{disp} = -\sum_{J>I} f_{damp}(R_{IJ}) \frac{C_6^{IJ}}{R_{IJ}^6} \tag{2.56}$$

where f_{damp} is the damping function where $f_{damp} = 0$ for small values of R_{IJ} and $f_{damp} = 1$ for large values of R_{IJ}. C_6^{IJ} are coefficients obtained by fitting to accurate reference molecular C_6 dispersion coefficients.

In 2010, Grimme et al. [84, 85] expanded on this approach and previous work undertaken and added a similar empirical correction to many well-used functionals, known as DFT-D3 (preceded by DFT-D1 and DFT-D2 approaches), including a scaling parameter that accounted for the differences in how each functional included van der Waals interactions:

$$E_{disp} = -\frac{1}{2} \sum_{i=1}^{N_{at}} \sum_{j=1}^{N_{at}} \sum_{\mathbf{L}} \left(f_{d,6}(r_{ij,L}) \frac{C_{6ij}}{r_{ij,L}^6} + f_{d,8}(r_{ij,L}) \frac{C_{8ij}}{r_{ij,L}^8} \right) \tag{2.57}$$

where $R_{0ij} = \sqrt{\frac{C_{8ij}}{C_{6ij}}}$, L is the Gaussian-distance weighted average, and

$f_{d,n}(r_{ij})$ is the damping function:

$$f_{d,n}(r_{ij}) = \frac{s_n}{1 + 6(r_{ij}/(s_{R,n}R_{0ij}))^{-\alpha_n}} \tag{2.58}$$

The parameters α_6, α_8, $s_{R,8}$ and s_6 are fixed values of 14, 16, 1, and 1 respectively whilst s_8 and $s_{R,6}$ are adjustable depending on the choice of functional. Within DFT, the damping can be varied by implementing the Becke-Johnson damping function [86]:

$$f_{d,n}(r_{ij}) = \frac{s_n r_{ij}^n}{r_{ij}^n + (a_1 R_{0ij} + a_2)^{-n}} \tag{2.59}$$

where $s_6 = 1$ and a_1, a_2 and s_8 are adjustable parameters specific to the functional employed. The DFT-D3(BJ) approach is used in this research, with parameters adjusted to the specific functional selection.

Alternative computational methods

KS-DFT is not the only electronic structure method used to predict chemical properties. DFT, in its present form, cannot be applied to systems with strong multi-reference character [87]. Before DFT became a popular choice, organometallic systems and inorganic systems containing metal atoms were usually investigated using Møller-Plesset second-order perturbation theory (MP2) [88]. However, for strongly correlated systems, the use of orbitals where the unrestricted Hartree-Fock (UHF) reference exhibits spin-contamination (artificial-symmetry breaking) lead to disastrous performance of MP2 [89]. Consequently, alternatives were developed such as orbital-optimised MP2 (OOMP2) [90] and orbital-optimised MP3 (κ-OOMP2) [91] to reduce the level of spin-contamination and thus improving

the reliability of the calculations. Therefore, an assessment of the electron correlation of a chemical system is important to understand before choosing the most appropriate single reference or multi-reference computational method.

With regard to fullerene systems, particularly C_{60}, a computational study [92] reported that electron density is highly correlated and therefore warned against using single reference methods such as DFT to model properties. However, this is juxtaposed by recent research [91] showing that the electron density in C_{60} is minimally correlated and therefore deemed single-reference methods as appropriate. The aforementioned paper suggested that a singlet-triplet gap of less than 10 kcal mol^{-1} is a useful predictor of bi-radicaloid nature (electrons singly occupying molecular orbitals) and therefore a minimal degree of electron correlation. This research follows the latter line of reasoning suggesting that whilst there might be evidence of correlation in smaller fullerenes, C_{60} is a weakly correlated system, aligning with experimental evidence of paramagnetic silence [93].

Computational calculations in this thesis use the single reference computational approach, DFT, implemented in the Q-Chem quantum chemistry software package [94], to calculate geometry optimised structures, single point energies and partial charge values, at the B3P86-D3 / cc-pVDZ level of theory, using DDEC6 to calculate partial charge values. No symmetry was imposed in the calculations, and all minima were confirmed through frequency analysis.

2.2 Classical electrostatics

Between 1861 and 1865, James Clerk Maxwell successfully unified the previously independent theories of electricity and magnetism into four elegant partial differential equations that relate the electric and magnetic fields in free-space to each other and also to electric charges and currents [95].

$$\nabla.\mathbf{E} = 4\pi\rho \tag{2.60}$$

$$\nabla \times \mathbf{B} - \frac{1}{c}\frac{\partial \mathbf{E}}{\partial t} = \frac{4\pi}{c}\mathbf{J} \tag{2.61}$$

$$\nabla.\mathbf{B} = 0 \tag{2.62}$$

$$\nabla \times \mathbf{E} + \frac{\partial \mathbf{B}}{\partial t} = 0 \tag{2.63}$$

where $\mathbf{E}$ is the electric field, $\mathbf{B}$ is the magnetic field, ρ is the electric charge density and $\mathbf{J}$ is the electric current density. Note that the above formulation of Maxwell's equations are in Gaussian units, which are often more convenient for practical purposes as this system needs only one fundamental constant (the speed of light), rather than two (the permittivity and the permeability of free space) when using SI units. A particularly remarkable feature of Maxwell's achievement was realised following Einstein's publication of the theory of Special Relativity, that the equations were found to be entirely compatible with special relativity [96]. When electrostatics are considered, i.e. where there is a time-independent electric field and no magnetic field, the Maxwell equations reduce to:

$$\nabla.\mathbf{E} = 4\pi\rho \qquad \nabla \times \mathbf{E} = 0 \tag{2.64}$$

This research focuses on modelling $Ca@C_{60}$ as a dielectric sphere, an azimuthally-

symmetrical system. Before this specific system is considered, the appropriate theoretical foundations, relevant to such a system, need to be understood. These foundations are summarised below using Christopher Pope's incredibly useful teaching resource from Texas AM University [96] and David Griffith's excellent book on Electrodynamics [97].

Every electromagnetic problem can be viewed as a problem formulated in free space with many electric point charges. However, the number of individual microscopic point charges that make up the problem are often so great that practical calculations are impossible and so it becomes preferable to use a "macroscopic approximation" which takes a macroscopic view of the problem in hand. In order to give a macroscopic formulation of the electrostatic equations in the presence of media (e.g. a dielectric), $\mathbf{E}$ is interpreted as an average value of the electric field with the introduction of a new quantity, $\mathbf{D}$, the electric displacement where $\mathbf{D} = \mathbf{E}$ in free space but in a medium represents a "back-reacted" version of $\mathbf{E}$ that takes into account the fact that, on macroscopic level, the positive, and negative charges in the medium are displaced as a result of the externally-applied $\mathbf{E}$ field which causes distortion in the system, resulting in a polarisation or effective electric dipole.

$$\mathbf{D} = \mathbf{E} + 4\pi\mathbf{P} \tag{2.65}$$

Consequently, the relevant electrostatic Maxwell equations are modified in a medium to become:

$$\nabla.\mathbf{D} = 4\pi\rho \qquad \nabla \times \mathbf{E} = 0 \tag{2.66}$$

Many problems in electrostatics involve boundary conditions, e.g. the interface between free-space and a particular medium, which can be determined by performing appropriate integrals of the two equations in Eq. (2.66). Firstly, and with regard to the left-hand equation involving $\mathbf{D}$, the electric displacement, $\nabla.\mathbf{D} = 4\pi\rho$ is integrated over a "*Gaussian-pillbox*" that straddles the interface. The caps of the cylindrical pillbox are considered to be parallel to the interface, with the interface bisecting the cylinder with one cap on each side. The divergence theorem can be used to solve the problem, stating that "*the surface integral of a vector field over a closed surface is equal to the volume integral of the divergence over the region inside the surface*" [97]:

$$\int_V \nabla.\boldsymbol{v} d\mathbf{V} = \int_S \boldsymbol{v}.d\mathbf{S} \tag{2.67}$$

where $\boldsymbol{v}$ is any vector field and $\mathbf{S}$ is a closed surface enclosing volume $\mathbf{V}$. Integrating $\nabla.\mathbf{D} = 4\pi\rho$ over the pillbox and applying the divergence theorem, the boundary condition can be found:

$$\mathbf{n}.(\mathbf{D_1} - \mathbf{D_2}) = 4\pi\sigma \tag{2.68}$$

where n is the unit normal vector pointing from medium 1 to medium 2

and σ is the surface charge density (charge per unit area). This boundary condition says that there is a discontinuity in the normal component of $\mathbf{D}$, given by 4π multiplied the surface charge density.

For the electric field $\mathbf{E}$ (the right-hand equation in Eq. (2.66)), one considers a rectangular loop formed by two infinitesimally-separated parallel line elements that straddles the interface. This can be solved using Stoke's theorem that states that "*the surface integral of the curl of a function over a surface bounded by a closed surface is equal to the line integral of the particular vector function around that surface*" [97]

$$\int_{\Sigma} (\nabla \times \boldsymbol{\upsilon}).d\mathbf{S} = \oint_{C} \boldsymbol{\upsilon}.d\mathbf{l} \tag{2.69}$$

where υ is again any vector field and Σ denotes an open surface whose boundary is the closed loop C. Integrating $\nabla \times \mathbf{E} = 0$ over the area Σ and applying to Stoke's theorem, the second boundary condition can be found:

$$\mathbf{n} \times (\mathbf{E_1} - \mathbf{E_2}) = 0 \tag{2.70}$$

where n is again the unit normal vector pointing from medium 1 to medium 2. This boundary condition says that the tangential components of the electric field $\mathbf{E}$ must be continuous across the interface. Now the boundary conditions have been defined, one can construct the complete electrostatic problem. In electrostatics, the electric field can be written in terms of a scalar potential ϕ:

$$\mathbf{E} = -\nabla\phi \tag{2.71}$$

Substituting this into the free space Maxwell equations for electrostatics (the first equation in Eq. (2.66)) leads to the Poisson equation:

$$\nabla^2\phi = -4\pi\rho \tag{2.72}$$

where ∇^2 is the Laplacian, a scalar differential operator.

Solving any problem in electrostatics can be reduced to solving the Poisson equation for a given charge density ρ in a volume V bounded by a surface S and subject to given boundary conditions. This is known as the boundary-value problem [96]. A useful feature of the Laplacian ∇^2 is that it becomes separable when the problem is defined in Cartesian, spherical polar or cylindrical coordinates, enabling Laplace's equation to be factored into a second-order ordinary differential equation, which is of great benefit when trying to construct solutions [97]. In order to solve this particular case, one must perform a separation of variables in spherical polar coordinates. The separation of variables approach is well known and will not be repeated here, other than to state the separated radial equation for the case of an azimuthally-symmetric system that can be used to model $Ca@C_{60}$.

A problem that is azimuthally symmetric in spherical polar coordinates means that it is independent of the azimuthal coordinate, φ. The potential ϕ can therefore be separated:

$$\phi(r,\beta) = \frac{1}{r}R(r)\Theta(\beta) \tag{2.73}$$

where R and Θ satisfies Laplace's equation whose variables have been separated in spherical polar coordinates, being the radial equation:

$$\frac{d^2R}{dr^2} = \frac{\lambda}{r^2}R, \qquad \frac{1}{\Theta}sin\beta\frac{\mathrm{d}}{\mathrm{d}\theta}(sin\beta\frac{\mathrm{d}\Theta}{\mathrm{d}\beta}) + \lambda\Theta = 0 \tag{2.74}$$

The radial equation is a Legendre equation, with solutions being Legendre polynomials when $\lambda = l(l+1)$. The first four Legendre polynomials, defined in Eq. (2.75) in traditional terms of x:

$$\begin{aligned} P_0(x) = 1, \qquad P_1(x) = x, \qquad P_2(x) = \frac{1}{2}(3x^2-1), \\ P_3(x) = \frac{1}{2}(5x^3-3x), \qquad P_4(x) = \frac{1}{8}(35x^4-30x^2+3) \end{aligned} \tag{2.75}$$

Since the goal is to find solutions of Laplace's equation in spherical polar coordinates and that azimuthally-symmetric solutions are defined in terms of Legendre polynomials, a general azimuthally-symmetric solution requires the expansion of Legendre polynomials in terms of $x = cos\beta$ (where β is the zenith angle) which takes the general form:

$$f(x) = \sum_{l\geq 0} a^l P_l(x) \tag{2.76}$$

where a_l is derived as:

$$a_l = \frac{1}{2}(2l+1)\int_{-1}^{1} dx f(x) P_l(x) \tag{2.77}$$

A key property of this expansion is the orthogonality condition:

$$\int_{-1}^{1} dx P_l(x) P_{l'}(x) = \frac{2}{2l+1}\delta_{l,l'}, \qquad l \neq l' \tag{2.78}$$

where $\delta_{l,l'}$ is known as Kronecker delta which equals 1 if l and l' are equal, and zero otherwise.

The two linearly independent solutions of the radial equation are $R = r^{l+1}$ and $R = r^{-l}$, therefore, by summing over all possible factorised solutions of the form of Eq. (2.74) the general azimuthally symmetric solution is defined [96]:

$$\phi(r,\beta) = \sum_{l\geq 0}(A_l r^l + B_l r^{-l-1}) P_l(cos\beta) \tag{2.79}$$

where A_l and B_l are arbitrary constants determined by the boundary conditions of the system.

2.2.1 Modelling Ca@C_{60}

For the case of modelling the electrostatics of Ca@C_{60}, this research extends the work performed by Raggi et al. [44] and Deng and Cai [98], modelling Ca@C_{60} as a point charge within a dielectric sphere, immersed in an infinite dielectric medium:

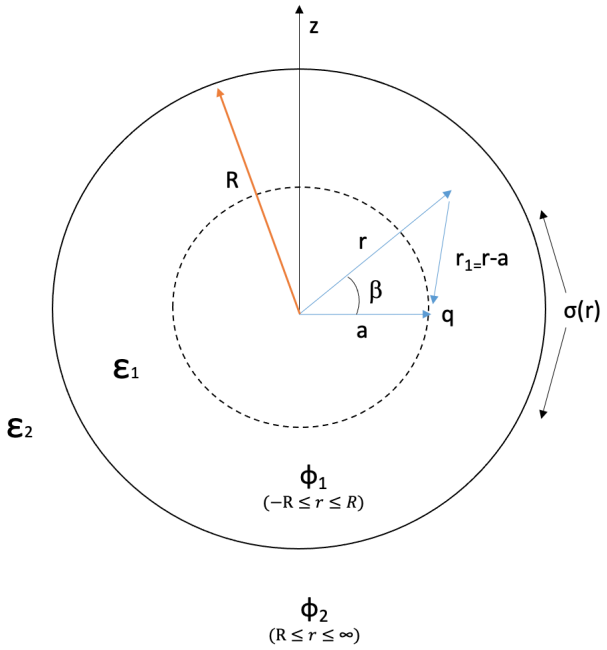

Figure 2.4: Geometric representation of a point charge within a dielectric sphere where $\sigma(r)$ is the surface charge density, $\phi(r)$ is the electric potential, q is the encapsulated point charge, R is the radius of the dielectric sphere, a is the length from the centre, r is the observation position and ϵ_1 and ϵ_2 are the internal and external dielectric constants respectively.

The boundary conditions defined in Eq. (2.70) and Eq. (2.68), in relation to this dielectric system, state that the normal components of the dielectric displacement field $\mathbf{D}$ and the tangential components of the electric field $\mathbf{E}$ satisfy the following equations [44] either side of the dielectric boundary:

$$\begin{aligned} \mathbf{n} \times (\mathbf{D}_{\mathbf{r}=\mathbf{R}^+} - \mathbf{D}_{\mathbf{r}=\mathbf{R}^-}) = 0 \\ \mathbf{n} \times (\mathbf{E}_{\mathbf{r}=\mathbf{R}^+} - \mathbf{E}_{\mathbf{r}=\mathbf{R}^-}) = 0 \end{aligned} \tag{2.80}$$

where R^+ and R^- are the radial positions just outside and inside the dielectric sphere respectively and $\mathbf{n}$ is the previously mentioned unit vector normal to the surface that is directed outwards from the sphere surface. The total surface charge is defined as the sum of a uniformly distributed free charge Q and a bound polarisation charge σ. At the boundary, the normal component of the electric field is discontinuous due to the presence of a permanent surface charge [99] and therefore this defines one of the key boundary conditions:

$$\sigma(R,\beta) = \varepsilon_1 \left[\frac{\partial \phi_1}{\partial r}\right]_{r=R} - \varepsilon_2 \left[\frac{\partial \phi_2}{\partial r}\right]_{r=R} \tag{2.81}$$

There are four other boundary conditions that exist for this system [44, 99], defining the limits of the analytical expressions for $0 \leq r \leq R$ and $R \leq r \leq \infty$:

1. The electric potential vanishes at infinity $\phi_2(r,\beta) \to 0$ as $R \to \infty$.

2. The internal potentials are finite inside the sphere.

3. The potentials and the fluxes normal to the spherical boundary are continuous at the boundary;

$$\phi_1(R,\beta) = \phi_2(R,\beta), \qquad \varepsilon_1 \left[\frac{\partial \phi_1}{\partial r}\right]_{r=R} = \varepsilon_2 \left[\frac{\partial \phi_2}{\partial r}\right]_{r=R} \tag{2.82}$$

4. The continuity of the potential on the surface of the sphere is due to the continuity of the tangential component of the electric field, which

is automatically satisfied by the choice of electric potential $\phi(r, \beta)$.

$$\left[-\frac{1}{r}\frac{\partial \phi_1}{\partial \beta}\right]_{r=R^-} = \left[-\frac{1}{r}\frac{\partial \phi_2}{\partial \beta}\right]_{r=R^+} \tag{2.83}$$

The point charge's potential also needs to be accounted for within the electrostatic problem. Usefully, the potential due to a point charge can be expanded as a summation of Legendre polynomials, where the potential felt at r by the unit charge at a is:

$$\begin{aligned} \frac{q}{4\pi\varepsilon_1 |r-a|} &= \frac{q}{4\pi\varepsilon_1 a}\sum_{l=0}^{\infty}\left(\frac{r}{a}\right)^l P_l(cos\beta), \qquad 0 \leq r \leq a \\ \frac{q}{4\pi\varepsilon_1 |r-a|} &= \frac{q}{4\pi\varepsilon_1 a}\sum_{l=0}^{\infty}\left(\frac{a}{r}\right)^l P_l(cos\beta), \qquad a \leq r \leq R \end{aligned} \tag{2.84}$$

Given both the potentials of the point charge and the dielectric sphere are both azimuthally-symmetric and can therefore be defined in terms of Legendre polynomials, the application of the boundary conditions to this problem enables an analytical expression to be derived for the potentials and surface charge density of the system, all in terms of Legendre polynomials. This solution shall be developed and discussed further in the next chapter.

Computational electrostatic calculations were implemented in the Mathematica software package [100], to calculate the numerical values of the analytical solutions. The summations used 200 terms to ensure convergence, with the resulting solutions being visualised using the inbuilt graphical analysis tools in Mathematica.

Chapter 3

Electrostatic analysis of the surface charge polarisation for metallofullerenes

3.1 Modelling surface charge polarisation of dielectric particles

The electrostatic properties of materials are important to understand when considering applications to industrial processes and procedures, especially in areas where electrostatic effects dominate particle behaviour, for example the removal of fine particles and coal dust in power stations, particle charging and deposition during powder coating, and the behaviour of particles in dry powder inhalers [44]. Work over the last decade by Bichoutskaia, Stace and Raggi et al. [44, 99] has contributed significantly to the understanding of the behaviour of dielectric particles, particularly how like-charged particles of dielectric materials can be attracted to one an-

other [101], through the mutual polarisation of charge leading to regions of attractive negative and positive surface charge density when dielectric particles are in close separation, and the polarisation response of a dielectric sphere due to an external point charge. These analytical solutions were developed using Legendre polynomial series expansions of the respective system's position-dependent electrostatic potential and relevant boundary conditions. These publications also demonstrate the importance of testing the validity of any theoretical approach through comparison with relevant quantum mechanical calculations and experimental evidence, if available.

The first hypothesis of this research is that the motion of an encapsulated metal confined within a fullerene cage is strongly correlated to the distribution of charge density on the cage surface. This was previously demonstrated by Raggi et al. [44] who presented an analytical solution for the distribution of surface charge on a dielectric sphere due to the presence of an external point charge, q. The solution described how the charge on the sphere's surface is polarised in the electric field into regions of positive and negative charge that varies with the separation, $(h-a)$, between the sphere and the point charge (and where k is the dimensionless dielectric constant, the permittivity relative to the vacuum $k = \frac{\varepsilon}{\varepsilon_0}$), represented geometrically in Figure 3.1.

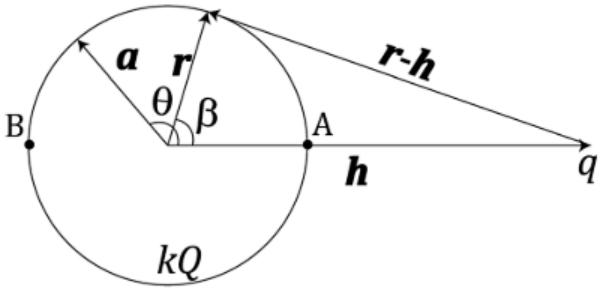

Figure 3.1: Geometric representation of the sphere–point charge interaction [44].

Raggi et al. derived the distribution of charge on the spherical bound-

ary induced by the presence of an external point charge by solving the Poisson equation to derive the system's electrostatic potentials (inside and outside the sphere) in the form of Legendre polynomial series expansions, as discussed in Chapter 2. The constants within the Legendre polynomial expansions were found by applying the system's relevant boundary conditions, leading to an expression for the polarisation surface charge density:

$$\sigma_{surf}^{pol}(cos\beta) = \frac{q}{4\pi h^2}\sum_{l=1}^{\infty}(2l+1)l\frac{(1-k)}{(1+k)l+1)}\left(\frac{a}{h}\right)^{l-1}P_l(cos\beta) \qquad (3.1)$$

This solution demonstrated that polarisation is particularly relevant at short separations with a large influence on the surface charge distribution of the dielectric sphere, confirmed through qualitative agreement with density functional theory calculations for C_{60} and C_{240} in the presence of an external point charge. This work gave weight to the ongoing debate that these fullerene molecules can be treated as dielectrics as opposed to metals. Whilst this is a useful starting point, in order to understand metallofullerenes e.g. Ca@C_{60}, an analytical solution is required for the case where the point charge is encapsulated within the dielectric sphere which is presented in this chapter. The aforementioned research by Raggi et al. [44], Deng and Cai [98] and relevant electrostatic potential solutions located in Batygin and Toptygin's 1978 book "*Problems in Electrostatics*" [102] have been very useful in informing the derivation of this solution.

3.2 A point charge within a dielectric sphere

The geometric representation of this model was described in Chapter 2 and repeated here for ease of reference.

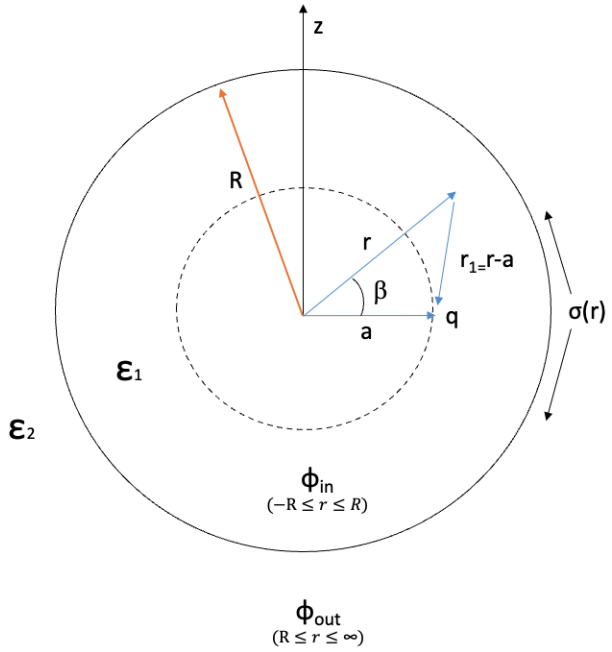

Figure 3.2: Geometric representation of a point charge within a dielectric sphere where $\sigma(r)$ is the surface charge density, $\phi(r)$ is the electric potential, q is the encapsulated point charge, R is the radius of the dielectric sphere, a is the length from the centre, r is the observation position and ϵ_1 and ϵ_2 are the internal and external dielectric constants respectively.

Following the logic of Deng and Cai [98] and Raggi et al. [44], the general solutions to the total potential field can be described as a summation of the contributions of the point charge and dielectric sphere potentials:

$$\begin{aligned} \phi_{in}(r,\beta) &= \phi_q(r,\beta) + \phi_{sphere}(r,\beta) \\ \phi_{in}(r,\beta) &= \frac{q}{4\pi\varepsilon_1 |r-a|} + \sum_{l=0}^{\infty} A_l r^l P_l(cos\beta), \qquad 0 \le r \le R \\ \phi_{out}(r,\beta) &= \frac{q}{4\pi\varepsilon_1 |r-a|} + \sum_{l=0}^{\infty} \frac{B_l}{r^{l+1}} P_l(cos\beta), \qquad R \le r \le \infty \end{aligned} \tag{3.2}$$

Expanding the Coulomb potential, $\phi_q(r,\beta)$, within the sphere in terms of

Legendre polynomials leads to the following expressions:

$$\begin{aligned} \frac{q}{4\pi\varepsilon_1 |r-a|} &= \frac{q}{4\pi\varepsilon_1 a}\sum_{l=0}^{\infty}\left(\frac{r}{a}\right)^l P_l(cos\beta), \qquad 0 \le r \le a \\ \frac{q}{4\pi\varepsilon_1 |r-a|} &= \frac{q}{4\pi\varepsilon_1 a}\sum_{l=0}^{\infty}\left(\frac{a}{r}\right)^l P_l(cos\beta), \qquad a \le r \le R \end{aligned} \tag{3.3}$$

Therefore, the complete electrostatic potentials in terms of Legendre polynomials can be described as:

$$\phi(r,\beta) = \begin{cases} \frac{q}{4\pi\varepsilon_1 a}\sum_{l=0}^{\infty}\left(\frac{r}{a}\right)^l P_l(cos\beta) + \sum_{l=0}^{\infty} A_l r^l P_l(cos\beta) & 0 \le r \le a \\ \frac{q}{4\pi\varepsilon_1 r}\sum_{l=0}^{\infty}\left(\frac{a}{r}\right)^l P_l(cos\beta) + \sum_{l=0}^{\infty} A_l r^l P_l(cos\beta) & a \le r \le R \\ \frac{q}{4\pi\varepsilon_1 r}\sum_{l=0}^{\infty}\left(\frac{a}{r}\right)^l P_l(cos\beta) + \sum_{l=0}^{\infty} \frac{B_l}{r^{l+1}} P_l(cos\beta) & R \le r \le \infty \end{cases} \tag{3.4}$$

Using the boundary condition that the potentials and the fluxes normal to the spherical boundary are continuous at the boundary (see Chapter 2 for the full set of boundary conditions) and the orthogonality property of Legendre Polynomials, an expression for A_l and an equation satisfying the boundary condition can be derived:

$$\phi_1(R,\beta) = \phi_2(R,\beta)$$

$$\sum_{l=0}^{\infty}\left(\frac{q}{4\pi\varepsilon_1 R}\left(\frac{a}{R}\right)^l + A_l R^l\right)\left(\frac{2}{2l+1}\delta_{l,l'}\right) = \sum_{l=0}^{\infty}\left(\frac{q}{4\pi\varepsilon_1 R}\left(\frac{a}{R}\right)^l + \frac{B_l}{R^{l+1}}\right)\left(\frac{2}{2l+1}\delta_{l,l'}\right)$$

$$A_l = \frac{B_l}{R^{2l+1}} \tag{3.5}$$

$$\varepsilon_1 \left[\frac{\partial \phi_1}{\partial r}\right]_{r=R} = \varepsilon_2 \left[\frac{\partial \phi_2}{\partial r}\right]_{r=R}$$

$$\varepsilon_1 \sum_{l=0}^{\infty} \left(-\frac{q}{4\pi\varepsilon_1}(l+1)\frac{a^l}{R^{l+2}} + lA_l R^{l-1}\right)\left(\frac{2}{2l+1}\delta\right) = \varepsilon_2 \sum_{l=0}^{\infty} \left(-\frac{q}{4\pi\varepsilon_1}(l+1)\frac{a^l}{R^{l+2}} - (l+1)B_l\frac{1}{R^{l+2}}\right)\left(\frac{2}{2l+1}\delta\right) \tag{3.6}$$

Rearranging and cancelling like terms and substituting $A_l = \frac{B_l}{R^{2l+1}}$ leads to final expressions for A_l and B_l

$$\begin{aligned} A_l &= \frac{q}{4\pi}\left(\frac{\varepsilon_1 - \varepsilon_2}{\varepsilon_1}\right)\left(\frac{l+1}{\varepsilon_2(l+1)+\varepsilon_1 l}\right)\frac{a^l}{R^{2l+1}} \\ B_l &= \frac{q}{4\pi}\left(\frac{\varepsilon_1 - \varepsilon_2}{\varepsilon_1}\right)\left(\frac{l+1}{\varepsilon_2(l+1)+\varepsilon_1 l}\right)a^l \end{aligned} \tag{3.7}$$

Substituting A_l and B_l into Eq. (3.4) leads to complete analytical expressions for the electrostatic potential:

$$\phi(r,\beta) = \begin{cases} \frac{q}{4\pi\varepsilon_1 a}\sum_{l=0}^{\infty}\left(\frac{r}{a}\right)^l P_l(cos\beta) + \frac{q}{4\pi}\sum_{l=0}^{\infty}\left(\frac{\varepsilon_1-\varepsilon_2}{\varepsilon_1}\right)\left(\frac{l+1}{\varepsilon_2(l+1)+\varepsilon_1 l}\right)\frac{a^l r^l}{R^{2l+1}}P_l(cos\beta) & 0 \le r \le a \\ \frac{q}{4\pi\varepsilon_1 r}\sum_{l=0}^{\infty}\left(\frac{a}{r}\right)^l P_l(cos\beta) + \frac{q}{4\pi}\sum_{l=0}^{\infty}\left(\frac{\varepsilon_1-\varepsilon_2}{\varepsilon_1}\right)\left(\frac{l+1}{\varepsilon_2(l+1)+\varepsilon_1 l}\right)\frac{a^l r^l}{R^{2l+1}}P_l(cos\beta) & a \le r \le R \\ \frac{q}{4\pi}\sum_{l=0}^{\infty}\left(\frac{2l+1}{\varepsilon_2(l+1)+\varepsilon_1 l}\right)\frac{a^l}{r^{l+1}}P_l(cos\beta) & R \le r \le \infty \end{cases} \tag{3.8}$$

Simplifying by reducing the Coulomb potential, $\phi_q(r,\beta)$ to its original form shows that this approach agrees completely with the solutions presented by Batygin and Toptygin [102]:

$$\phi(r,\beta) = \begin{cases} \frac{q}{4\pi\varepsilon_1|r-a|} + \frac{q}{4\pi}\sum_{l=0}^{\infty}\left(\frac{\varepsilon_1-\varepsilon_2}{\varepsilon_1}\right)\left(\frac{l+1}{\varepsilon_2(l+1)+\varepsilon_1 l}\right)\frac{a^l r^l}{R^{2l+1}}P_l(cos\beta) & r \leq R \\ \frac{q}{4\pi}\sum_{l=0}^{\infty}\left(\frac{2l+1}{\varepsilon_2(l+1)+\varepsilon_1 l}\right)\frac{a^l}{r^{l+1}}P_l(cos\beta) & R \leq r \leq \infty \end{cases} \tag{3.9}$$

Using the boundary condition that the normal component to the electric field is discontinuous due to the presence of a permanent and free charge on the surface of the sphere, an analytical expression for the surface charge density can be derived:

$$\sigma(R,\theta) = \varepsilon_1\left[\frac{\partial\phi_1}{\partial r}\right]_{r=R} - \varepsilon_2\left[\frac{\partial\phi_2}{\partial r}\right]_{r=R}$$

$$\sigma(R,\beta) = -\frac{q}{4\pi\left|R-a\right|^2} + \frac{q}{4\pi}\sum_{l=0}^{\infty}\left(\frac{\varepsilon_1 + l(3\varepsilon_1-\varepsilon_2)}{\varepsilon_1(\varepsilon_2+l(\varepsilon_1+\varepsilon_2))}\right)\frac{a^l(l+1)}{R^{l+2}}P_l(cos\beta)$$

(3.10)

This analytical expression for the surface charge density as a function of the encapsulated point charge position, can be visualised graphically and then directly compared to DFT calculations to provide assurance of its reliability to model the $Ca@C_{60}$ system.

3.2.1 DFT validation using q@C_{60} and Ca@C_{60}

To visualise the analytical expression, the surface charge density was plotted for a geometric system of properties comparable to that of Ca@C_{60} at a range of charge separations, a, as shown in the Figure 3.3:

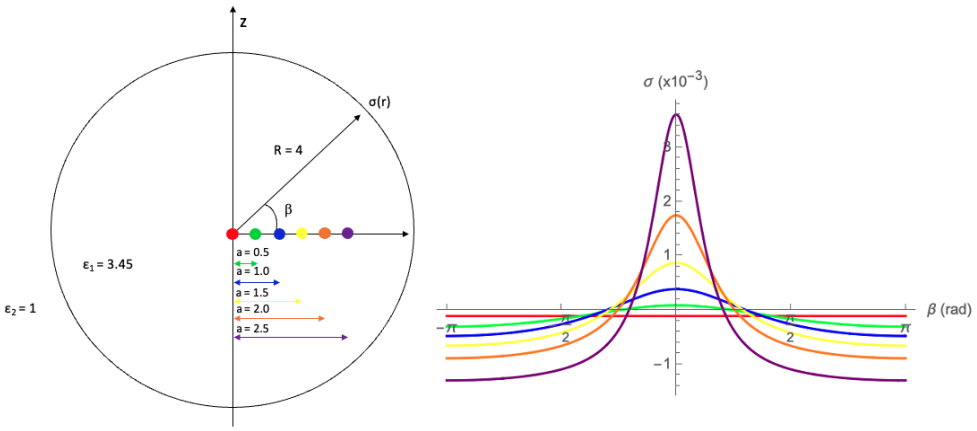

Figure 3.3: Surface charge distributions on a dielectric sphere, of radius (R) 4Å and dielectric constant (ϵ_1) 3.45, immersed in a vacuum (ϵ_2=1), through the placement of a single point charge inside the particle (q = 1.43e). The left-hand illustration defines the system, including the angle from the axis of the point charge (β) and the distance of the point charge from the centre. The right-hand illustration shows the corresponding surface charge distributions as a function of β for various positions of point charge: a = 0Å (red), a = 0.5Å (green), a = 1.0Å (blue), a = 1.5Å (yellow), a = 2.0Å (orange) and a = 2.5Å (purple).

When the point charge is at the centre of the sphere (a = 0Å), the surface charge is uniform, as shown by the red straight line. As the positive point charge moves off centre, towards the surface of the sphere, the surface charge moves across the sphere's surface in the direction of point charge motion due to the electrostatic attraction between the negative surface charge and encapsulated positive point charge. This results in the sphere becoming polarised, with one hemisphere containing more surface charge density than the other. For small values of a (e.g. 0.5Å, green line), the impact on the surface charge is minimal due to the relatively large radius of the sphere, however, as the value of a increases, the impact quickly

becomes more pronounced and concentrated shown by the reducing curve-widths, indicating that the redistributed surface charge is compacted into increasingly smaller surface areas - for this particular system, the surface charge density approximately doubles for every 0.5Å increment, providing good evidence to validate the hypothesis that the motion of an encapsulated charge confined within a dielectric sphere is strongly correlated to the distribution of charge density on the cage surface. To provide additional validation, the model can be compared against DFT calculations for a point charge encapsulated within C_{60}.

Single point energy DFT calculations were performed using the validated computational parameters identified in chapter 4. The first set of calculations modelled a point charge, q of strength +1.43, encapsulated within C_{60}, with locations matching Figure 3.3, to provide a comparable analysis to the analytical model. The resulting output was visualised using the Ovito package [103] with gradient colouring from blue (negative) to red (positive) to clearly visualise the movement of charge across the cage surface.

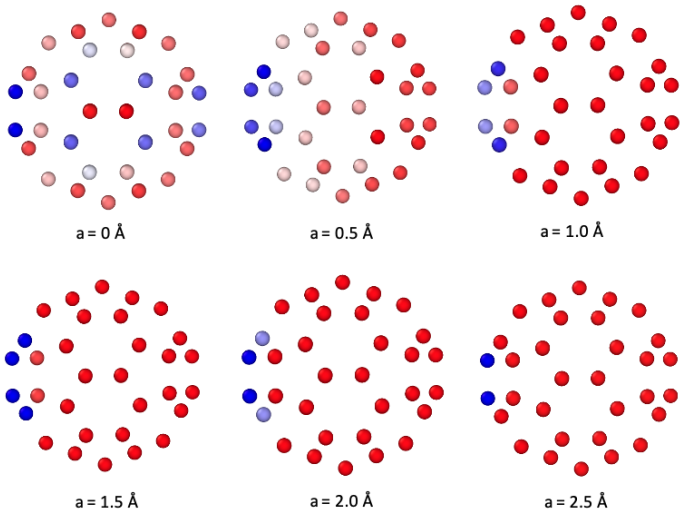

Figure 3.4: DFT calculated partial charges for q@C_{60}, at the B3P86-D3 / cc-pVDZ level of theory. The point charge inside the particle (q = 1.43e) was placed at various locations (a = 0Å - 2.5Å at 0.5Å intervals), moving from right to left hemispheres in the direction of the carbon 6-6 bond.

When the positive point charge is at the centre of C_{60}, the charge distribution is symmetric, as expected due to the electrostatic interaction between the point charge and cage being evenly distributed across the cage. When the point charge moves off centre into the left hemisphere, towards the location of the carbon 6-6 bond, the surface charge redistributes in the same direction. At 0.5 Å, the charge redistribution appears to be spread across the 6 carbons of the hexagon, at 1.0 - 2.0 Å, this reduces to 4 of the 6 carbons within the hexagon, and finally at 2.5 Å, the surface charge is focused on the 6-6 bond. This behaviour closely matches the analytical solution, with the main difference being that the analytical approach does not spread the charge across discrete carbon sites, as the DFT results show, due to the model being of a smooth dielectric sphere. However, for the purposes of establishing whether the analytical approach correctly models behaviour, the close alignment with DFT provides further good evidence of the validity of this approach to support the hypothesis that the motion of the point charge is correlated to the distribution of charge density on the cage surface.

Taking this one step further, to establish the model's alignment with the metallofullerene case, analytical and DFT calculations were undertaken to model $Ca@C_{60}$. The main difference with these calculations was the variability of the strength of the calcium charge at different locations of the cage (observed in Chapter 4 and 5) - the quantity of charge transferred from the calcium ion to the cage surface changes depending on the position of the calcium ion within the fullerene cage, which will have an impact on the electrostatics of the system.

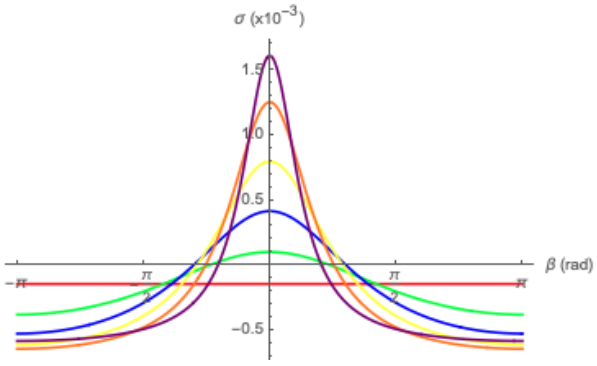

Figure 3.5: Surface charge distributions on a dielectric sphere, of radius (R) 4Å and dielectric constant (ϵ_1) 3.45, immersed in a vacuum (ϵ_2=1), through the placement of a single point charge inside the particle. Corresponding surface charge distributions as a function of β for various positions and point charge strengths: a = 0Å / q = +1.81e (red), a = 0.5Å / q = +1.75e (green), a = 1.0Å / q = +1.56e (blue), a = 1.5Å / q = +1.32e (yellow), a = 2.0Å / q = +1.03e (orange) and a = 2.5Å / q = +0.64e (purple).

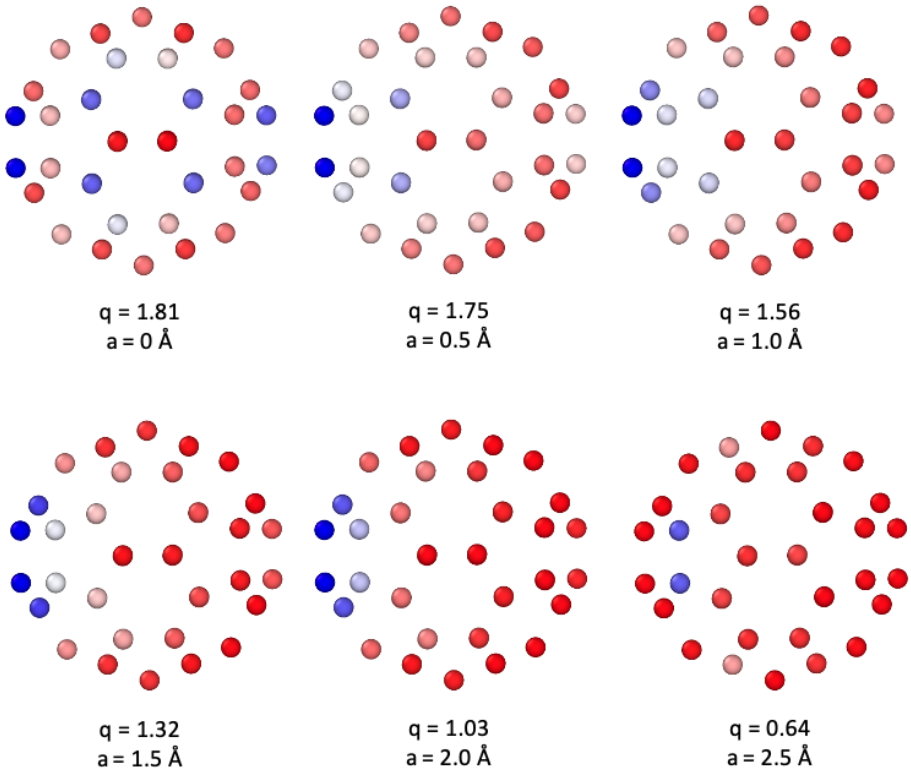

Figure 3.6: DFT derived surface charge distributions of Ca@C_{60}, through the placement of a calcium ion inside the particle (using optimised partial charge values), at various locations (a = 0Å - 2.5Å at 0.5Å intervals), moving into the left hemisphere in the direction of the optimised carbon 6-6 bond.

The analytical solution, in figure 3.5 shows that the reducing charge strength at each interval causes the surface charge density to decrease as a result of a reduced electrostatic attraction between the cage and the point charge. In addition, the profiles of each curve at the extremities (π and -π) are clustered together with similar surface charge densities, indicating that the surface charge is spread over a larger surface area, rather than being compacted as observed in figure 3.3.

The DFT solution, in figure 3.6 shows that when the calcium is at the centre of C_{60}, the charge distribution is symmetric, as expected, and identical to the result of the point charge case. At this position, the strength of the charge is +1.81e. As the calcium moves into the left-hand hemisphere in the direction of the optimised carbon 6-6 bond, charge is transferred to the calcium from the cage non-linearly to a value of +0.64e at 2.5Å. The surface charge again redistributes in the same direction of motion, however, the redistribution appears more gradual, compared to figure 3.4, with a larger spread across the hemisphere. This aligns with the analytical picture, indicating that the degree of polarisation is partially stabilised by the charge transfer process. This reinforces Raggi et al. finding that the stability of the $Ca@C_{60}$ is defined by the interplay between the amount of charge transferred from the metal onto the cage and the degree of polarisation of the surface charge on the cage [17].

This DFT partial charge analysis provides good evidence that the analytical solution presented is a useful and valid approach to model the surface charge polarisation behaviour of the $Ca@C_{60}$ metallofullerene.

3.3 Limitations of analytical solutions

The currently validated analytical solutions available offer a useful holistic electrostatic analysis of surface charge polarisation caused by a free moving charge inside and outside a dielectric sphere. The forms of this work's analytical solution and Raggi's solution, using Legendre polynomials, are similar and so can be used together to compute the distribution of surface charge at either sides of the dielectric particle boundary for a point charge moving across that boundary from inside to outside the cage. There are two limitations to consider when reconciling the results from these analytical solutions to DFT or experimental evidence. The first being the transfer of charge from an encapsulated ion to the cage surface as the ion moves across the cage, as observed in DFT calculations. As shown in the previous section, this can be modelled simply (but manually) by first calculating the charge strength at a specific location using DFT and then inputting those values into the analytical expression to calculate the surface charge distributions. However, this does not take into account the additional quantity of charge that is transferred either from the ion to the cage or vice-versa. But given the delocalised nature of the C_{60} cage, it is assumed that any increasing or decreasing volume of charge is spread across the existing surface charge distribution, having a minimal impact on the overall profile of the surface charge distribution.

The second consideration is that the current analytical solutions do not take into account the electrostatic effects of increasing surface charge surface area concentrations as a result of the point charge moving towards the boundary. In reality, it is unlikely that the surface charge density will tend to a delta-function distribution due to the repulsive effects of the increasingly concentrated localised charge density on the surface. Analysing

this effect is outside the scope of this research, however, Filippov et al. [104], when studying the interaction between particles with inhomogeneous surface charge distributions, derived an analytical expression in terms of Legendre polynomials and a "δ-localised" point charge on the surface of a single uncharged particle, which could be useful to more accurately model surface charge distribution behaviour:

$$\sigma_\delta = \frac{q}{a^2}\frac{\varepsilon_1 - \varepsilon_0}{\varepsilon_1 + \varepsilon_0}\sum_{n=0}^{\infty}\frac{2n+1}{n\varepsilon_1 + (n+1)\varepsilon_0}P_n(cos\theta) - \frac{2q}{\varepsilon_0 a^2}\frac{\varepsilon_1 - \varepsilon_0}{\varepsilon_1 + \varepsilon_0}\delta(cos\theta_0 - cos\theta) \tag{3.11}$$

The additional contribution to the total charge (right-hand term) indicates that the "*environment reacts to the presence of the surface point charge such that the "height" of the δ-function decreases*" [104]. Incorporating this "δ-localised" region of charge into this research's analytical solution could be a useful next step to more accurately model the surface charge distribution of a metallofullerene system.

As an aside, the literature is unclear on the reason behind the precise optimised metal ion position within the fullerene, mostly relying on symmetry arguments (Jahn-Teller distortion) [105] to explain why an off-centre position is more energetically stable rather than a central position. However, this doesn't explain the specific radius of the potential well. This chapter suggests a possible explanation - that the radius of the potential well is the equilibrium position that optimises (1) the electrostatic energy between the encapsulated ion and fullerene cage, (2) the polarisation energy as a result of accumulated charge on the cage surface and (3) the Jahn-Teller distortion energy. This could be an interesting future research direction.

Chapter 4

Computational validation of $Ca@C_{60}$ polarisation properties

Since the discovery of C_{60} in 1985, structural and electronic characterisation work has enabled experimental researchers to consider potential mechanisms to create new molecules, by extending and modifying known reaction pathways that were fine-tuned and optimised for high yield and purity. For this research, focussed on $Ca@C_{60}$, a chronological literature review initially identifies and selects high-yield and experimentally available sterically undemanding functionalised fullerene cages as potential candidates for the development of a bi-stable endohedral metallofullerene molecular switch. The review focuses on hydrogen and fluorine functionalised fullerenes as recommended by Raggi et al. [17]; hydrogen was chosen following a previous study's findings that described how hydrogen addition modified the inner potential energy environment of the fullerene cage and therefore the propensity for an encapsulated species to favour one hemisphere over another [35] resulting in a bi-stable polarisation response from the surface charge density on the cage. Fluorine is an interesting comparative choice

for two reasons, firstly to evaluate the impact of a strongly electronegative species on the fullerene cage's surface charge and secondly, as found in the literature review, the prevalence of high-yield and experimentally available pathways. Encapsulated calcium was chosen as the switching agent, following the previous work by Raggi et al. [17] that demonstrated that calcium ion motion was strongly correlated to the distribution of surface charge density on the fullerene cage, as demonstrated in Chapter 3.

To design a robust testing environment for the selected functionalised fullerene cages, preliminary computational experiments were undertaken to identify and validate appropriate DFT parameters, particularly relevant functionals, basis sets and wave-function analysis methods for ground-state geometry optimisation calculations, single-point energy calculations and partial charge analysis of $Ca@C_{60}$. The experimentally determined electron affinity of the $Ca@C_{60}$ [106] radical was used as an experimental benchmark. To assess the resilience of the functional and basis set choice, further experiments were undertaken to calculate the ionisation energy of another endohedral metallofullerene molecular switch, $Li@C_{60}$, comparing the calculated values to theoretical literature and experimentally determined values. Finally, ground state polarisation and electronic properties were calculated using the selected DFT computational parameters to provide benchmark properties to compare against selected functionalised endohedral metallofullerenes.

4.1 Literature review

4.1.1 Hydrogen functionalised C_{60}

The first hydrogenating reactions on C_{60} used Birch reduction (Li, liquid NH_3, t-BuOH) to create $C_{60}H_{36}$ in 1990 [107]. Note that $C_{60}H_{18}$ was also produced in this reaction, however, it was not clear whether this was a genuine co-product of the Birch reduction or a pyrolysis product of $C_{60}H_{36}$ that followed in the experiment. This was accompanied by the reverse dehydrogenation reaction back to C_{60} by treatment of a toluene solution of the Birch-reduced product with DDQ (reflux), a dehydrogenation agent. The realisation that experimental methods could produce derivatives of C_{60} with a wide range of elements trapped inside the central fullerene cavity generated huge interest in exploring potential new areas of chemistry and materials science.

Following computational research into which low-order hydrogenated fullerene isomers would be preferentially populated at room temperature, Henderson et al. produced $C_{60}H_2$ (1993) and $C_{60}H_4$ (1994) with yields of 20-30% and 10% respectively, through the reaction of C_{60} with BH_3:tetrahydrofuran in toluene followed by hydrolysis and separated by high-performance liquid chromatography (HPLC) [108, 109]. The quality of the separation process was directly correlated with both the yield and purity. The authors note that the total yield of $C_{60}H_4$ was less than 2% from C_{60}, but 10% when $C_{60}H_2$ was used as the starting material. This synthesis, the subsequent isolation in pure form and structural analysis by Nuclear Magnetic Resonance (NMR) spectroscopy provided fundamental information on the structure of C_{60} derivatives, particularly the preference of the initial 1,2 addition and secondary 3,4 addition across a 6-ring to produce $C_{60}H_2$ and

$C_{60}H_4$ respectively, consistent with the thermodynamic isomers predicted from semi-empirical calculations.

The difficulties of efficiently preparing and isolating specific reduced fullerenes was noted in 1996 by Meier et al. due to the large number of adjacent oxidation states[110]. Despite this, Meier successfully synthesised and separated the major isomer of $C_{60}H_6$ by the reaction of C_{60} with Zn-Cu couple at 50°C in toluene containing a small amount of water, of which roughly 50% was isolated by HPLC using a preparative Buckyclutcher column and an automated injector/fraction collector. This was an impressive result, as the reaction produced $C_{60}H_6$ with negligible contamination by adjacent oxidation states. At the time the only example of the highly symmetrical 1,2,33,41,42,50 addition pattern was compared to structures of two other species, $C_{60}Br_6$ [111] and $C_{60}Cl_6$ [112] characterised as 1,2,5,10,21,24 patterns.

By 1997 experimental researchers possessed several established routes to hydrogenated fullerenes. Bergosh et al. noted the following pathways; "*Birch reduction, hydroboration, hydrozirconation, solution phase and solid phase hydrogenation, hydrogenation by addition of hydrogen atoms, transfer hydrogenation, electrochemical reduction as well as chemical reduction with diimide, chromous acetate, photoinduced electron transfer, and with hydride reducing agents*" [113]. These pathways were interesting due to the hydrogenation-dehydrogenation process, particularly used for hydrogen storage systems. The same paper reported an improved isolated yield of $C_{60}H_2$ (66%) and $C_{60}H_4$ (45%) following a similar approach to Henderson, using 250 mg of C_{60} and Zn(Cu) prepared from 5g of Zn dust.

Gakh et al. synthesised and characterised the C_1 (60-70% yield), C_3 (25-30% yield) and T (2-5% yield) isomers of $C_{60}H_{36}$ in 2003 [114]. This was

an important achievement that had defied numerous attempts to characterise the structure of $C_{60}H_{36}$ for over a decade. The three isomers were produced by high-temperature transfer hydrogenation of C_{60} in a 9,10-dihydroanthracene melt, with structures characterised by 2D ^{1}H-detected NMR experiments recorded at 800MHz. This paper provided compelling evidence for straightforward hydrogen migration across the fullerene surface at high temperatures, which supported the case that hydrogenated fullerenes could be useful in the field of hydrogen storage.

In 2005, $C_{60}H_{18}$, previously a minor product of C_{60} hydrogenation reactions, was produced by hydrogenation of C_{60} at 100 bar H_2 pressure and 673K for 10 hours [115]. NMR analysis and Infrared Spectroscopy showed that the crude output (without purification) of this reaction consisted of 95% of the C_{3v} isomer. This overcame the difficulties of producing large amounts of pure single isomeric materials and this technique to synthesise bulk amounts of $C_{60}H_{18}$ hoped to facilitate further research on understanding functionalised C_{60}, now recognised as an important class of materials for solar cell applications [116].

Since its initial production, $C_{60}H_2$ had generated a lot of interest as an effective hole transport material with potential applications in organic field-effect transistors and organic light-emitting devices [117]. In 2009, Tzirakis et al. presented a novel one-step synthesis of $C_{60}H_2$ via hydrolysis of acylated fullerenes [118], improving on previous synthetic approaches by rapidly producing $C_{60}H_2$ with good yield ($> 99\%$) without the need for a separating process. This enabled a pathway for the bulk production of $C_{60}H_2$ for commercial testing and applications.

Continued interest in hydrogen storage capabilities led Luzan et al. to study the kinetics and pathways of the C_{60} reaction with hydrogen gas in

2011 [119], enabling access to higher order hydrogenated fullerenes (known as fulleranes). $C_{60}H_{36}$, $C_{60}H_{44}$ and $C_{60}H_{52}$ were produced via the $C_{60}H_{18}$ intermediary. For this experiment, hydrogenation of C_{60} was performed between 350 – 440°C at 50 bar hydrogen pressure and monitored using the gravimetric method with fullerene products studied by X-ray diffraction, matrix-assisted laser desorption ionisation time-of-flight (MALDI TOF) and atmospheric pressure photoionisation high resolution Fourier transform ion cyclotron resonance (APPI FT-ICR) mass spectrometry, liquid chromatography, and elemental analysis. These experiment revealed products of significantly higher abundance which permitted the suggestion of the reaction pathway, $C_{60} \rightarrow C_{60}H_{18} \rightarrow C_{60}H_{36} \rightarrow C_{60}H_{44} \rightarrow C_{60}H_{52}$, as an access route to higher order fulleranes.

4.1.2 Hydrogen functionalised C_{70}

Concurrently to the work on C_{60}, research was being undertaken on the functionalised of C_{70} fullerenes. In 1998, Spielmann et al., prepared and characterised $C_{70}H_2$, $C_{70}H_4$ and $C_{70}H_8$ using the aforementioned Zn(Cu) reduction technique [120]. The products were purified by HPLC with five bands isolated; C_{70}, $C_{70}H_2$ major isomer (18% yield), $C_{70}H_4$ major isomer (25% yield), three minor isomers of $C_{70}H_4$ (2.9% yield) and $C_{70}H_8$ (27% yield). This study also provided insight into the polyaddition process, particularly that the site of the initial reduction step determines the preferred site of the second reduction step.

4.1.3 Fluorine functionalised C_{60}

Following the discovery of functionalised fullerenes, the fundamental reasons behind observed polyaddition patterns in fullerenes were poorly understood, which motivated researchers to produce a range of functionalised fullerenes to better understand polyaddition processes. The polyaddition patterns fell into three groups; the 1,2 addition of non-bulky groups and 1,2 cycloadditions and 1,4 additions of bulky addends [121]. The 1,2 additions of sterically undemanding groups were of particular importance as they could reveal underlying electronic mechanisms. These groups were limited to hydrogenation and fluorination, whose formation had been shown to take place via a series of 1,2-additions [122–126]. The challenge with experimentally studying hydrogenation, as mentioned in the previous section, is isolating and separating individual products from the reaction mixtures. Hydrogenated fullerenes are also readily oxidised to produce fullerenols, which adds complication when attempting to analyse multiple connected peaks of ^{1}H NMR spectra. Therefore, fluorinated fullerenes developed into a very active area of research to better understand the underlying mechanisms to the polyaddition patterns observed through experiments. Olga Boltalina, now of Colorado State University, has been central to these efforts and in 1996, together with collaborators, prepared and characterised $C_{60}F_{18}$ by the reaction between C_{60} and potassium hexafluoroplatinate (K_2PtF_6) in a Knudsen cell contained within a mass spectrometer and characterised by ^{19}F NMR spectroscopy showing that $C_{60}F_{18}$ had a crown shaped C_{3v} symmetry and was isostructural with $C_{60}H_{18}$. In 2002, Boltalina and Darwish et al. isolated and characterised $C_{60}F_2$, $C_{60}F_4$, $C_{60}F_6$ and $C_{60}F_8$ [121] through fullerene fluorination with K_2PtF_6 at 470°C under vacuum (ca. 0.1 bar). Products were dissolved in toluene, filtered to remove moisture, and then separated by High Pressure Liquid Chromatography. To obtain pure

single products, each fraction was recycled several times to remove tails from earlier fractions. ^{19}F NMR spectra revealed that $C_{60}F_2$ and $C_{60}F_4$ were isometric to their hydrogenated counterparts, with $C_{60}F_6$ exhibiting an S-motif structure, which was interesting as this structure was previously considered as being an intermediate along the pathway to the isostructural $C_{60}H_{18}$ [123]. $C_{60}F_8$ was characterised as having a T-motif structure, and it was found that each fluorine addition increased localisation of the electrons in the addended hexagon, which increased the likelihood of further addition on the hexagon ring. This contrasts with C_{70} hydrogen functionalisation, as the site of the first reduction on the hexagon does not necessarily lead to further addition on the hexagon ring, rather preferring symmetrical arrangements such as additions at opposite poles of the C_{70} cage.

The literature review provides a chronological overview of the production of hydrogen and fluorine functionalised fullerenes that have been experimentally produced, characterised, and purified - summarised in Table 4.1.

Functionalised Fullerene	**Lead Author(s)**	**Year**	**Yield / Purity**	**Isomer Characterisation**
$C_{60}H_n$				
$C_{60}H_2$	Henderson [108]	1994	20-30%	1,2-$C_{60}H_2$
	Bergosh [113]	1997	66%	
	Wang [127]	2005	50%	
	Tzirakis [118]	2009	>99%	
$C_{60}H_4$	Henderson [109]	1994	10%	1,2,3,4-$C_{60}H_4$
	Bergosh [113]	1997	45%	1,2,18,36-$C_{60}H_4$; 1,2,33,50-$C_{60}H_4$
$C_{60}H_6$	Meier [110]	1996	35%	1,2,33,41,42,50-$C_{60}H_6$
	Bergosh [113]	1997	18%	1,2,33,41,42,50-$C_{60}H_6$
$C_{60}H_{18}$	Wagberg [115]	2005	95%	Not specified
	Luzan [119]	2011	95%	C_{3v}
$C_{60}H_{36}$	Gakh [114]	2003	70%, 25%, 5%	C_1, C_3, T
$C_{60}F_n$				
$C_{60}F_2$	Boltalina [121]	2002	100%	1,2-$C_{60}F_2$
$C_{60}F_4$	Boltalina [121]	2002	100%	1,2,3,4-$C_{60}F_2$
$C_{60}F_6$	Boltalina [121]	2002	100%	S, T
$C_{60}F_8$	Boltalina [121]	2002	100%	T
$C_{60}F_{18}$	Boltalina [126]	1996	100%	C_{3v}
$C_{70}H_n$				
$C_{70}H_2$	Spielman [120]	1998	18%	1,2-$C_{70}H_2$
$C_{70}H_4$	Spielman [120]	1998	25%	1,2,56,57-$C_{70}H_2$
$C_{70}H_8$	Spielman [120]	1998	27%	7,19,23,27,33,37,44,53-$C_{70}H_8$
$C_{70}H_{10}$	Spielman [128]	2000	35%	7,8,19,26,33,37,45,49,53,63-$C_{70}H_{10}$

Table 4.1: Literature review of candidate hydrogenated and fluorinated functionalised fullerene cages that have been experimentally produced, characterised, and purified.

To refine the literature review into a group of testing molecules, this research will primarily focus on pairs of additive hydrogen and fluorine functionalised fullerenes that are experimentally available in reasonable yield. In an ideal situation the pairs will be isostructural with respect to functionalisation, but in cases they are not, the isomer choice of each pair will be led by the molecule that is available in the highest yield so that functionalised group comparisons can be made and underlying polarisation and switching mechanisms can be investigated, limiting the number of changing variables.

The 1,2-$C_{60}H_2$ and 1,2-$C_{60}F_2$ pair is both isostructural and available in excellent yield (>99%). 1,2,3,4-$C_{60}H_4$ and 1,2,3,4-$C_{60}F_4$ are isostructural and available in reasonable yield (45% and 100% respectively). S-$C_{60}F_6$

and its hydrogenated counterpart, 1,2,33,41,42,50-$C_{60}H_6$ (major isomer) are experimentally available in reasonable yields (100% and 35% respectively). Cahill's ab initio calculations in 1996 [129] identified the S-motif 1,2,3,4,9,10-$C_{60}H_6$ as one of the lowest energy isomers and therefore this isostructural isomer will be tested and compared against the analogous fluorinated endohedral fullerene. T-$C_{60}F_8$ is experimentally available at high-yield, but interestingly, $C_{60}H_8$ is not experimentally available and has never been isolated, despite acknowledgement of its existence as an intermediate to more highly hydrogenated species [130]. However, in line with the selection criteria, the T-$C_{60}H_8$ structure will be tested to compare against the analogous fluorinated endohedral fullerene. The following table summarises and justifies the selected functionalised cages investigated in this study:

Selected Functionalised Fullerene	**Justification**
1,2-$C_{60}H_2$ and 1,2-$C_{60}F_2$	Experimentally available high-yield molecules that are isostructural with respect to functionalisation
1,2,3,4-$C_{60}H_4$ and 1,2,3,4-$C_{60}F_4$	
S-$C_{60}H_6$ and S-$C_{60}F_6$	S-$C_{60}F_6$ experimentally available at high-yield.
	Ab-initio calculations indicate that S-motif 1,2,3,4,9,10-$C_{60}H_6$ is one of the lowest energy isomers of $C_{60}H_6$.
T-$C_{60}H_8$ and T-$C_{60}F_8$	T-$C_{60}F_8$ experimentally available at high-yield.
	$C_{60}H_8$ is not currently experimentally available, but is a known intermediary to higher-order fullerenes. The T-$C_{60}H_8$ isomer will be tested as a comparison

Table 4.2: Selected hydrogenated and fluorinated C_{60} cages for study

This section has successfully identified and selected experimentally available and sterically undemanding functionalised fullerenes for calcium to be encapsulated within as potential candidates for a polarisation molecular switch.

4.2 DFT computational parameter selection and validation

To test the polarisation response of the selected candidate functionalised fullerenes, DFT was used as a quantum chemical tool to predict polarisation properties, particularly ground state geometries and surface charge polarisation. But first and importantly, to construct a robust DFT experiment, relevant computational parameters must be explored and validated to give assurance that the level of theory selected produces chemical property predictions that can be legitimately compared to experimental evidence.

As a first step, singlet, and triplet geometry optimisation calculations were performed on the selected cages to identify the singlet-triplet gap as an indicator of biradicaloid character and therefore general appropriateness of DFT as a tool for predicting polarisation properties of functionalised metallofullerenes. Singlet and triplet geometry optimisation calculations were calculated for the selected functionalised fullerenes and calculated ground state energies were compared to evaluate the singlet-triplet gap.

Molecule	**Singlet - Triplet Gap (eV)**	
	X=H	**X=F**
$Ca@C_{60}$	0.05	0.05
1,2-$Ca@C_{60}X_2$	0.06	0.06
1,2,3,4-$Ca@C_{60}X_4$	0.13	0.13
S-$Ca@C_{60}X_6$	-0.08	-0.06
T-$Ca@C_{60}X_8$	-0.41	-0.49

Table 4.3: Singlet – triplet gap calculations for selected hydrogenated and fluorinated C_{60} cages at the B3P86-D3 / cc-pVDZ level of theory.

The singlet-triplet gap predicted for the selected molecules range between ± 0.05 eV and 0.49 eV. This is within Lee and Head-Gordon's [131] identified singlet-triplet energy gap, potentially indicating biradicaloid nature. As mentioned in chapter 2, this research follows the line of reasoning suggested that whilst there might be evidence of correlation in smaller fullerenes, C_{60} is a weakly correlated system, aligning with experimental evidence of paramagnetic silence [93]. To verify this, optimisation calculations were performed on $Ca@C_{60}$ and $[Ca@C_{60}]^+$ using Q-Chem's inbuilt Unrestricted Hartree-Fock method (UHF). Both methods computed identical ground state energies and an ionisation energy of 6.2 eV. In addition, spin-projection values calculated were consistent with singlet, rather than triplet states, and therefore, in the context of geometry optimisation and ionisation energies, the degree of electron correlation appears not to affect computed electronic properties. This aligns with the view that C_{60} is a weakly correlated system, and so DFT is deemed an appropriate tool to continue this research.

To select the appropriate level of DFT theory, a range of functionals and basis sets were tested on $Ca@C_{60}$ using geometry optimisation calculations to determine the electron affinity and ionisation energy with comparisons to experimental evidence. These calculations produce a minimum electronic ground state energy (and associated electronic structure) and molecular configuration (geometric structure).

4.2.1 Exchange correlation functionals

A literature review was undertaken to establish common exchange correlation functionals used to study fullerenes and endohedral fullerenes. Those functionals were assessed against studies that review and compare func-

tionals in different chemical contexts. B3LYP [39, 40, 132] was found to be a popular and well established starting point functional, however, a recent paper [85] reviewing the advanced GMTKN55 database for general main group thermochemistry, kinetics and non-covalent interactions, found it to be the worst of 23 hybrid functionals for the calculation of reaction energies. Another paper argues that the standard B3LYP / 6-31G* model chemistry should not be used in DFT calculations of molecular thermochemistry [133]. The hybrid GGA functionals, PBE0 and B3P86, are referenced in the literature [38, 82, 134, 135] as useful functionals to probe encapsulated C_{60} species. PBE0 is referenced as a slower hybrid functional that overcomes several technical issues when calculating endofullerene electronic structure calculations. In addition, a recent study [136] also found the range separated GGA ωB97X useful in theoretical studies of $HF@C_{60}$. Dispersion corrections were reported as essential for the study of chemical reactivity of fullerenes [137]. This parameter can be implemented using the Grimme "DFT-D3" and "DFT-D3(BJ)" dispersion correction within the Q-Chem software package, as discussed in Chapter 3. Based on the literature review, the functionals selected for validation testing were all hybrid GGA functionals — B3LYP, B3LYP-D3, PBE0-D3, B3P86-D3 and ωB97X-D3.

4.2.2 Basis sets

The Pople basis set 6-31G* [40, 41] was found to be a popular starting point for many researchers. However, in the context of a functionalised metallofullerene polarisation switch, ensuring that the basis set contains diffuse functions is important, especially with regard to hydrogen bonding for the hydrogen functionalised fullerene cages. In addition, because of charge transfer from the metal encapsulated species to the fullerene cage,

the fullerene cage is negatively charged. Several papers [138–140] discuss the merits of using diffuse basis sets to properly describe the non-covalent interactions involving anions, and conclude that "*the omission of diffuse functions appears to have a negligible effect while calculating geometry parameters or total energy; thus, acceptable results may be obtained without them*" [140]. To assess this impact, the basis sets selected for validation testing were 6-31G*, 6-311G*, 6-31++G** and cc-pVDZ.

Reflecting on the knowledge gained in Chapter 3 regarding basis set theory, the basis set selection tests the impact of the exclusion or inclusion of different mathematical components in an attempt to best describe the $Ca@C_{60}$ system with respect to a linear combination of atomic orbitals, representing the system's molecular orbitals. The Pople basis sets (6-31G*, 6-311G*, 6-31++G**) all use 6 Gaussians to expand the 1s core of elements in the second period of the Periodic Table. 6-31G* is a double-zeta basis set (two basis functions for each valence atomic orbital) and includes d polarisation functions on non-hydrogen atoms. 6-311G* is a triple-zeta basis set (three basis functions for each valence AO), adding another Gaussian to 6-31G* and also includes d polarisation functions. 6-31++G** tests the importance of the inclusion of diffuse functions to the s and p shells (for elements Li-Cl), denoted by "+" and a single diffuse s orbital to hydrogen, which might be useful when investigating hydrogenated $Ca@C_{60}$. The Dunning basis set, cc-pVDZ, is a double-zeta basis that includes polarisation functions and also correlation consistent basis sets that are optimised using "*Configuration Interaction Singles and Doubles*" (CISD) wave functions, a post-HF approach [54]. Given the ongoing debate to the degree of correlation within C_{60}, including a correlation consistent basis set seems a sensible approach to acknowledge this debate within the testing environment.

4.2.3 Functional and basis set validation

In order to validate the most appropriate functional and basis set combination, geometry optimisation calculations were performed on singlet and triplet states of $Ca@C_{60}$ and $[Ca@C_{60}]^-$ and compared to the experimentally calculated electron affinity of 3.00 ± 0.10 eV [23] determined by ultraviolet photoelectron spectroscopy. Three rounds of computational experiments were performed across the range of selected functionals and basis sets with the goal to converge on an appropriate and valid functional and basis set combination, to accurately predict the electron affinity of $Ca@C_{60}$; Round 1 tested the selected functionals using the 6-31G* basis set. Round 2 tested the selected functionals using the 6-311G* and 6-31++G** basis sets. Round 3 tested the most accurate functionals using the 6-311G*, cc-pVDZ and 6-31++G** basis sets, supplemented by frequency analysis to confirm the global potential energy minimum. The results are shown in Table 4.4.

Functional	**Basis set**			
	6-31G*	**6-311G***	**6-31++G****	**cc-pVDZ**
B3LYP	2.37 eV	2.80 eV	2.75 eV	2.64 eV
B3LYP-D3	3.82 ev	2.80 eV	2.81 eV	2.64 eV
PBEO-D3	2.54 eV	2.88 eV	2.85 eV	2.77 eV
B3P86-D3	2.73 eV	3.12 eV	3.06 eV	2.98 eV
ωB97X-D3	2.26 eV	2.63 eV	2.59 eV	2.52 eV
Experimental	3.00 ± 0.10 eV	3.00 ± 0.10 eV	3.00 ± 0.10 eV	3.00 ± 0.10 eV

Table 4.4: $Ca@C_{60}$ geometry optimisation calculations at progressive levels of theory with respect to the accuracy of the experimentally determined electron affinity of the $Ca@C_{60}$ radical.

Despite the popular use of the B3LYP functional across computational chemistry, B3LYP did not produce an accurate prediction for the elec-

tron affinity of $Ca@C_{60}$. This reinforces findings in the literature review that B3LYP should not be used in DFT calculations of molecular thermochemistry [133]. These experiments indicate that either the B3P86-D3 / 6-31++G** or B3P86-D3 / cc-pVDZ levels of theory provide an accurate prediction for the experimentally calculated electron affinity for the $Ca@C_{60}$ radical, comfortably within experimental error. Note that cc-pVDZ produced slightly lower electron energies compared to 6-31++G** and across all calculations produced the most accurate electron affinity of 2.98 eV compared to experiment. Frequency analysis also confirmed that at these levels of theory real frequencies are predicted, giving confidence that the geometries optimised are at a potential energy minimum. To test which basis set, 6-31++G** or cc-pVDZ, is the most appropriate for polarisation calculations, additional energetic and partial charge analysis was undertaken.

Firstly, ionisation energy calculations were undertaken at the B3P86-D3 / 6-31++G** and B3P86-D3 / cc-pVDZ levels of theory and compared against computational and experimental determinations of the first ionisation energy of $Ca@C_{60}$, $Li@C_{60}$ and C_{60}. $Li@C_{60}$ was tested as another experimentally available metallofullerene that is recognised in the literature as a multi-state molecular switch. The ionisation energy of $Ca@C_{60}$ was calculated using a method of differences between the singlet ground state energy of $Ca@C_{60}$ and $[Ca@C_{60}]^+$ and repeated for $Li@C_{60}$ and C_{60}. Results are shown in Table 4.5.

Molecule	**Ionisation Energy (eV)**				
	6-31++G**	**cc-pVDZ**	**6-311G***	**Comp. [36]**	**Exp.**
$Ca@C_{60}$	6.2	6.2	6.3	6.1	N / A
$Li@C_{60}$	6.1	6.1	6.2	6.1	6.5 ± 0.1 [141, 142]
C_{60}	7.8	7.7	7.8	7.7	7.6 ± 0.1

Table 4.5: Ionisation energy calculations using the B3P86-D3 functional and 6-31G++**, cc-pVDZ and 6-311G* basis sets compared to computational and experimental literature for $Ca@C_{60}$, $Li@C_{60}$ and C_{60}.

The ionisation energies calculated for both 6-31++G** and cc-pVDZ were identical and in good agreement with computational literature values for all for $Ca@C_{60}$ and $Li@C_{60}$. When compared to experimental values, the ionisation energy for $Li@C_{60}$ was underestimated by 6%. Yagi et al. commented that "*the ionisation potential of $Li@C_{60}$ is estimated to be 1.1 eV smaller than that of C_{60}, which is the result of electron transfers to the C_{60} cage*" [141] in agreement with gas phase experiments. Comparing to computational results, the ionisation potential of $Li@C_{60}$ is estimated to be 1.7 – 1.8 eV smaller than that of C_{60} suggesting that computational methods used in the literature are not accurately evaluating the valence electron binding energy. In the case of C_{60} (6-31++G** only), the calculated ionisation energy was in reasonable agreement (2% difference) compared to the computational and experimental literature values.

4.2.4 Partial charge method

Partial charge calculations were undertaken using a range of methods to identify an appropriate method to calculate $Ca@C_{60}$ partial charges and surface charge polarisation. The Q-Chem package provides a range of partial charge population analysis methods. This study initially tested three

approaches; Mulliken [143], charges from the Electrostatic Potential on a Grid (CHELPG) [144] and Hirshfeld Charge Model 5 (CM5) [145]. Mulliken population analysis is the default methodology offered in Q-Chem but is recognised to be heavily dependent on the basis set and can produce non-physical negative numbers of electrons along with high basis set dependence [146]. CHELPG is often seen as a more stable alternative to Mulliken analysis, using atom-centred charges that best fit the molecular electrostatic potential. However, CHELPG often suffers from an "inner atom" problem when applied to larger molecules as the inner atomic charges don't affect the molecular electrostatic potential and so can cause an over-fitting issue, leading to inaccurate partial charges [144]. Hirshfeld CM5 uses a parameterised mapping of the Hirshfeld population analysis [145] to correct the underestimation of charges produced by the Hirshfeld approach while remaining weakly basis set dependent. CM5 charges have also been found to perform well for solvation energy calculations [147, 148]. The partial charge calculations were performed on optimised geometries of $Ca@C_{60}$ using the B3P86-D3 functional and 6-31G*, 6-31++G** and cc-pVDZ basis sets to assess the impact of basis set on the predicted partial charge. The results are shown in Table 4.6:

Method	**Basis Set**			
	cc-pVDZ	**6-31++G****	**6-31G***	**6-311G***
Mulliken	1.48	2.47	1.37	1.40
CHELPG	1.29	1.33	1.15	1.39
Hirshfeld CM5	0.93	0.97	0.88	0.96

Table 4.6: $Ca@C_{60}$ partial charge analysis using Mulliken, CHELPG and Hirshfeld CM5 methods and 6-31G*, 6-311G*, 6-31++G** and cc-pVDZ basis sets at the B3P86-D3 level of theory. Charge units are e.

6-31G* produced smaller partial charges, compared to cc-pVDZ and 6-

31++G** indicating that the inclusion of diffuse functions is most likely required for this endohedral metallofullerene system. The Mulliken analysis produced higher partial charges across the three basis sets when comparing against a literature Mulliken population calculations of 1.27e [132]. The CHELPG method produced partial charges aligned to the literature Mulliken value with a stable response across basis sets. However, the unknown contribution due to the "*inner-atom issue*" reduces confidence in this approach. The partial charges predicted by the Hirshfeld CM5 approach are smaller than those produced by the Mulliken and CHELPG approaches and are also reasonably consistent across basis-sets and without the concern of an "*inner-atom*" issue. However, comparing to literature partial charge values, the Hirshfeld CM5 calculation suggests that only one 4s electron is transferred to the fullerene cage which goes against experimental evidence that two electrons are transferred to the cage with a "*back-donation*" effect to result in a partial charge between +1e and +2e. However, an alternative explanation could be that the overlap of the cage electron density and the central atom is larger than previously calculated.

To extend this testing, a translational analysis was undertaken to test how the basis sets respond to the partial charge methods when the calcium is moved in a straight-line across the cage. In this case, single point energy and partial charge calculations were performed on optimised geometries of $Ca@C_{60}$ at the B3P86-D3 / 6-31++G** functional and B3P86-D3 / cc-pVDZ level of theory. Results are shown in Figure 4.1.

In general, the CHELPG and Hirshfeld CM5 methods produced similar results using 6-31++G** and cc-pVDZ. CHELPG produced partial charges in line with literature ranges between 0.35 Å and the optimised calcium position, 1.18 Å. However, for radial distances of 0.00 Å – 0.35 Å the partial charges blow up to 20e suggesting that all calcium electrons are transferred

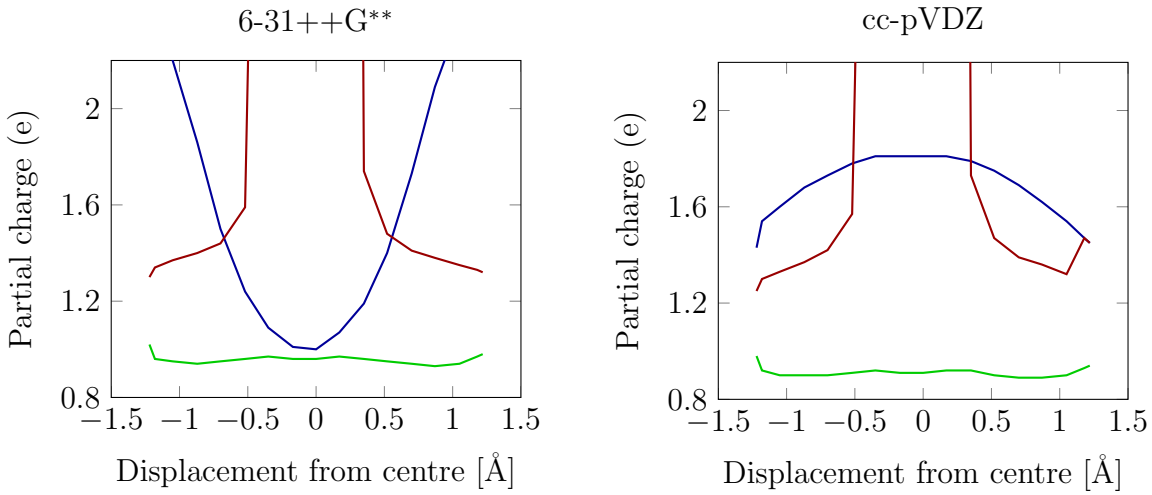

Figure 4.1: Calcium partial charges calculated across the C_{60} cage using Mulliken (blue), CHELPG (red) and Hirshfeld CM5 (green) methods at the B3P86-D3 / 6-31++G** and B3P86-D3 / cc-pVDZ level of theory.

to the cage, which seems highly unlikely and potentially a consequence of the inner-atom issue. Hirshfeld CM5 produced a restrained response for both 6-31++G** and cc-pVDZ with partial charges between 0.93e and 1.02e for all radial distances tested, lower than literature values as discussed previously. Interestingly, the Mulliken analysis produced partial charges of 2.48e (6-31++G**) and 1.29e (cc-pVDZ) and opposing profiles. The 6-31++G** profile suggests that more than two electrons are donated to the cage with charge being transferred to the cage as the calcium moves from the centre to the cage wall. The cc-pVDZ profile suggests partial charges within literature ranges of 1.27e – 1.81e, with charge being transferred to the calcium as it moves from the centre to the cage wall.

When the Mulliken results are mapped to the potential energy profile, 6-31++G** exhibits an inverse relationship, i.e. for higher energy calcium positions at the centre, charge is transferred to the calcium. cc-pVDZ exhibits a proportional relationship, i.e. for central calcium positions, charge is transferred to the cage. This is demonstrated in Figure 4.2.

Central calcium positions are known to be of higher symmetry, with the

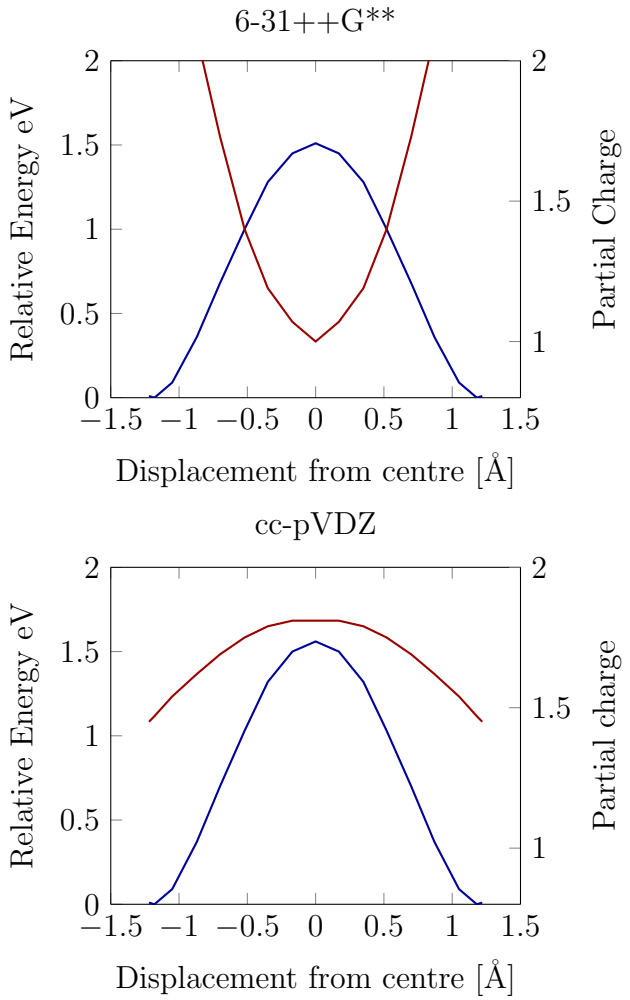

Figure 4.2: Single point energy (blue) and partial charge (red) calculations across the fullerene cage at the B3P86-D3 / 6-31++G** and cc-pVDZ level of theory (axes relate to both graphs).

actual centre being of I_h symmetry. Previous calculations by Lu et al. in 1999 [26] on the I_h configuration predict a larger calcium partial charge of 1.67e, indicating that cc-pVDZ is more accurate than 6-31++G**. This suggests that for higher energy positions near the centre of the fullerene cage, energy is required to transfer charge from the cage to the calcium, resulting in a greater back-donation effect and therefore greater mixing of the fullerene and calcium charge density. This higher energy requirement again reinforces the stabilisation effect that charge transfer from the calcium to the cage has on the overall system. Please also note that calculated cc-pVDZ energies were on average 4.4 eV lower than 6-31++G**.

The translational analysis indicates that the cc-pVDZ basis set is preferable to the 6-31++G** basis set when using the Mulliken approach to calculate partial charges. It should be noted that choosing the most appropriate partial charge methodology for electronic and electrostatic analysis is difficult as the often-cited methodologies each come with their own limitations as described (e.g. basis set dependence, inner-atom issues etc.). To overcome these challenges, a recently published partial charge method can be used to cross-reference the results; the Density Derived Electrostatic and Chemical (DDEC) approach, with the most recent iteration being DDEC6 [149]. The DDEC6 method is a charge partitioning algorithm functional of the electron and spin distributions, with no basis set dependence. It was designed with nine specific performance goals in mind for assigning net atomic charges (NACs), specifically to overcome the issues found in existing approaches:

1. Exactly one assigned electron distribution per atom.
2. Core electrons remain assigned to the host atom.
3. NACs are functionals of the total electron density distribution.
4. Assigned atomic electron distributions give an efficiently converging polyatomic multipole expansion.
5. NACs usually follow Pauling scale electronegativity trends.
6. NACs for a particular element have good transferability among different conformations that are equivalently bonded.
7. The assigned NACs are chemically consistent with the assigned atomic spin moments.
8. Predictably rapid and robust convergence to a unique solution.

9. Computational cost of charge partitioning scales linearly with increasing system size.

Helpfully, the article describing the DDEC6 approach performs tests on $Li@C_{60}$ and predicts a partial charge value of 0.90e, indicating that one electron is transferred to the cage, in line with experimental evidence [150]. This was compared in the article to Hirshfeld CM5 that predicts 0.57e, demonstrating the limitations of this method. Recent testing of the DDEC6 approach, by the University of Nottingham Computational Nanoscience Group at the B3P86 / 6-311G* level of theory, calculated the partial charge on lithium for $Li@C_{60}$ as 0.91e and on calcium in $Ca@C_{60}$ at 1.43e. Given this method overcomes basis set dependence, these unpublished results have been compared to Table 4.6, demonstrating alignment to Mulliken and CHELPG partial charge calculations. Given CHELPG produces non-physical charges when the calcium is moved across the cage, this indicates that Mulliken is the most appropriate method for assigning net atomic charges from the traditional set of methods for this system. Repeating the $Ca@C_{60}$ translational analysis using DDEC6 (see Figure 4.3), the DDEC6 profile matches the Mulliken profile, reinforcing the view that for the partial charge analysis of $Ca@C_{60}$, Mulliken is a useful and cost-effective computational choice if DDEC6 is unavailable.

Extending this analysis to functionalised cages, additional DDEC6 and Mulliken partial charge calculations were performed on all selected functionalised cages holding encapsulated calcium at the B3P86-D3 / cc-pVDZ level of theory. The results can be seen Table 4.7.

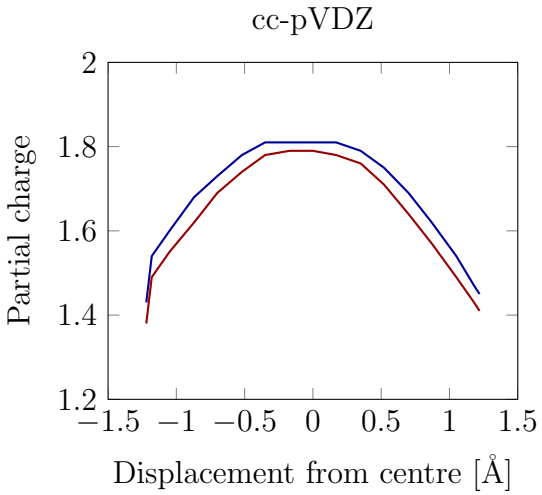

Figure 4.3: Partial charge calculations across the fullerene cage at the B3P86-D3 / cc-pVDZ level of theory and Mulliken (blue) and DDEC6 (red) net atomic charges.

Method	**$Ca@C_{60}$=A**	**1,2-AX_2**	**1,2,3,4-AX_4**	**S-AX_6**	**T-AX_8**
	X = H				
DDEC6	1.43	1.47	1.54	1.47	1.58
Mulliken	1.48	1.51	1.57	1.50	1.60
	X = F				
DDEC6	1.43	1.50	1.65	1.53	1.68
Mulliken	1.48	1.54	1.66	1.55	1.65

Table 4.7: Calcium partial charges calculated using DDEC6 and Mulliken methods at the B3P86-D3 / cc-pVDZ level of theory across selected functionalised endohedral metallofullerenes.

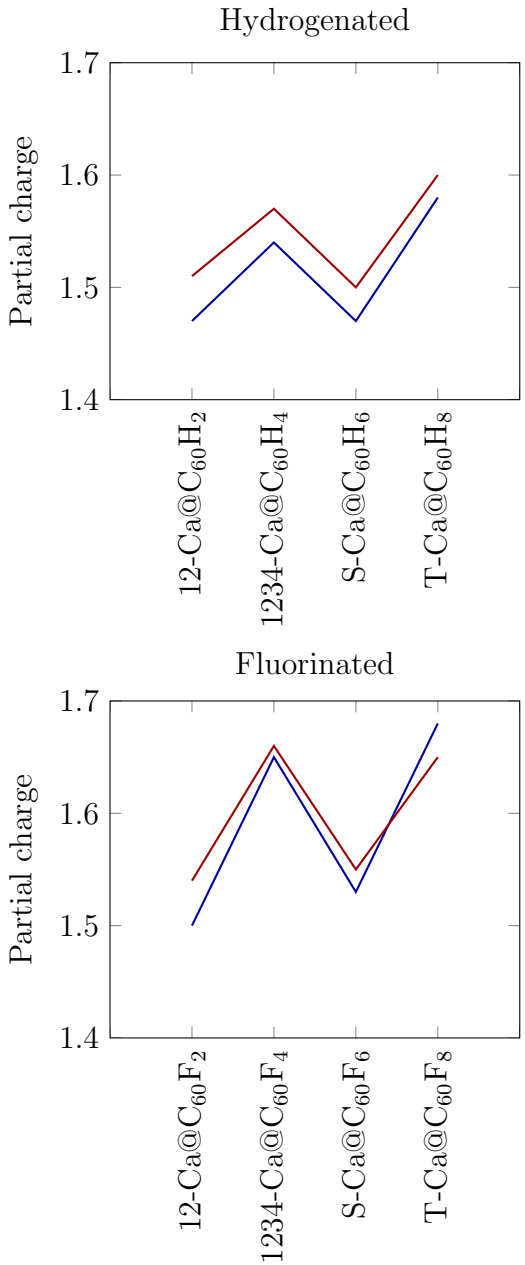

Figure 4.4: Calcium partial charges calculated using DDEC6 (blue) and Mulliken (red) methods at the B3P86-D3 / cc-pVDZ level of theory.

Across the calcium partial charge series, both DDEC6 and Mulliken have the same profile. DDEC6 predicts slightly lower partial charges for both hydrogenated and fluorinated molecules, with T-$Ca@C_{60}F_8$ being the only exception. On the whole, both methods produce similar results, reinforcing the view that both methods can be useful for these systems. However, given DDEC6 was designed to overcome the limitations of current traditional

methods, and Mulliken is well-known to have basis set dependence issues, the DDEC6 method shall be used going forward in this research, however, it should be noted that Mulliken provided similar results at this level of theory and can be used as a cost-effective partial charge analysis tool for future work.

In summary, the B3P86-D3 / cc-pVDZ level of theory demonstrates an excellent degree of accuracy when calculating $Ca@C_{60}$ electron affinity, a reasonable degree of accuracy when calculating ionisation energies for $Ca@C_{60}$ and $Li@C_{60}$ and a more physically realistic partial charge behaviour (compared to B3P86-D3 / 6-31++G**). DDEC6, used in conjunction with the B3P86-D3 / cc-pVDZ level of theory, is a useful approach, overcoming traditional partial charge method issues to predict the system partial charges in line with computational and experimental values from the literature for $Ca@C_{60}$ and $Li@C_{60}$. Therefore, these three computational parameters are selected as robust and resilient choices to calculate geometric and polarisation properties of $Ca@C_{60}$ and functionalised $Ca@C_{60}$ and shall be used in this research going forward.

Reflecting on this chosen level of theory, it is worth being reminded of the components that make up this exchange functional and basis set combination. The exchange functional B3P86 is a hybrid GGA functional with exchange and correlation components provided by Becke [38] and Perdew [82]. cc-pVDZ is a double-zeta basis set that incorporates polarised functions in a correlation consistent manner, demonstrating the importance of the polarisation of the orbital electron distributions and larger diffuse orbitals that take into account the C_{60} anion in the $Ca^{+}@C_{60}$ system. This basis set also demonstrates a more realistic modelling of the charge transfer process between the calcium ion and the C_{60} cage.

4.3 $Ca@C_{60}$ polarisation properties

Using the defined computational parameters, DFT geometry optimisation calculations on both singlet and triplet states of $Ca@C_{60}$ predict the ground state to be an optimised singlet state with the calcium located 1.18 Å from the centre, aligned with the midpoint of one of the 6–6 bonds, as shown in the right-hand illustration of figure 4.5. Literature values for the radial position range between 0.7 Å - 1.22 Å and so the prediction of 1.18 Å is considered reasonable and consistent.

Calcium Position	**Calcium Radial Position (Å)**	**Calcium Partial Charge**	**Fullerene Cage Partial Charge**
6-6 midpoint	1.18	1.43	-1.43

Table 4.8: Calculated ground state primary polarisation properties for $Ca@C_{60}$ with respect to the calcium location inside the fullerene cage.

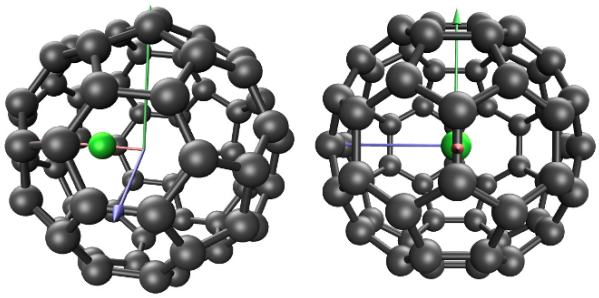

Figure 4.5: Visual representation of ground state $Ca@C_{60}$ to show the calcium off-centre radial position (LHS) and calcium alignment with the 6-6 bond.

The degree of aromaticity across the structure is important to consider when seeking to understand both the calcium ion position and the preferred addition sites during the formation of hydrogen and fluorine functionalised fullerenes. Chemical bond studies on fullerene systems using a valence bond treatment of the Heisenberg Hamiltonian indicate a preference of π-electron density to lie on 6–6 bonds [92] indicating an electrostatically favourable

position for both the encapsulated positively charged calcium ion and as an addition site for the first H_2 and F_2 additions of C_{60}, as mentioned previously. The calculated calcium partial charge of +1.43e supports the existing view that in the process of formation, two electrons are transferred to the cage with a back-donation effect due to a degree of delocalisation of the fullerene electron density and overlap with the central calcium atom.

The translational analysis of DFT single point energies and partial charges is shown in Figure 4.6, demonstrating the impact of functionalisation on the internal potential energy profile and energy barriers between the two minima in each hemisphere.

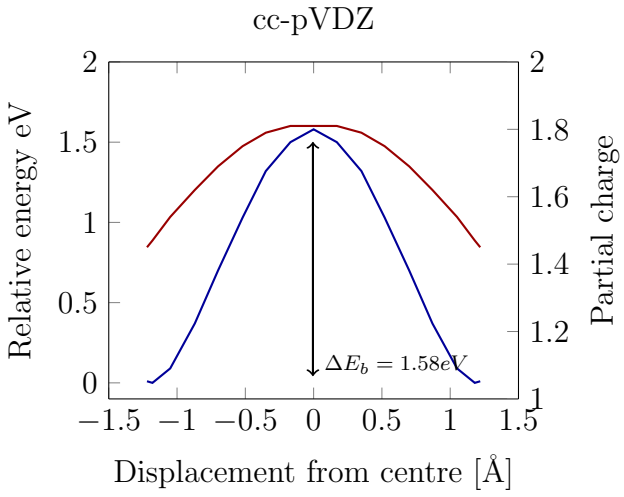

Figure 4.6: $Ca@C_{60}$ radial relative potential energy (blue) and partial charge profile (red) at the B3P86-D3 / cc-pVDZ level of theory.

The potential energy profile takes the familiar symmetrical Mexican-hat form, with the minimum located 1.18 Å from the centre of the fullerene cage, where the ground calcium ion is located. As discussed previously, the DDEC6 net atomic charges indicate that at higher energy positions near the centre of the fullerene cage, energy is required to transfer electrons from the cage to the calcium, resulting in a greater back-donation effect and therefore greater mixing of the fullerene and calcium charge density. The maximum energy barrier, 1.58 eV, remains in the centre of the molecule. The partial

charge profile (an inverse parabola for $Ca@C_{60}$) becomes asymmetrical, with the maximum (+1.79e) shifting into the functionalised hemisphere. The asymmetrical distribution of surface charge can clearly be seen in the visualisation, Figure 4.7, using the open-source Ovito visualisation software [103]:

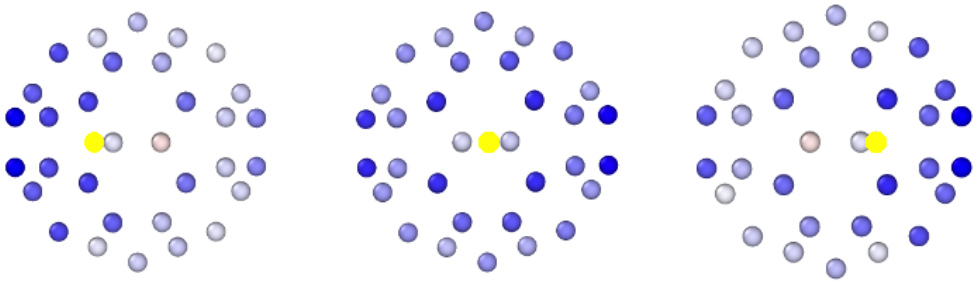

Figure 4.7: Distribution of partial atomic charge for three different positions of the calcium atom (yellow particle inside cage) in $Ca@C_{60}$. The lower energy minima (LHS), calcium at the centre (middle), and the higher energy minima (RHS). The carbon atoms are depicted according to the charge they carry: red (positive) and blue (negative).

When the calcium is located at the lowest energy minima position in the left-hand hemisphere, an accumulation of charge is clearly observed in this hemisphere. As the calcium moves to the centre of the cage, the surface charge distributes more evenly throughout the cage. When the calcium moves into the right-hand hemisphere, to the opposite minima position, the surface charge follows the calcium ion, also shifting into the right-hand hemisphere. To understand this motion further, the surface polarisation charge on each hemisphere was plotted as a function of the position of the calcium ion, Figure 4.8.

The polarisation charge in each hemisphere is negative for all radial positions of calcium. Focusing on the left-hemisphere (dotted line), at the lowest energy minimum, where the calcium is displaced -1.18Å from the cage centre, the polarisation charge is -1.11e with net charge transfer being $Ca^{1.49+}@C_{60}^{1.49-}$. As the calcium moves to the energy maximum at the cage

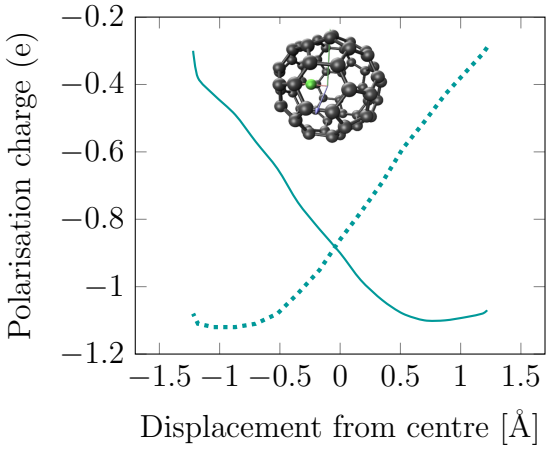

Figure 4.8: Polarisation charge located on the left-hand (dotted line) and right-hand (smooth line) hemispheres of the fullerene cage in $Ca@C_{60}$ as a function of the position of the calcium ion.

centre, the polarisation charge reduces to -0.86e, with net charge transfer being $Ca^{1.79+}@C_{60}^{1.79-}$. As the calcium moves into the functionalised (RHS) hemisphere to the energy minimum at 1.18Å from the cage centre, the polarisation charge reduces further to -0.31e with net charge transfer being $Ca^{1.50+}@C_{60}^{1.50-}$. Therefore, as the calcium moves between the two energy minima, the charge switches by approximately 0.80e. This behaviour clearly demonstrates the established correlation between surface charge polarisation and calcium ion motion for the $Ca@C_{60}$ system.

Ground state electronic properties were also calculated to give a holistic view of $Ca@C_{60}$:

Molecule	**Multiplicity**	**Energy (eV)**	**Singlet – Triplet gap (eV)**
$Ca@C_{60}$	Singlet	-80,671	-0.05

Table 4.9: Calculated ground state electronic properties for $Ca@C_{60}$.

An unexpected result was the calculated singlet ground state. The singlet ground state was also predicted at all levels of theory tested, with an average singlet-triplet gap of 0.05 eV. As discussed previously, the literature

provides good evidence for the triplet $^3A_2$ (e_1^2) ground state, however, Wang et al. noted three potential electronic states for the C_{5v} symmetry arising from the off-centre calcium ion; $^3A_2$ (e_1^2), $^1A_1$ (a_1^2) and $^3A_1$ (a_1a_1). The energy separation between the $^3A_2$ (e_1^2) and $^1A_1$ (a_1^2) states (essentially the singlet-triplet gap) was calculated to be 0.12 eV. The 0.05 eV singlet-triplet gap calculated is relatively small and therefore suggests that whilst the singlet electronic state is the predicted ground-state, a triplet ground state is energetically close and therefore one can see how previous calculations could have derived this result, as shown in the literature. The impact of this relates to magnetic and conductance behaviour. A singlet state molecule (all electrons paired) is diamagnetic (repelled by a magnetic field) with limited conductivity – which are the properties of C_{60}. Conversely, a triplet state molecule (unpaired electrons) is paramagnetic and potentially a conductor of electricity. These results reinforce the view that $Ca@C_{60}$ is diamagnetic in character with limited conductivity, however, the very small singlet-triplet gap suggests that it would require a small amount of energy to prepare a triplet state $Ca@C_{60}$ system that would be paramagnetic and potentially conducting. In 2013, Filidou et al. [135] presented electron paramagnetic resonance spectroscopy and electron nuclear double resonance studies on a functionalised exohedral fullerene system, dimethyl[9-hydro (C60-Ih)[5,6]fulleren-1(9H)-yl]phosphonate (DMHFP), where the triplet electron spin was used to hyperpolarise, couple and measure two nuclear spins [135]. This paper first discussed the triplet state system for C_{60}, created through photoexcitation of the singlet ground state to a singlet excited state followed by the process of inter-system crossing (ISC), originating from the spin-orbit coupling. The ISC process populates the lowest triplet state unevenly, which then decays to the singlet ground state directly. These studies and the small singlet-triplet gap observed in this research's calculations suggest that an ISC process might be possible for $Ca@C_{60}$. However,

this is outside the scope of this research and so will be left to future studies.

Chapter 5

Polarisation properties of hydrogenated and fluorinated metallofullerenes

Following the selection of candidate functionalised fullerenes and relevant DFT parameters, DFT calculations were undertaken to predict their ground state geometries and partial charge distributions. To understand the impact of functionalisation on internal potential energy barriers, single point energies and partial charges were calculated for calcium positions across the cage, towards the centres of the functionalised sites. The surface polarisation charge on each hemisphere was then calculated to observe the polarisation switching process as a function of calcium motion. Molecular stabilities were assessed through formation energy calculations, followed by a comparison of the hydrogenated and fluorinated molecules, informing final candidate choices for a bi-stable polarisation switch. The discussion is then extended to consider how such a switch could be scaled up through stabilised nanoparticle lattices comprising endohedral fullerenes [46].

5.1 Hydrogenated $Ca@C_{60}$

Please note that a tabulated summary of all DFT calculated polarisation properties presented in this section can be found at appendix A.

5.1.1 1,2-$Ca@C_{60}H_2$

DFT geometry optimisation calculations on both singlet and triplet states of 1,2-$Ca@C_{60}H_2$ predict the ground state to be an optimised singlet state with the calcium located 1.14 Å from the centre of the non-functionalised hemisphere, aligned with the midpoint of the 6-6 hexagon's adjacent to the functionalised site, as shown in the left-hand illustration of Figure 5.1. The right-hand illustration shows the off-centre position of the calcium and direction of the dipole, pointing directly away from the functionalised site, indicating an accumulation of surface charge in the opposite hemisphere. The functionalised site shows a slight cage deformation as a result of the newly created sp^3 bonds at the addition site.

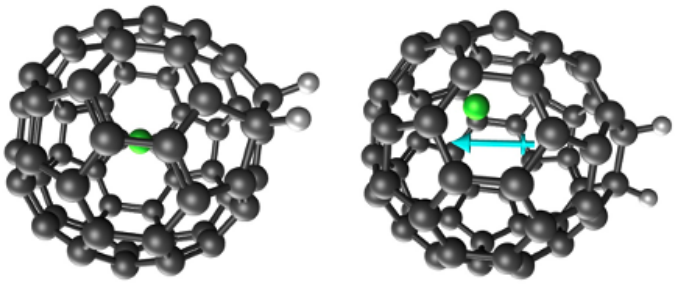

Figure 5.1: The left-hand illustration shows the ground state geometry of 1,2-$Ca@C_{60}H_2$ with calcium aligned to the midpoint of the 6-6 bond. The RHS illustration shows the same molecule, rotated to visualise the calcium off-centre position, the functionalised site and the resulting dipole (blue arrow).

A translational analysis of DFT single point energies and partial charges is shown in figure 5.2.

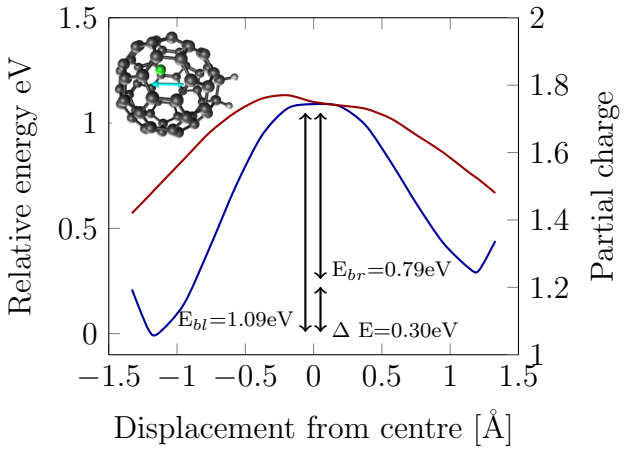

Figure 5.2: 1,2-Ca@$C_{60}H_2$ relative potential energy (blue) as the calcium is displaced towards (RHS) and away from (LHS) the H_2 functionalised site, and corresponding DDEC6 partial charge profile (red) of the calcium ion. E_{bl} and E_{br} are the energy barriers for the left and right hemispheres respectively, and ΔE is the energy gap between minima.

The addition of H_2 results in the Mexican-hat potential becoming asymmetrical with an energy gap of 0.30 eV between minima, with the global minimum located in the non-functionalised hemisphere. The predicted calcium partial charge at this location is +1.50e, indicating a charge transfer of +0.50e from the cage to the calcium when comparing to the isolated Ca^{2+} ion. The maximum energy barrier, 1.09 eV, remains in the centre of the molecule (as with Ca@C_{60}). The partial charge profile becomes asymmetrical, with the maximum (+1.77e) shifting into the non-functionalised hemisphere. The asymmetrical distribution of surface charge can clearly be seen in figure 5.3.

When the calcium is at the lowest energy minima position in the non-functionalised hemisphere, an accumulation of charge is clearly observed in this hemisphere. As the calcium moves to the centre of the cage, the surface charge distributes more evenly throughout the cage. When the calcium moves into the functionalised hemisphere, to the higher energy minima position, the surface charge follows the calcium ion, also shifting into the functionalised hemisphere towards the functionalised sites. To

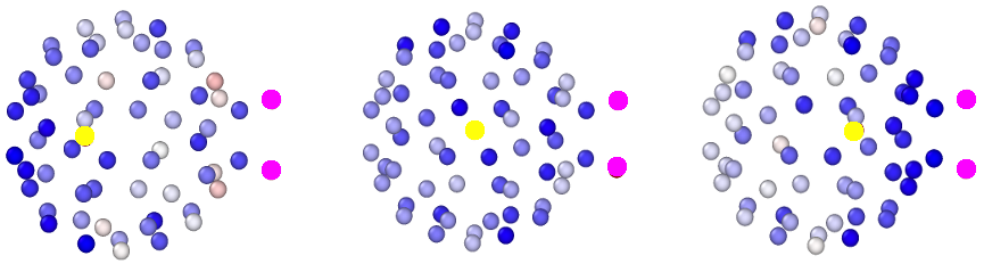

Figure 5.3: Distribution of partial atomic charge for three different positions of the calcium atom (yellow particle inside cage) in 1,2-Ca@$C_{60}H_2$. The lower energy minima (LHS), calcium at the centre (middle), and the higher energy minima (RHS). The carbon atoms are depicted according to the charge they carry: red (positive) and blue (negative). The hydrogens are the purple circles outside the cage.

understand this motion further, the surface polarisation charge on each hemisphere was plotted as a function of the position of the calcium ion:

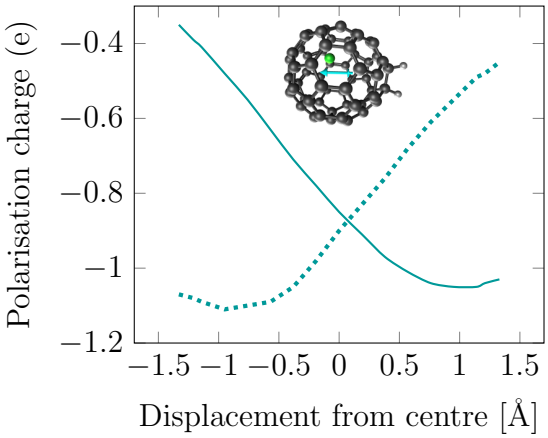

Figure 5.4: Polarisation charge located on the left hemisphere (dotted line) and right hemisphere (smooth line) of the fullerene cage in 1,2-Ca@$C_{60}H_2$ as a function of the position of the calcium ion. The results of the right hemisphere include contributions from the two hydrogens.

Similar to Ca@C_{60}, the polarisation charge in each hemisphere is negative for all radial positions of calcium. Focusing on the left-hemisphere (dotted line), at the lowest energy minimum, where the calcium is displaced -1.14Å from the cage centre, the polarisation charge is -1.09e with net charge transfer being 1,2-$Ca^{1.50+}@C_{60}^{1.50-}H_2$. As the calcium moves to the energy maximum at the cage centre the polarisation charge reduces to -0.90e with net charge transfer being 1,2-$Ca^{1.76+}@C_{60}^{1.76-}H_2$, slightly less than Ca@$C_{60}$.

As the calcium moves into the functionalised (RHS) hemisphere to the energy minimum at 1.14Å from the cage centre, the polarisation charge reduces further to -0.48e with net charge transfer being 1,2-$Ca^{1.50+}@C_{60}^{1.50-}H_2$. Therefore, as the calcium moves between the two energy minima, the charge switches by approximately 0.61e.

Interestingly, there is a mismatch between the position of lowest energy minimum and lowest surface charge polarisation in the left hemisphere, also observed in Raggi et al.'s analysis of the isomers of $Ca@C_{60}H_4$ [35]. This asymmetrical distribution of surface charge as the calcium moves across the molecule clearly demonstrates both the modification of internal energy barriers and the correlation between surface charge polarisation and calcium ion motion for the 1,2-$Ca@C_{60}H_2$ system.

5.1.2 1,2,3,4-Ca@$C_{60}H_4$

DFT geometry optimisation calculations on both singlet and triplet states of 1,2,3,4-Ca@$C_{60}H_4$ predict the ground state to be an optimised singlet state with the calcium located 1.13 Å from the centre of the non-functionalised hemisphere, aligned with the pentagon centre, as shown in the left-hand illustration of figure 5.5. The right-hand illustration shows the off-centre position of the calcium and direction of the dipole, pointing directly away from the functionalised site, indicating an accumulation of surface charge in the opposite hemisphere. The functionalised site shows a more pronounced cage deformation compared to 1,2-Ca@$C_{60}H_2$ as a result of the newly created sp^3 bonds at the addition site.

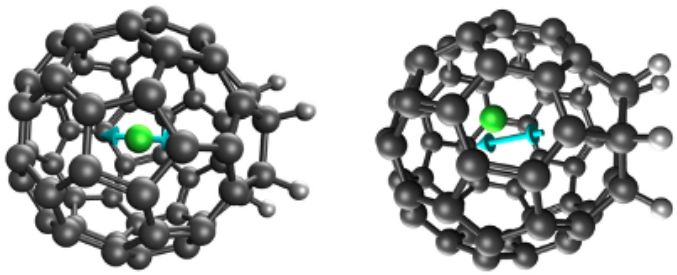

Figure 5.5: The left-hand illustration shows the ground state geometry of 1,2,3,4-Ca@$C_{60}H_4$ with calcium aligned to the midpoint of the pentagon centre. The RHS illustration shows the same molecule, rotated to visualise the calcium off-centre position, the functionalised site and the resulting dipole (blue arrow).

A translational analysis of DFT single point energies and partial charges can be seen in figure 5.6 showing the impact of functionalisation on the internal potential energy profile and energy barriers between the two minima in each hemisphere.

The addition of H_4 results in the Mexican-hat potential becoming asymmetrical with an energy gap of 0.35 eV between minima, with the global minimum located in the non-functionalised hemisphere. The predicted calcium partial charge at this location is +1.54e, indicating a charge transfer

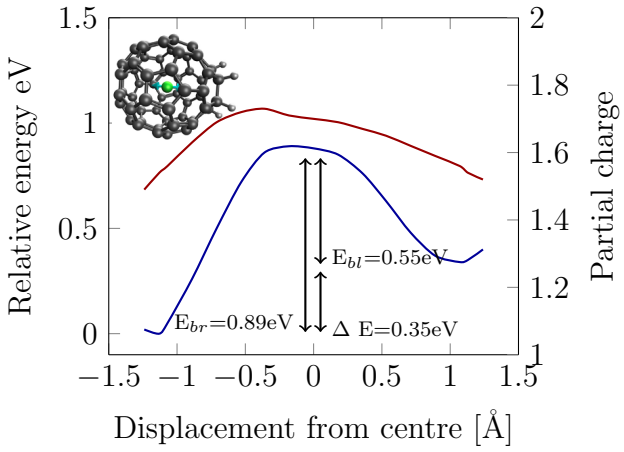

Figure 5.6: 1,2,3,4-Ca@$C_{60}H_4$ relative potential energy (blue) as the calcium is displaced towards (RHS) and away from (LHS) the H_4 functionalised site, and corresponding DDEC6 partial charge profile (red) of the calcium ion at the B3P86-D3 / cc-pVDZ level of theory

of +0.46e from the cage to the calcium when comparing to the isolated Ca^{2+} ion. The maximum energy barrier, 0.89 eV, is marginally shifted off-centre by 0.09 Å into the non-functionalised hemisphere, with minima also shifted in the same direction. The partial charge profile is again asymmetrical, with the maximum (+1.73e) shifting into the non-functionalised hemisphere. The asymmetrical distribution of surface charge can clearly be seen in Figure 5.7.

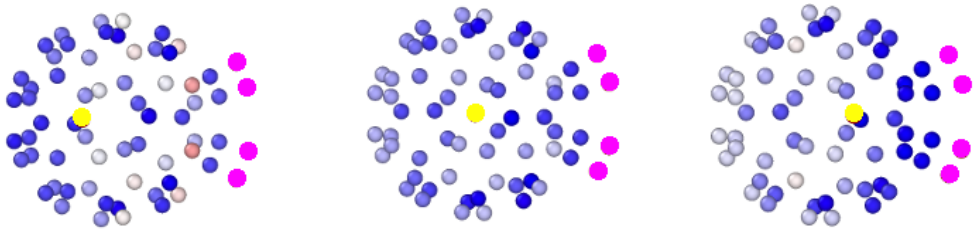

Figure 5.7: Distribution of partial atomic charge for three different positions of the calcium atom (yellow particle inside cage) in 1,2,3,4-Ca@$C_{60}H_4$. The lower energy minima (LHS), calcium at the centre (middle), and the higher energy minima (RHS). The carbon atoms are depicted according to the charge they carry: red (positive) and blue (negative). The hydrogens are the purple circles outside the cage.

When the calcium is at the lowest energy minima position in the non-functionalised hemisphere, an accumulation of charge is clearly observed in

this hemisphere. As the calcium moves to the centre of the cage, the surface charge distributes more evenly throughout the cage, albeit in this case, with a slight increase in surface charge into the functionalised hemisphere, emphasising the effect observed in 1,2-Ca@$C_{60}H_2$. When the calcium moves into the functionalised hemisphere, to the higher energy minimum position, the surface charge follows the calcium ion, also shifting into the functionalised hemisphere towards the functionalised sites. To understand this motion further, the surface polarisation charge on each hemisphere was plotted as a function of the position of the calcium ion:

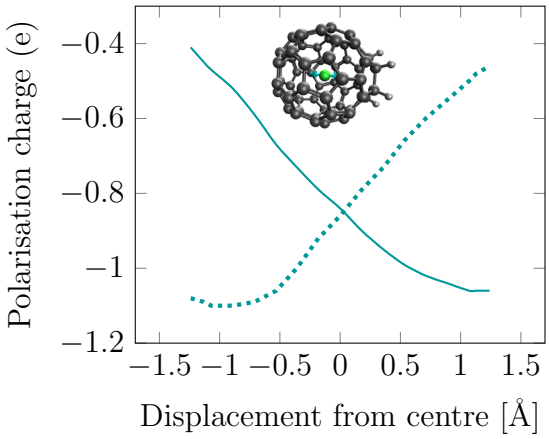

Figure 5.8: Polarisation charge located on the left hemisphere (dotted line) and right hemisphere (smooth line) of the fullerene cage in 1,2,3,4-Ca@$C_{60}H_4$ as a function of the position of the calcium ion. The results of the right hemisphere include contributions from the four hydrogens.

Similar to 1,2-Ca@$C_{60}H_2$, the polarisation charge in each hemisphere is negative for all radial positions of calcium. Focusing on the left-hemisphere (dotted line), at the lowest energy minimum, where the calcium is displaced -1.13Å from the cage centre, the polarisation charge is -1.09e with net charge transfer being 1,2,3,4-$Ca^{1.54+}@C_{60}^{1.54-}H_4$. As the calcium moves to the energy maximum at the cage centre the polarisation charge increases to -0.85e with net charge transfer being 1,2,3,4-$Ca^{1.71+}@C_{60}^{1.71-}H_4$. As the calcium moves into the functionalised (RHS) hemisphere to the energy minimum at 1.07Å from the cage centre, the polarisation charge reduces to

-0.48e with net charge transfer being 1,2,3,4-$Ca^{1.54+}@C_{60}^{1.54-}H_4$. Therefore, as the calcium moves between the two energy minima, the charge switches by approximately 0.61e.

Again, the position of maximum surface charge polarisation does not coincide with the lowest energy minima position, but at a distance -0.8Å from the centre. However, this is not the case for the functionalised hemisphere, where the maximum degree of surface charge polarisation more closely corresponds with the energy minima position. This effect was also observed by Raggi et al. [35] when investigating 1,2,3,4-$Ca@C_{60}H_4$ and points again to the "pushing effect" the hydrogens have on the internal energy profile of the system. Given the barriers are constructed as a result of the system's electrostatics, this could be due to the positively charged hydrogen atoms interacting with the accumulated charge on the cage surface. This asymmetrical distribution of surface charge as the calcium moves across the molecule again reinforces the findings of Raggi et al. and clearly demonstrates both the modification of internal energy barriers and the correlation between surface charge polarisation and calcium ion motion for the 1,2,3,4-$Ca@C_{60}H_4$ system.

These results provide a useful comparison to Raggi et al.'s work on $Ca@C_{60}H_4$ isomers [35], particularly "isomer f" described in the paper which is very similar to the 1,2,3,4-$Ca@C_{60}H_4$ isomer used in this study, with the main difference being that this study's second hydrogen addition occurs at the adjacent 6-6 bond next to the 1,2 site as described by Henderson et al. [109]. Note also that Raggi et al.'s "isomer f" was calculated at the B3LYP / 6-31G* level of theory, finding the ground state to be of a triplet multiplicity, compared to the singlet multiplicity identified in this work at the B3P86-D3 / cc-pVDZ level of theory. Interestingly, the other isomers tested in the aforementioned paper all possessed a singlet multiplicity.

The ground state positions of the energy minima (the calcium's optimised position) were relatively similar across both results. Raggi et al.'s calculated energy gap, ΔE, was 0.2eV, compared to this study's energy gap of 0.35eV. The change in polarisation charge is identical, being a 0.6e change from the left hemisphere to the right hemisphere as the calcium moves across the cage. The marginal differences may be due to the slight difference of isomer configuration used in this study. What is clear from this analysis and Raggi et al.'s work is the impact of different locations of hydrogen addition on both the internal energy profile and polarisation charge as the calcium moved across the cage. This highlights that isomer purity is a crucial part of the validation process to determine candidates for a polarisation switch. A mix of isomers could lead to ineffective and unpredictable switching behaviour.

5.1.3 S-Ca@$C_{60}H_6$

DFT geometry optimisation calculations on both singlet and triplet states of S-Ca@$C_{60}H_6$ predict the ground state to be an optimised singlet state with the calcium located 1.15 Å from the centre of the non-functionalised hemisphere, aligned off-centre to one of the 6–6 hexagons, as shown in the left-hand illustration of figure 5.9. The right-hand illustration shows the off-centre position of the calcium and direction of the dipole, pointing directly away from the functionalised site indicating an accumulation of surface charge in the opposite hemisphere. The functionalised site shows a more pronounced cage deformation compared to 1,2,3,4-Ca@$C_{60}H_4$ as a result of the newly created sp^3 bonds at the addition site.

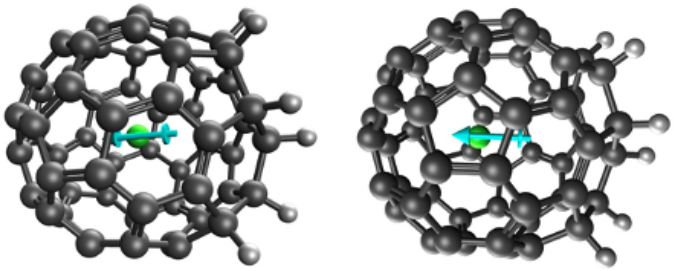

Figure 5.9: The left-hand illustration shows the ground state geometry of S-Ca@$C_{60}H_6$ with calcium aligned to the midpoint of the pentagon centre. The RHS illustration shows the same molecule, rotated to visualise the calcium off-centre position, the functionalised site and the resulting dipole (blue arrow).

A translational analysis of DFT single point energies and partial charges can be seen in figure 5.10 showing the impact of functionalisation on the internal potential energy profile and energy barriers between the two minima in each hemisphere.

The addition of H_6 results in the Mexican-hat potential becoming asymmetrical with an energy gap of 0.51 eV between minima, with the global minimum located in the non-functionalised hemisphere. The predicted calcium partial charge at this location is +1.50e, indicating a charge transfer

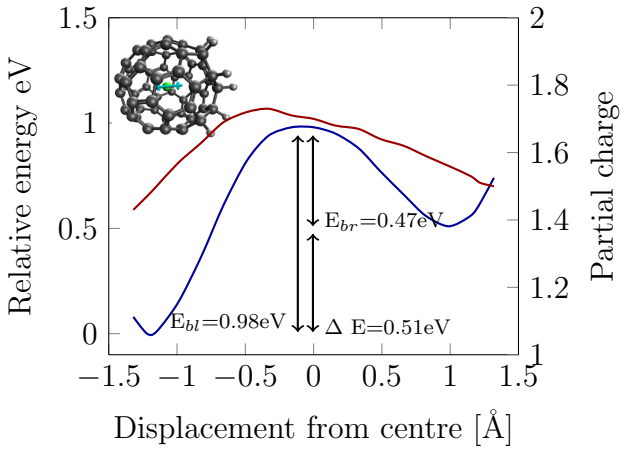

Figure 5.10: S-Ca@$C_{60}H_6$ relative potential energy (blue) as the calcium is displaced towards (RHS) and away from (LHS) the H_6 functionalised site, and corresponding DDEC6 partial charge profile (red) of the calcium ion at the B3P86-D3 / cc-pVDZ level of theory

of +0.50e from the cage to the calcium when comparing to the isolated Ca^{2+} ion. The maximum energy barrier, 0.98 eV, is marginally shifted off-centre by 0.09 Å into the non-functionalised hemisphere, with minima also shifted in the same direction. The partial charge profile is again asymmetrical, with the maximum (+1.73e) shifting into the non-functionalised hemisphere.

The asymmetrical distribution of surface charge can clearly be seen in Figure 5.11.

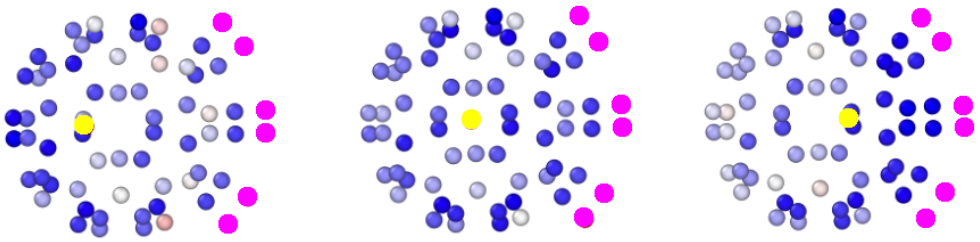

Figure 5.11: Distribution of partial atomic charge for three different positions of the calcium atom (yellow particle inside cage) in S-Ca@$C_{60}H_6$. The lower energy minima (LHS), calcium at the centre (middle), and the higher energy minima (RHS). The carbon atoms are depicted according to the charge they carry: red (positive) and blue (negative). The hydrogens are the purple circles outside the cage.

When the calcium is at the lowest energy minima position in the non-

functionalised hemisphere, an accumulation of charge is clearly observed in this hemisphere. As the calcium moves to the centre of the cage, the surface charge distributes more evenly throughout the cage, with a slight increase in surface charge into the functionalised hemisphere, emphasising the effect observed in 1,2-Ca@$C_{60}H_2$ and 1,2,3,4-Ca@$C_{60}H_4$. When the calcium moves into the functionalised hemisphere, to the higher energy minima position, the surface charge follows the calcium ion, also shifting into the functionalised hemisphere towards the functionalised sites. To understand this motion further, the surface polarisation charge on each hemisphere was plotted as a function of the position of the calcium ion:

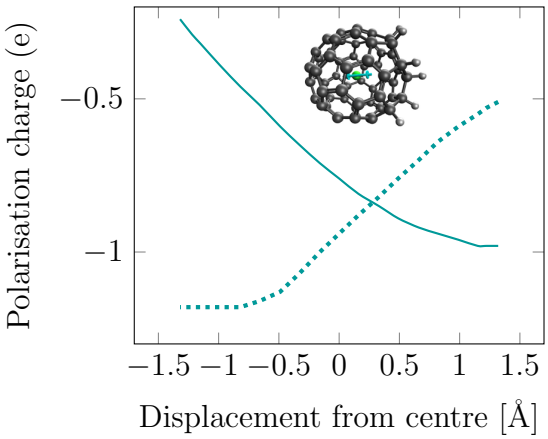

Figure 5.12: Polarisation charge located on the left hemisphere (dotted line) and right hemisphere (smooth line) of the fullerene cage in S-Ca@$C_{60}H_6$ as a function of the position of the calcium ion. The results of the right hemisphere include contributions from the six hydrogens.

Similar to 1,2-Ca@$C_{60}H_2$ and 1,2,3,4-Ca@$C_{60}H_4$, the polarisation charge in each hemisphere is negative for all radial positions of calcium. Focusing on the left-hemisphere (dotted line), at the lowest energy minimum (left-hemisphere), where the calcium is displaced -1.15Å from the cage centre, the polarisation charge is -1.18e with net charge transfer being S-$Ca^{1.50+}$@$C_{60}^{1.50-}H_6$. As the calcium moves to the energy maximum at the cage centre, the polarisation charge increases to -1.07e, with net charge transfer being S-$Ca^{1.73+}$@$C_{60}^{1.73-}H_6$. As the calcium moves into the function-

alised (RHS) hemisphere to the energy minimum at 0.99Å from the cage centre, the polarisation charge reduces to -0.59e with net charge transfer being S-$Ca^{1.56+}@C_{60}^{1.56-}H_6$. Therefore, as the calcium moves between the two energy minima, the charge switches by 0.59e. The position of maximum surface charge polarisation does not coincide with the lowest energy minima position, but at a distance -0.1Å from the centre, demonstrating again the "pushing effect" the hydrogens have on the internal energy profile of the system. The asymmetrical distribution of surface charge again demonstrates the modification of internal energy barriers and the correlation between surface charge polarisation and calcium motion.

These results also provide a useful comparison to Raggi et al.'s work on $Ca@C_{60}H_6$ [17], particularly figure 3 in the paper showing the energy barriers of an isomer of $Ca@C_{60}H_6$ where each hydrogen is added to one full hexagon, 1,2,3,4,5,6-$Ca@C_{60}H_6$. In this configuration, ΔE was calculated to be 0.23 eV with a maximum energy barrier of 0.93 eV. This is compared to this study's S-$Ca@C_{60}H_6$ isomer where the energy gap was predicted to be 0.51 eV with a maximum energy barrier of 0.98 eV. Interestingly, the maximum energy barriers closely correspond to each other, however, the almost two-fold difference of the calculated energy gap again demonstrates the importance of isomer selection. Raggi et al.'s isomer concentrates addition on one hexagon and the smaller energy gap is comparable to that of 1,2-$Ca@C_{60}H_2$ and 1,2,3,4-$Ca@C_{60}H_4$ predicted in this study. The impact of the S-motif addition for S-$Ca@C_{60}H_6$ spreads out sp^3 hybrid carbons and increases the energy gap between minima.

5.1.4 T-Ca@$C_{60}H_8$

DFT geometry optimisation calculations on both singlet and triplet states of T-Ca@$C_{60}H_8$ predict the ground state to be an optimised singlet state with the calcium located 1.30 Å from the centre of the non-functionalised hemisphere, aligned off-centre to one of the 6–6 hexagons adjacent to the functionalised site, as shown in the left-hand illustration of figure 5.13. The right-hand illustration shows the off-centre position of the calcium and direction of the dipole, pointing directly away from the functionalised site, indicating an accumulation of surface charge in the opposite hemisphere. The functionalised site shows a slight cage deformation as a result of the newly created sp^3 bonds at the addition site.

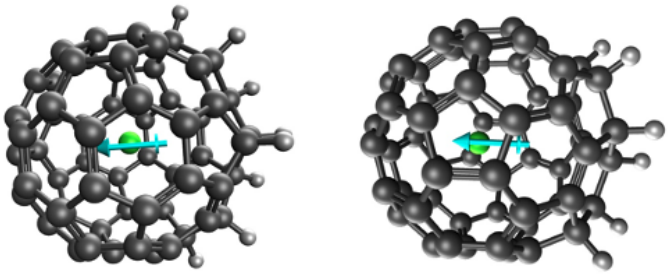

Figure 5.13: The left-hand illustration shows the ground state geometry of T-Ca@$C_{60}H_8$ with calcium aligned to the midpoint of the 6-6 bond. The RHS illustration shows the same molecule, rotated to visualise the calcium off-centre position, the functionalised site and the resulting dipole (blue arrow).

The translational analysis of DFT single point energies and partial charges can be seen in figure 5.14 showing the impact of functionalisation on the internal potential energy profile and energy barriers between the two minima in each hemisphere.

The addition of H_8 results in the Mexican-hat potential becoming asymmetrical with an energy gap of 0.44 eV between minima, with the global minimum located in the non-functionalised hemisphere. The predicted calcium partial charge at this location is +1.47e, indicating a charge transfer

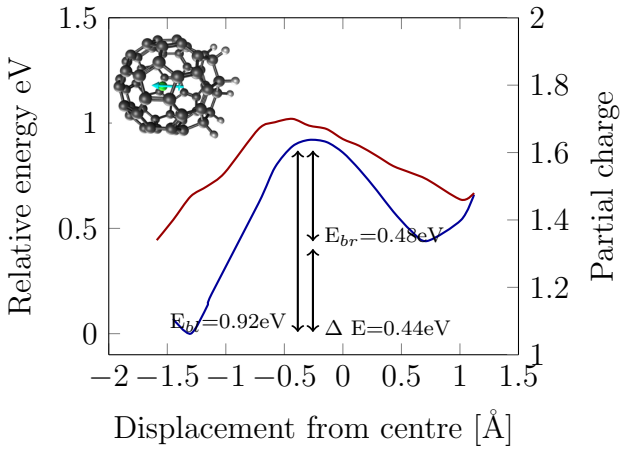

Figure 5.14: T-Ca@$C_{60}H_8$ relative potential energy (blue) as the calcium is displaced towards (LHS) and away from (RHS) the H_8 functionalised site, and corresponding DDEC6 partial charge profile (red) of the calcium ion at the B3P86-D3 / cc-pVDZ level of theory

of +0.53e from the cage to the calcium when comparing to the isolated Ca^{2+} ion. The maximum energy barrier, 0.92 eV, is shifted off-centre by 0.29 Å into the non-functionalised hemisphere, with minima also shifted in the same direction. The partial charge profile is again asymmetrical, with the maximum (+1.70e) shifting into the non-functionalised hemisphere. The asymmetrical distribution of surface charge can clearly be seen in the Figure 5.15.

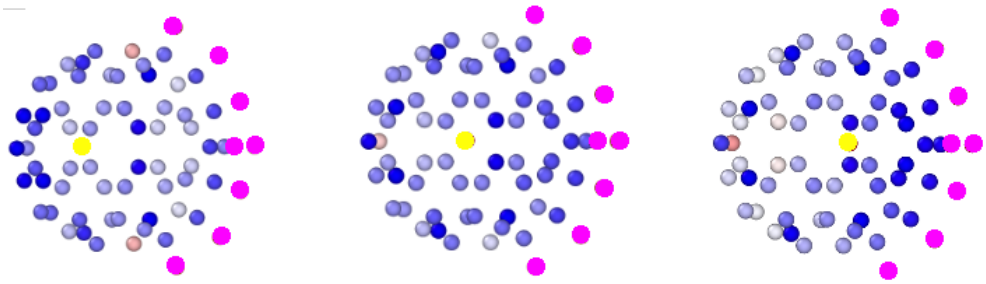

Figure 5.15: Distribution of partial atomic charge for three different positions of the calcium atom (yellow particle inside cage) in T-Ca@$C_{60}H_8$. The lower energy minima (LHS), calcium at the centre (middle), and the higher energy minima (RHS). The carbon atoms are depicted according to the charge they carry: red (positive) and blue (negative). The hydrogens are the purple circles outside the cage.

When the calcium is at the lowest energy minima position in the non-

functionalised hemisphere, an accumulation of charge is clearly observed in the left hemisphere. As the calcium moves to the centre of the cage, the surface charge distributes more evenly throughout the cage. When the calcium moves into the functionalised hemisphere, to the higher energy minimum position, the surface charge follows the calcium ion, also shifting into the functionalised hemisphere towards the functionalised sites. To understand this motion further the surface polarisation charge on each hemisphere was plotted as a function of the position of the calcium ion:

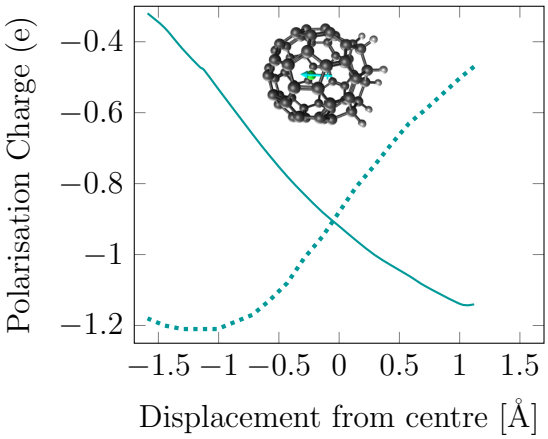

Figure 5.16: Polarisation charge located on the left hemisphere (dotted line) and right hemisphere (smooth line) of the fullerene cage in T-Ca@$C_{60}H_8$ as a function of the position of the calcium ion. The results of the right hemisphere include contributions from the eight hydrogens.

Similar to all preceding hydrogenated Ca@C_{60} molecules, the polarisation charge in each hemisphere is negative for all radial positions of calcium. Focusing on the left-hemisphere (dotted line), at the lowest energy minimum (left-hemisphere), where the calcium is displaced -1.30Å from the cage centre, the polarisation charge is -1.21e with net charge transfer being T-$Ca^{1.47+}@C_{60}^{1.47-}H_8$. As the calcium moves to the energy maximum at the cage centre, the polarisation charge increases to -1.08e, with net charge transfer being T-$Ca^{1.70+}@C_{60}^{1.70-}H_8$. As the calcium moves into the functionalised (RHS) hemisphere to the energy minimum at 0.72Å from the cage centre, the polarisation charge reduces to -0.59e with net charge

transfer being T-$Ca^{1.52+}@C_{60}^{1.52-}H_8$. Therefore, as the calcium moves between the two energy minima, the charge switches by approximately 0.62e. The position of maximum surface charge polarisation does not coincide with the lowest energy minima position, but at a distance -1.0Å from the centre, demonstrating again the "pushing effect" the hydrogens have on the internal energy profile of the system. The asymmetrical distribution of surface charge again demonstrates the modification of internal energy barriers and the correlation between surface charge polarisation and calcium motion.

5.1.5 Formation energy: Hydrogen functionalisation

The DFT calculations provide information on the energy required to break the sp^2 hybridised C=C bond and form two sp^3 hybridised C-H bonds. The first four hydrogen additions to $Ca@C_{60}$ (H_2, H_4, H_6 and H_8) reduce the ground state energy linearly by an average 33.19 eV. The energy to break the sp^2 hybridised C=C bond and form two sp^3 hybridised C-H bonds can be described by the following equations:

$$\begin{gathered} Ca@C_{60}H_n + H_2 \rightarrow Ca@C_{60}H_{n+2} \\ \Delta E_{H-H} = H_2 - 2H \\ \Delta E_{2C-H} = Ca@C_{60}H_{n+2} - Ca@C_{60}H_n - H_2 \end{gathered} \tag{5.1}$$

A DFT calculation was performed to determine the ground state energy of H_2 at the B3P86 / cc-pVDZ level of theory, yielding an energy of -32.26 eV. Therefore, the energy to break the sp^2 hybridised C=C bond and form two sp^3 hybridised C-H bonds is:

$$\Delta E_{2C-H} = -33.19 \text{ eV} - (-32.26 \text{ eV}) = -0.93 \text{ eV} \tag{5.2}$$

The net energy lost by the system when forming each sp^3 hybridised C-H bond from the sp^2 hybridised C=C is -0.47 eV indicates an energetically favourable process.

5.2 Fluorinated $Ca@C_{60}$

Please note that a tabulated summary of all DFT calculated polarisation properties presented in this section can be found at appendix A.

5.2.1 1,2-$Ca@C_{60}F_2$

DFT geometry optimisation calculations on both singlet and triplet states of 1,2-$Ca@C_{60}F_2$ predict the ground state to be an optimised singlet state with the calcium located -1.32 Å from the centre of the non-functionalised hemisphere, aligned to the midpoint of the 6-6 hexagon adjacent to the functionalised site, as shown in the left-hand illustration of Figure 5.17. The right-hand illustration shows the off-centre position of the calcium and direction of the dipole, pointing directly towards from the functionalised site. Compared to this molecule's hydrogen counterpart, the dipole points in the opposite direction towards the strongly negative fluorine atoms rather than towards the weaker accumulated negative charge in the left hemisphere as a result of the calcium position. The functionalised site shows a slight cage deformation as a result of the newly created sp^3 bonds at the addition site.

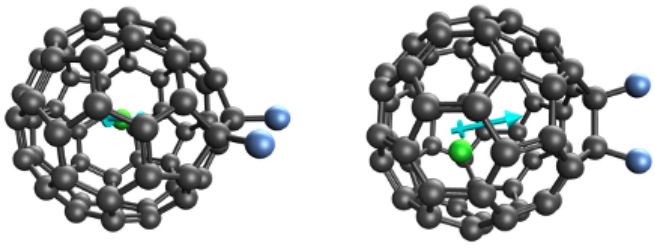

Figure 5.17: The left-hand illustration shows the ground state geometry of 1,2-$Ca@C_{60}F_2$ with calcium aligned to the midpoint of the 6-6 bond. The RHS illustration shows the same molecule, rotated to visualise the calcium off-centre position, the functionalised site and the resulting dipole (blue arrow).

A translational analysis of DFT single point energies and partial charges

can be seen in figure 5.18 showing the impact of functionalisation on the internal potential energy profile and energy barriers between the two minima in each hemisphere.

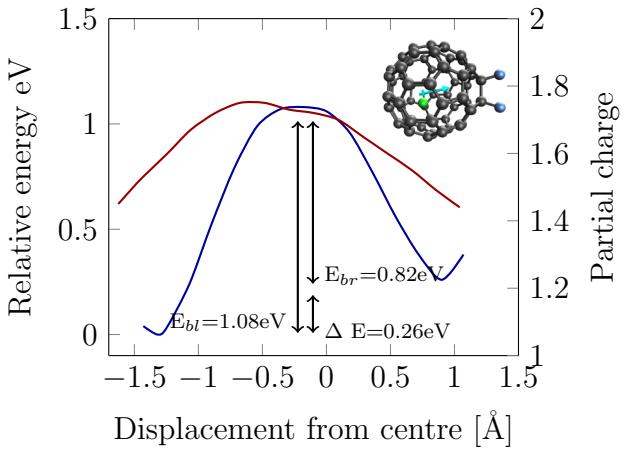

Figure 5.18: 1,2-Ca@$C_{60}F_2$ relative potential energy (blue) as the calcium is displaced towards (LHS) and away from (RHS) the F_2 functionalised site, and corresponding DDEC6 partial charge profile (red) of the calcium ion at the B3P86-D3 / cc-pVDZ level of theory

The addition of F_2 results in the Mexican-hat potential becoming asymmetrical with an energy gap of 0.26 eV between minima, with the global minimum located in the non-functionalised hemisphere. The predicted calcium partial charge at this location is +1.50e, indicating a charge transfer of +0.50e from the cage to the calcium when comparing to the isolated Ca^{2+} ion. The maximum energy barrier, 1.08 eV, is shifted -0.18 Å into the left hemisphere. The partial charge profile becomes asymmetrical, with the maximum (+1.73e) also shifting into the non-functionalised hemisphere. The asymmetrical distribution of surface charge can clearly be seen in figure 5.19.

One of the main initial differences when comparing against 1,2-Ca@$C_{60}H_2$ is that the strongly electronegative fluorine atoms result in the sp^3 carbons being positively charged (0.22e each). Interestingly, the total charge on the C-F and C-H units are the same, 0.05 e. This demonstrates that the

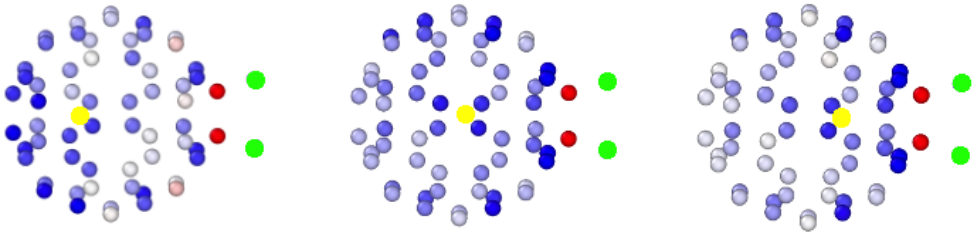

Figure 5.19: Distribution of partial atomic charge for three different positions of the calcium atom (yellow particle inside cage) in 1,2-Ca@$C_{60}F_2$. The lower energy minima (LHS), calcium at the centre (middle), and the higher energy minima (RHS). The carbon atoms are depicted according to the charge they carry: red (positive) and blue (negative). The fluorines are the green circles outside the cage.

available total charge to distribute on each new sp^3 site does not change as a result of functionalisation, more that the charge is distributed towards the most electronegative species in the unit. For C-F this is fluorine and for C-H this is carbon (although the difference in electronegativity is typically small between carbon and hydrogen, resulting in a non-polar bond).

When the calcium is at the lowest energy minimum position in the non-functionalised hemisphere, an accumulation of charge is clearly observed in this hemisphere. As the calcium moves to the centre of the cage, the surface charge distributes more evenly throughout the cage. When the calcium moves into the functionalised hemisphere, to the higher energy minima position, the surface charge follows the calcium ion, also shifting into the functionalised hemisphere towards the functionalised sites. To understand this motion further, the surface polarisation charge on each hemisphere was plotted as a function of the position of the calcium ion in figure 5.20.

The polarisation charge in each hemisphere is negative for all radial positions of calcium. Focusing on the left-hemisphere (dotted line), at the lowest energy minimum, where the calcium is displaced -1.32Å from the cage centre, the polarisation charge is -0.88e with net charge transfer be-

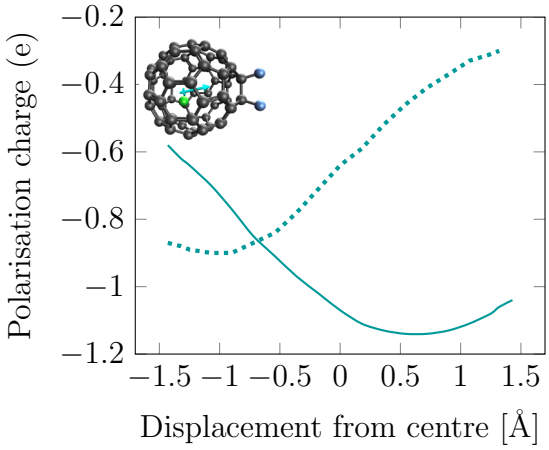

Figure 5.20: Polarisation charge located on the left hemisphere (dotted line) and right hemisphere (smooth line) of the fullerene cage in 1,2-Ca@$C_{60}F_2$ as a function of the position of the calcium ion. The results of the right hemisphere include contributions from the two fluorines.

ing 1,2-$Ca^{1.50+}@C_{60}^{1.50-}F_2$. As the calcium moves to the energy maximum the polarisation charge reduces to -0.71e with net charge transfer being 1,2-$Ca^{1.73+}@C_{60}^{1.73-}F_2$. As the calcium moves into the functionalised (RHS) hemisphere to the energy minimum at 0.89Å from the cage centre, the polarisation charge reduces further to -0.37e with net charge transfer being 1,2-$Ca^{1.49+}@C_{60}^{1.49-}F_2$. Therefore, as the calcium moves between the two energy minima, the charge switches by approximately 0.51e, which is 0.1e less than the molecules' hydrogen counterpart, 1,2-Ca@$C_{60}H_2$. Similar to the hydrogenated series, there is again a mismatch between the position of lowest energy minimum and lowest surface charge polarisation. This asymmetrical distribution of surface charge as the calcium moves across the molecule clearly demonstrates both the modification of internal energy barriers and the correlation between surface charge polarisation and calcium ion motion for the 1,2-Ca@$C_{60}F_2$ system, albeit at a reduced intensity when compared to hydrogen.

5.2.2 1,2,3,4-Ca@$C_{60}F_4$

DFT geometry optimisation calculations on both singlet and triplet states of 1,2,3,4-Ca@$C_{60}F_4$ predict the ground state to be an optimised singlet state with the calcium located -1.61 Å from the centre of the non-functionalised hemisphere, aligned to the midpoint of the pentagon-hexagon join adjacent to the functionalised site, as shown in the left-hand illustration of figure 5.21. The right-hand illustration shows the off-centre position of the calcium and direction of the dipole, pointing directly towards the functionalised site, similar to that of 1,2-Ca@$C_{60}F_2$. The functionalised site shows a slight cage deformation as a result of the newly created sp^3 bonds at the addition site.

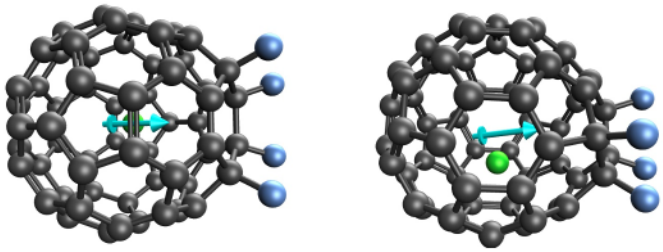

Figure 5.21: The left-hand illustration shows the ground state geometry of 1,2,3,4-Ca@$C_{60}F_4$ with calcium aligned to the midpoint of the pentagon-hexagon join. The RHS illustration shows the same molecule, rotated to visualise the calcium off-centre position, the functionalised site and the resulting dipole (blue arrow).

A translational analysis of DFT single point energies and partial charges can be seen in figure 5.22 showing the impact of functionalisation on the internal potential energy profile and energy barriers between the two minima in each hemisphere.

The addition of F_4 results in the Mexican-hat potential becoming asymmetrical with an energy gap of 0.27 eV between minima, with the global minimum located in the non-functionalised hemisphere. The predicted calcium partial charge at this location is +1.54e, indicating a charge transfer of

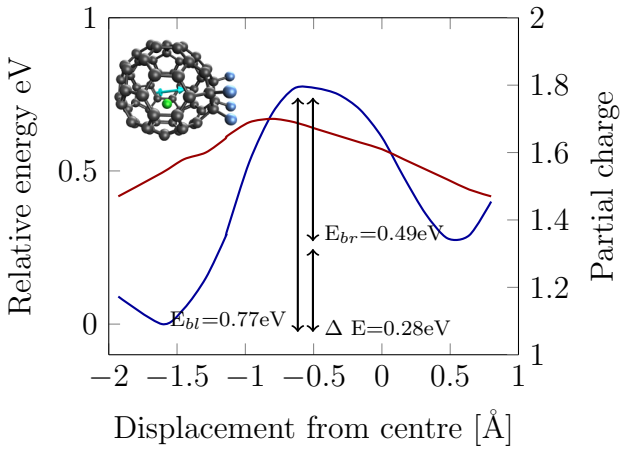

Figure 5.22: 1,2,3,4-Ca@$C_{60}F_4$ relative potential energy (blue) as the calcium is displaced towards (RHS) and away from (LHS) the F_4 functionalised site, and corresponding DDEC6 partial charge profile (red) of the calcium ion at the B3P86-D3 / cc-pVDZ level of theory

+0.46e from the cage to the calcium when comparing to the isolated Ca^{2+} ion. The maximum energy barrier, 0.77 eV, is shifted -0.56 Å into the left hemisphere. The partial charge profile becomes asymmetrical, with the maximum (+1.69e) also shifting into the non-functionalised hemisphere. The asymmetrical distribution of surface charge can clearly be seen in figure 5.23.

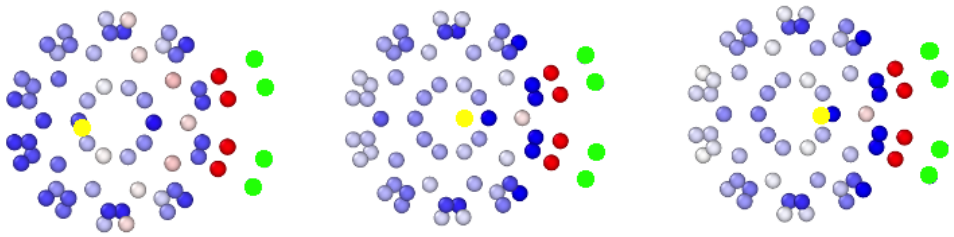

Figure 5.23: Distribution of partial atomic charge for three different positions of the calcium atom (yellow particle inside cage) in 1,2,3,4-Ca@$C_{60}F_4$. The lower energy minima (LHS), calcium at the centre (middle), and the higher energy minima (RHS). The carbon atoms are depicted according to the charge they carry: red (positive) and blue (negative). The fluorines are the green circles outside the cage.

Similarly to 1,2-Ca@$C_{60}F_2$ the strongly electronegative fluorine atoms result in the sp^3 carbons being positively charged. When the calcium is at the lowest energy minima position in the non-functionalised hemisphere,

an accumulation of charge is observed in this hemisphere. Interestingly, at this position, a ring of marginally positively charged carbons is observed on the cage next to the sp^3 carbons, indicating that the sp^3 carbons attract nearby surface charge. As the calcium moves to the centre of the cage, the surface charge distributes into the right-hand hemisphere, rather than evenly distributed compared to 1,2,3,4-Ca@$C_{60}H_4$. This is likely as a result of the positively charged sp^3 carbons attracting surface charge as the calcium moves towards the functionalised site. In fact, when the calcium moves into the functionalised hemisphere, to the higher energy minima position, the difference in surface charge distribution compared to the central position is negligible, as the higher energy minima is relatively close to the central position. To understand this motion further, the surface polarisation charge on each hemisphere was plotted as a function of the position of the calcium ion:

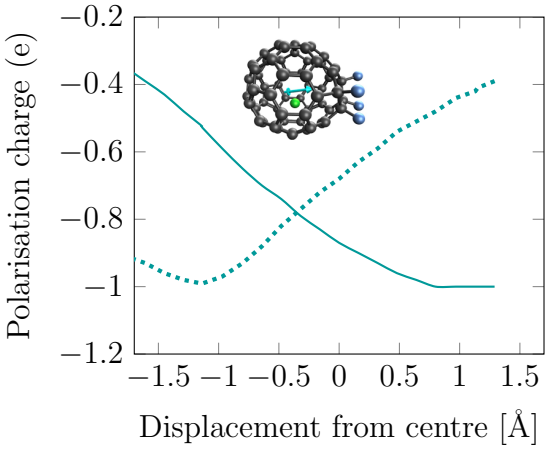

Figure 5.24: Polarisation charge located on the left hemisphere (dotted line) and right hemisphere (smooth line) of the fullerene cage in 1,2,3,4-Ca@$C_{60}F_4$ as a function of the position of the calcium ion. The results of the right hemisphere include contributions from the four fluorines.

The polarisation charge in each hemisphere is negative for all radial positions of calcium. Focusing on the left-hemisphere (dotted line), at the lowest energy minimum, where the calcium is displaced -1.61Å from the cage centre, the polarisation charge is -0.93e with net charge transfer being

1,2,3,4-$Ca^{1.47+}@C_{60}^{1.47-}F_4$. As the calcium moves to the energy maximum the polarisation charge reduces slightly to -0.88e with net charge transfer being 1,2,3,4-$Ca^{1.69+}@C_{60}^{1.69-}F_4$. As the calcium moves into the functionalised (RHS) hemisphere to the energy minimum at 0.48Å from the cage centre the polarisation charge reduces further to -0.54e with net charge transfer being 1,2,3,4-$Ca^{1.52+}@C_{60}^{1.52-}F_2$. Therefore, as the calcium moves between the two energy minima, the charge switches by approximately 0.39e. This asymmetrical distribution of surface charge as the calcium moves across the molecule clearly demonstrates both the modification of internal energy barriers and the correlation between surface charge polarisation and calcium ion motion for the 1,2,3,4-$Ca@C_{60}F_4$ system, albeit at a reduced intensity when compared to the hydrogen functionalised counterpart.

5.2.3 S-Ca@$C_{60}F_6$

DFT geometry optimisation calculations on both singlet and triplet states of S-Ca@$C_{60}F_6$ predict the ground state to be an optimised singlet state with the calcium located -1.40 Å from the centre of the non-functionalised hemisphere, aligned to an off-centre hexagon adjacent to the functionalised site, as shown in the left-hand illustration of figure 5.25. The right-hand illustration shows the off-centre position of the calcium and direction of the dipole, pointing directly towards from the functionalised site. The functionalised site shows a more pronounced cage deformation as a result of the newly created sp^3 bonds at the addition site.

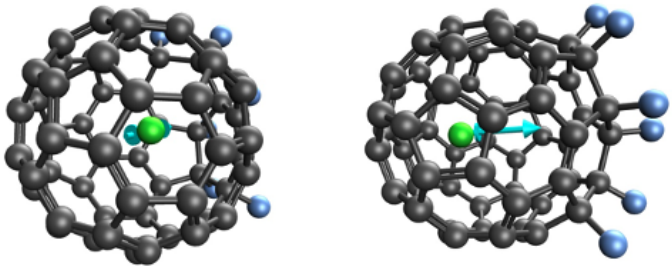

Figure 5.25: The left-hand illustration shows the ground state geometry of S-Ca@$C_{60}F_6$ with calcium aligned to an off-centre hexagon. The RHS illustration shows the same molecule, rotated to visualise the calcium off-centre position, the functionalised site and the resulting dipole (blue arrow).

A translational analysis of DFT single point energies and partial charges can be seen in figure 5.26 showing the impact of functionalisation on the internal potential energy profile and energy barriers between the two minima in each hemisphere.

The addition of F_6 results in the Mexican-hat potential becoming asymmetrical with an energy gap of 0.52 eV between minima, with the global minimum located in the non-functionalised hemisphere. The predicted calcium partial charge at this location is +1.59e, indicating a charge transfer of +0.41e from the cage to the calcium when comparing to the isolated Ca^{2+}

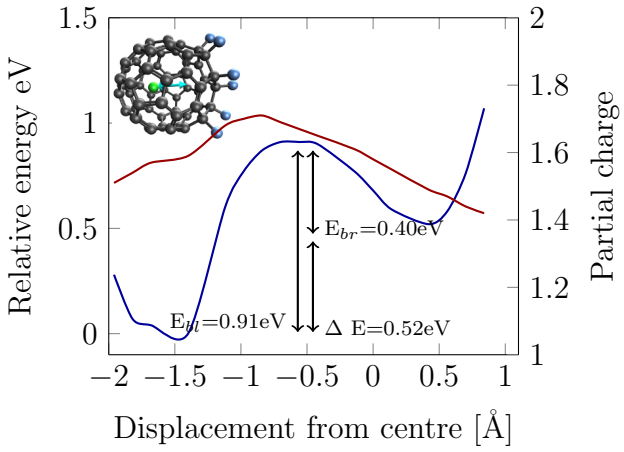

Figure 5.26: S-Ca@$C_{60}F_6$ relative potential energy (blue) as the calcium is displaced towards (RHS) and away from (LHS) the F_6 functionalised site, and corresponding DDEC6 partial charge profile (red) of the calcium ion at the B3P86-D3 / cc-pVDZ level of theory

ion. The maximum energy barrier, 0.91 eV, is shifted -0.56 Å into the left hemisphere. The partial charge profile becomes asymmetrical, with the maximum (+1.67e) also shifting into the non-functionalised hemisphere. The asymmetrical distribution of surface charge can clearly be seen in Figure 5.27.

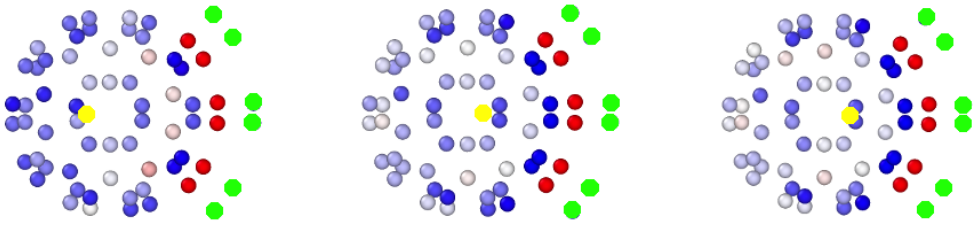

Figure 5.27: Distribution of partial atomic charge for three different positions of the calcium atom (yellow particle inside cage) in S-Ca@$C_{60}F_6$. The lower energy minima (LHS), calcium at the centre (middle), and the higher energy minima (RHS). The carbon atoms are depicted according to the charge they carry: red (positive) and blue (negative). The fluorines are the purple circles outside the cage.

Again, the strongly electronegative fluorine atoms result in the sp^3 carbons being positively charged. When the calcium is at the lowest energy minimum position in the non-functionalised hemisphere, an accumulation of charge is observed in this hemisphere. Similar to 1,2,3,4-Ca@$C_{60}F_4$, at this

position, a ring of marginally positively charged carbon can be seen on the cage next to the sp^3 carbons, again indicating that the sp^3 carbons attract nearby surface charge. As the calcium moves to the centre of the cage, the surface charge distributes into the right-hand hemisphere, rather than evenly distributed, likely as a result of the positively charged sp^3 carbons attracting surface charge as the calcium moves towards the functionalised site. In fact, when the calcium moves into the functionalised hemisphere, to the higher energy minima position, the difference in surface charge distribution compared to the central position is negligible, as the higher energy minima is relatively close to the central position. To understand this motion further, the surface polarisation charge on each hemisphere was plotted as a function of the position of the calcium ion:

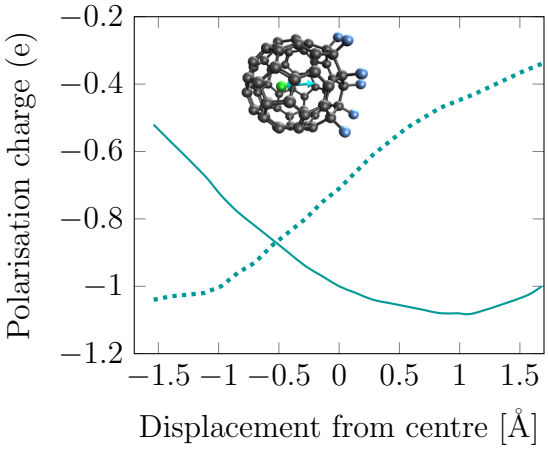

Figure 5.28: Polarisation charge located on the left hemisphere (dotted line) and right hemisphere (smooth line) of the fullerene cage in S-Ca@$C_{60}F_6$ as a function of the position of the calcium ion. The results of the right hemisphere include contributions from the six fluorines.

The polarisation charge in each hemisphere is negative for all radial positions of calcium. Focusing on the left-hemisphere (dotted line), at the lowest energy minimum, where the calcium is displaced -1.40Å from the cage centre, the polarisation charge is -1.03e with net charge transfer being S-$Ca^{1.59+}$@$C_{60}^{1.59-}F_6$. As the calcium moves to the energy maximum, the polarisation charge reduces slightly to -0.87e with net charge transfer

being S-$Ca^{1.67+}@C_{60}^{1.67-}F_6$. As the calcium moves into the functionalised (RHS) hemisphere to the energy minimum at 0.42Å from the cage centre, the polarisation charge reduces further to -0.57e with net charge transfer being S-$Ca^{1.49+}@C_{60}^{1.49-}F_6$. Therefore, as the calcium moves between the two energy minima, the charge switches by approximately 0.46e. This asymmetrical distribution of surface charge as the calcium moves across the molecule clearly demonstrates both the modification of internal energy barriers and the correlation between surface charge polarisation and calcium ion motion for the S-Ca@$C_{60}F_6$ system, albeit again at a reduced intensity when compared to hydrogen.

5.2.4 T-Ca@$C_{60}F_8$

DFT geometry optimisation calculations on both singlet and triplet states of T-Ca@$C_{60}F_8$ predict the ground state to be an optimised singlet state with the calcium located -1.59 Å from the centre of the non-functionalised hemisphere, aligned to an off-centre hexagon adjacent to the functionalised site, as shown in the left-hand illustration of figure 5.29. The right-hand illustration shows the off-centre position of the calcium and direction of the dipole, pointing directly towards the functionalised site. The functionalised site shows a more pronounced cage deformation as a result of the newly created sp^3 bonds at the addition site.

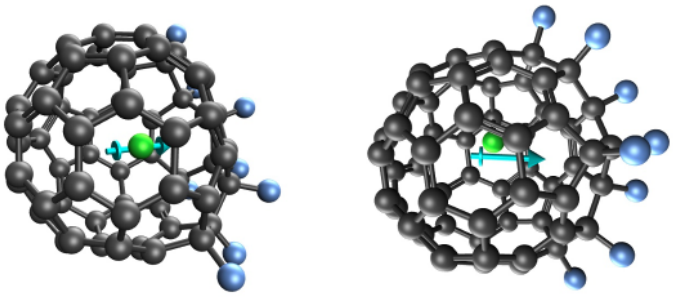

Figure 5.29: The left-hand illustration shows the ground state geometry of T-Ca@$C_{60}F_8$ with calcium aligned to an off-centre hexagon. The RHS illustration shows the same molecule, rotated to visualise the calcium off-centre position, the functionalised site and the resulting dipole (blue arrow).

A translational analysis of DFT single point energies and partial charges can be seen in figure 5.30 showing the impact of functionalisation on the internal potential energy profile and energy barriers between the two minima in each hemisphere.

The addition of F_8 results in the Mexican-hat potential becoming asymmetrical with an energy gap of 0.12 eV between minima, with the global minimum located in the non-functionalised hemisphere. The predicted calcium partial charge at this location is +1.54e, indicating a charge transfer of +0.46e from the cage to the calcium when comparing to the isolated Ca^{2+}

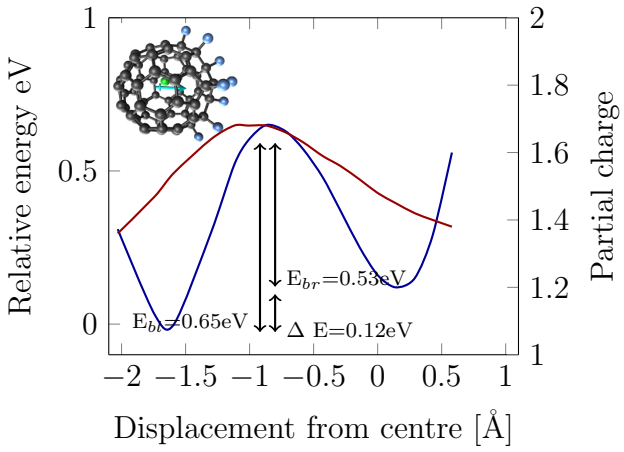

Figure 5.30: T-Ca@$C_{60}F_8$ relative potential energy (blue) as the calcium is displaced towards (RHS) and away from (LHS) the F_8 functionalised site, and corresponding DDEC6 partial charge profile (red) of the calcium ion at the B3P86-D3 / cc-pVDZ level of theory

ion. The maximum energy barrier, 0.65 eV, is shifted -0.87 Å into the left hemisphere. The partial charge profile becomes asymmetrical, with the maximum (+1.68e) also shifting into the non-functionalised hemisphere. The asymmetrical distribution of surface charge can clearly be seen in figure 5.31.

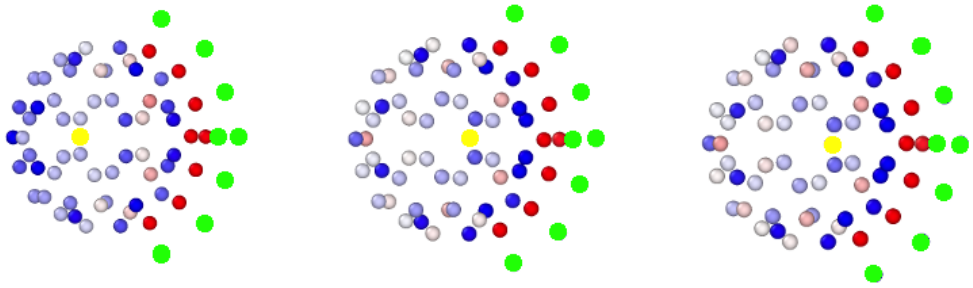

Figure 5.31: Distribution of partial atomic charge for three different positions of the calcium atom (yellow particle inside cage) in T-Ca@$C_{60}F_8$. The lower energy minima (LHS), calcium at the centre (middle), and the higher energy minima (RHS). The carbon atoms are depicted according to the charge they carry: red (positive) and blue (negative). The fluorines are the green circles outside the cage.

Again, the strongly electronegative fluorine atoms result in the sp^3 carbons being positively charged. When the calcium is at the lowest energy minimum position in the non-functionalised hemisphere, an accumulation of

charge is observed in this hemisphere. Similar to the preceding fluorinated molecules, at this position, a ring of marginally positively charged carbon can be seen on the cage next to the sp^3 carbons, again indicating that these positively charged carbons attract nearby surface charge. As the calcium moves to the centre of the cage, the surface charge distributes into the right-hand hemisphere, rather than evenly distributed, likely as a result of the positively charged sp^3 carbons attracting surface charge as the calcium moves towards the functionalised site. When the calcium moves into the functionalised hemisphere, to the higher energy minimum position, the difference in surface charge distribution compared to the central position is negligible, as the higher energy minimum is again relatively close to the central position. To understand this motion further, the surface polarisation charge on each hemisphere was plotted as a function of the position of the calcium ion:

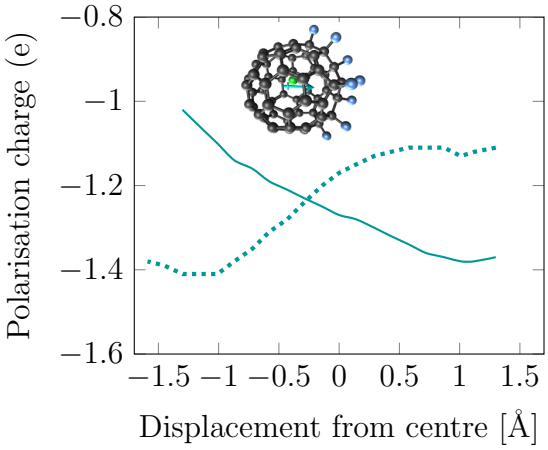

Figure 5.32: Polarisation charge located on the left hemisphere (dotted line) and right hemisphere (smooth line) of the fullerene cage in T-Ca@$C_{60}F_8$ as a function of the position of the calcium ion. The results of the right hemisphere include contributions from the eight fluorines.

The polarisation charge in each hemisphere is negative for all radial positions of calcium. Focusing on the left-hemisphere (dotted line), at the lowest energy minimum, where the calcium is displaced -1.59Å from the cage centre, the polarisation charge is -1.38e with net charge transfer be-

ing T-$Ca^{1.54+}@C_{60}^{1.54-}F_8$. As the calcium moves to the energy maximum, the polarisation charge remains at -1.38e with net charge transfer being T-$Ca^{1.68+}@C_{60}^{1.68-}F_8$. As the calcium moves into the functionalised (RHS) hemisphere to the energy minimum at 0.14Å from the cage centre, the polarisation charge reduces further to -1.15e with net charge transfer being T-$Ca^{1.45+}@C_{60}^{1.45-}F_8$. Therefore, as the calcium moves between the two energy minima, the charge switches by approximately 0.23e. This asymmetrical distribution of surface charge as the calcium moves across the molecule clearly demonstrates both the modification of internal energy barriers and the correlation between surface charge polarisation and calcium ion motion for the T-$Ca@C_{60}F_8$ system, albeit again at a reduced intensity when compared to hydrogen functionalisation.

5.2.5 Formation energy: Fluorine functionalisation

The DFT calculations provide information on the energy required to break the sp^2 hybridised C=C bond and form two sp^3 hybridised C-H bonds. The first four fluorine additions to $Ca@C_{60}$ (F_2, F_4, F_6 and F_8) reduce the ground state energy linearly by 5,434.10 eV. The energy to break the sp^2 hybridised C=C bond and form two sp^3 hybridised C-F bonds can be described by the following equation:

$$\begin{gathered} Ca@C_{60}F_n + F_2 \rightarrow Ca@C_{60}F_{n+2} \\ \Delta E_{F-F} = F_2 - 2F \\ \Delta E_{2C-F} = Ca@C_{60}F_{n+2} - Ca@C_{60}F_n - F_2 \end{gathered} \tag{5.3}$$

A DFT calculation was performed to determine the ground state energy of F_2 at the B3P86 / cc-pVDZ level of theory yields an energy of -5,429.32 eV. Therefore, the energy to break the sp^2 hybridised C=C bond and form two sp^3 hybridised C-F bonds is:

$$\Delta E_{2C-F} = -5,434.10 \text{ eV} - (-5,429.32 \text{ eV}) = -4.78 \text{ eV} \tag{5.4}$$

The net energy lost by the system when forming each sp^3 hybridised C-F bond from the sp^2 hybridised C=C is -2.39 eV, indicating an energetically favourable process.

5.3 Comparing functionalised Ca@C_{60} polarisation properties

The calculations in the preceding sections demonstrate how the internal energy barriers are modified by selected hydrogenation and fluorination, and also how the calcium partial charge and surface polarisation charge change as the calcium moves from the left (non-functionalised) to the right (functionalised) hemispheres of these molecules. The energy and surface charge polarisation of all molecules are visualised together in figures 5.33 and 5.34 respectively, to better understand the impact of increased functionalisation and electronegativity across both molecular series and help inform potential polarisation switch candidates.

Both hydrogenation and fluorination cause the internal energy barriers to shift into the left hemisphere, increasing to a maximum of -0.3 Å for T-Ca@$C_{60}H_8$ and -0.87 Å for T-Ca@$C_{60}F_8$, and shifting the global minimum positions by similar amounts. The energy gaps created by hydrogen and fluorine functionalisation are 0.30 eV - 0.51 eV and 0.12 eV - 0.52 eV respectively, with increasing functionalisation showing a similar trend across molecules. In general, there is a greater variation of energy barrier positions and magnitudes between fluorinated molecules compared to hydrogenated molecules. As observed in the preceding section, fluorination results in positively charged sp^3 addition sites compared to negative sites for hydrogenation - this additional component appears to impact the surface charge distribution and overall electrostatics of the system that create the internal energy barriers in a more complex way compared to the hydrogenated molecules.

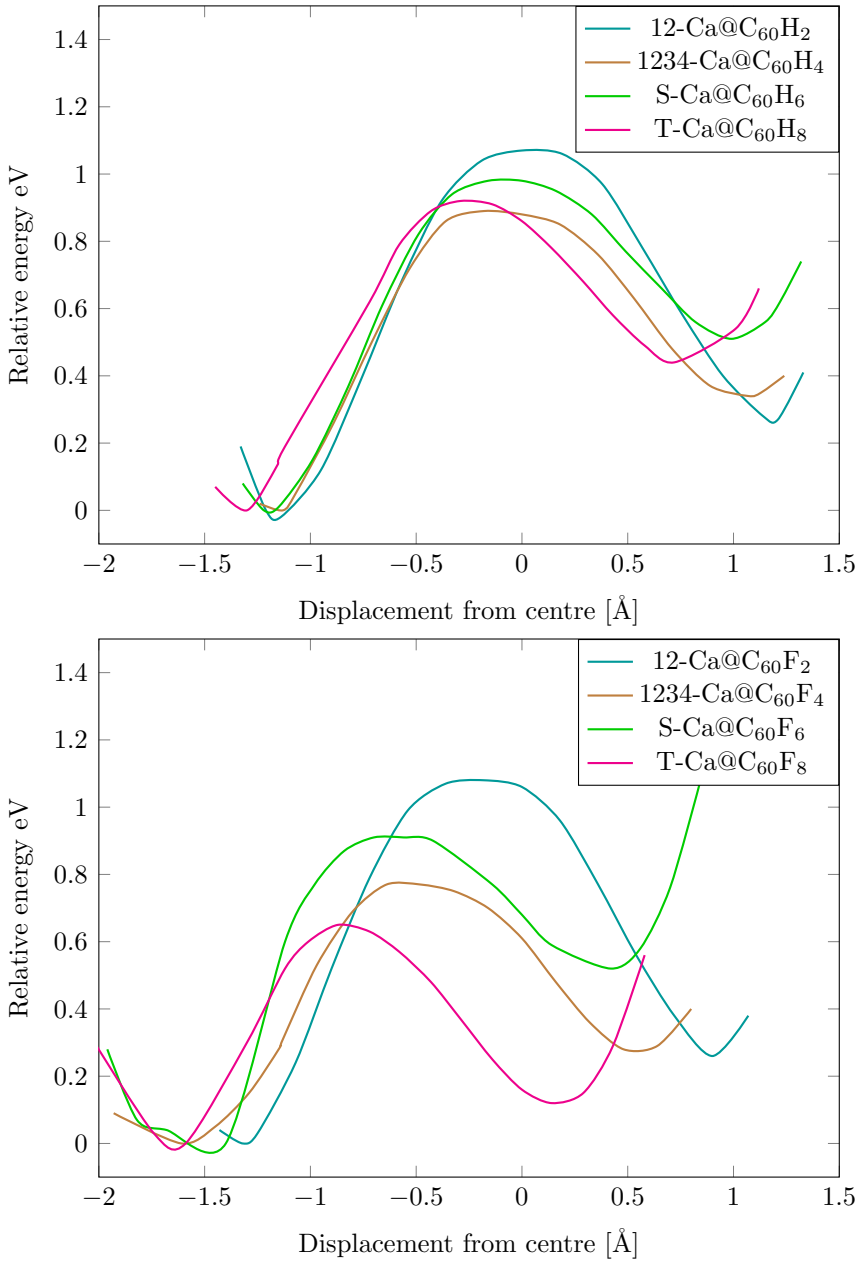

Figure 5.33: Relative energies of the selected hydrogenated and fluorinated $Ca@C_{60}$ molecules as the calcium is displaced towards (LHS) and away from (RHS) the hydrogenated sites. Note that the y-axis is relative to each molecule, and not to the group of molecules as a whole, due to the significant energy difference between each molecule.

This complexity is also observed in the surface charge polarisation of the fluorinated molecules with relatively large variations between the total amount of charge transferred from the left to right hemisphere (0.23e - 0.51e) as well as the position at which the polarisation charge is equally distributed across the cage (line intersection). This in contrast to the hydrogenated series, possessing a similar degree of charge switching (0.6e), with only slight variations around the point at which the surface charge polarisation is equally distributed across hemispheres.

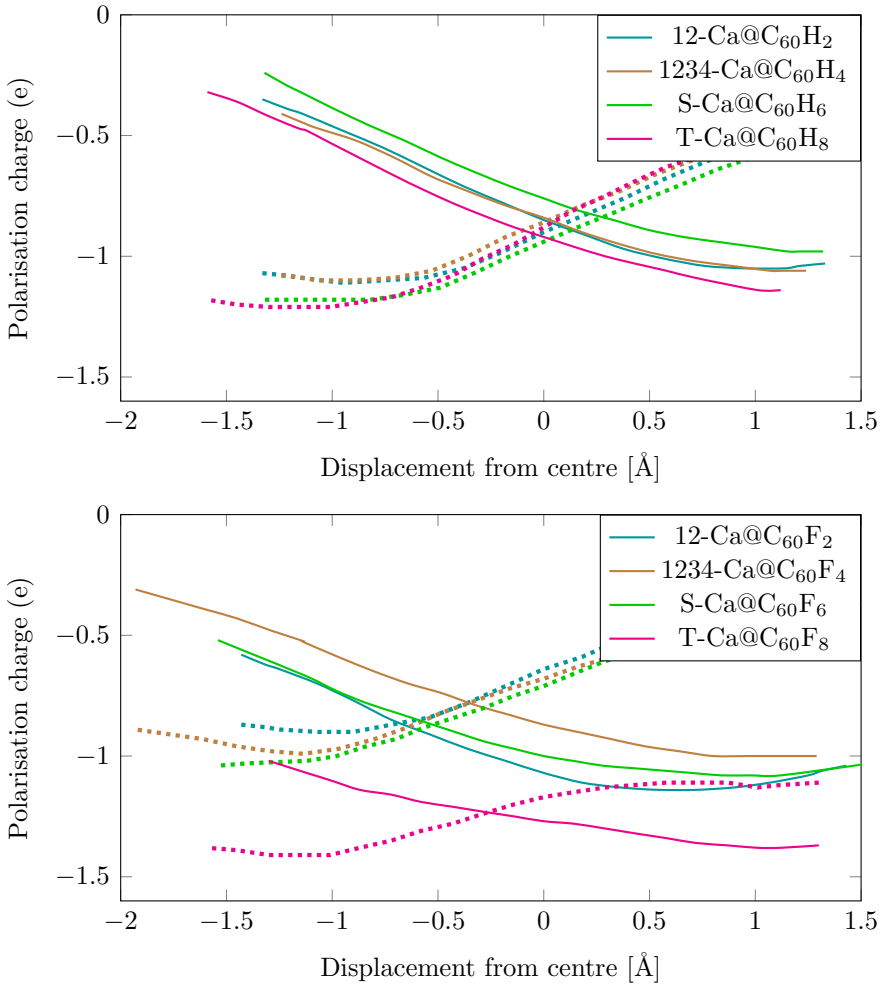

Figure 5.34: Surface charge polarisation on separate hemispheres of the fullerene cage for selected hydrogenated and fluorinated $Ca@C_{60}$ molecules as a function of the position of calcium. The dotted line shows the left hemisphere and the smooth line the right hemisphere. Results for the right hemisphere include contributions from the hydrogen and fluorine atoms respectively.

The calcium partial charge on the selected hydrogenated and fluorinated $Ca@C_{60}$ molecules as the calcium moves across the cage can be seen in Figure 5.35.

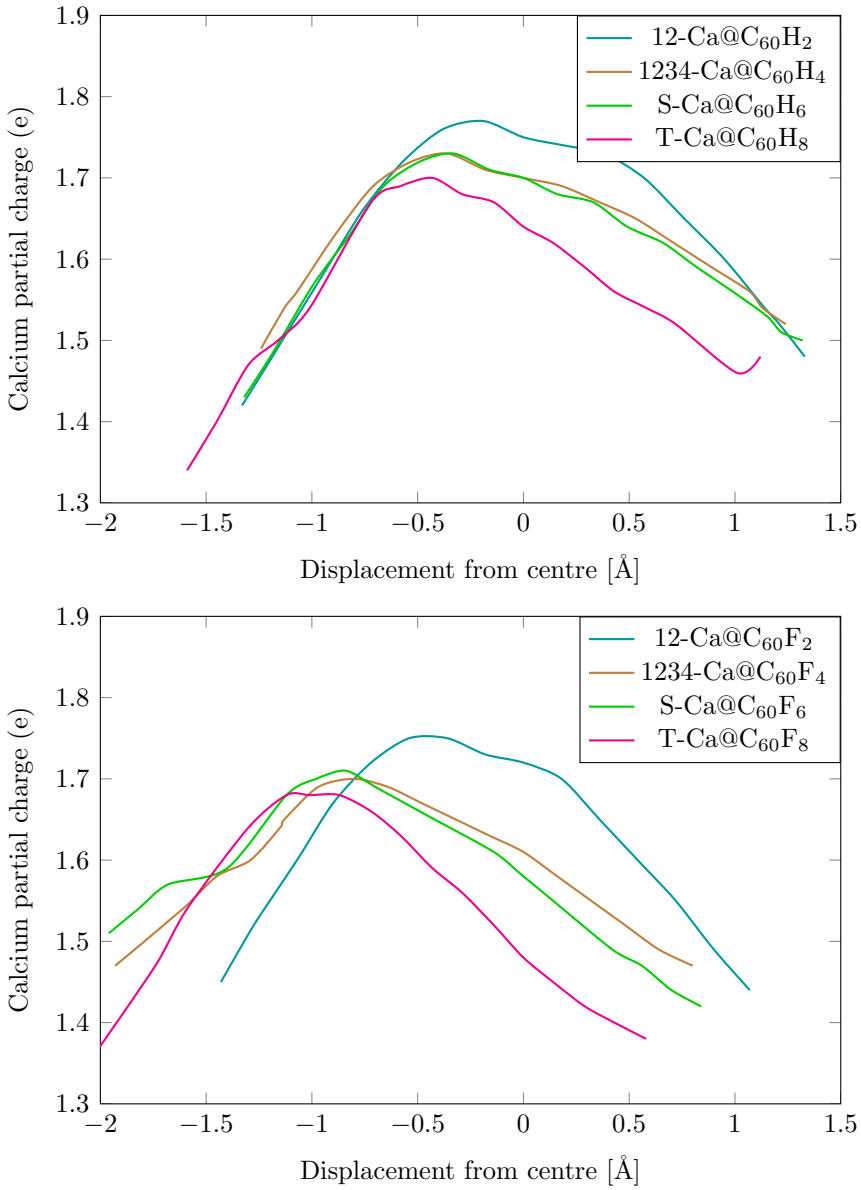

Figure 5.35: Calcium partial charge on the selected hydrogenated and fluorinated $Ca@C_{60}$ molecules as the calcium is displaced towards (LHS) and away from (RHS) the hydrogenated sites.

Across both series, the maximum partial charge on the calcium ion decrease as functionalisation increases with the position of the maximum shifting further into the left hemisphere as more hydrogen and fluorine atoms are added to the cage, reflecting a similar pattern observed for the

internal energy barriers. Interestingly, the partial charges are very similar in the left-hand hemisphere across hydrogenated molecules, compared to a greater spread of partial charges in fluorinated molecules. When the calcium moves into the right hemisphere, increasing functionalisation results in less charge transferred to the cage, indicating that the charge transfer process is linked to the proximity and availability of charge accepting sites. This makes sense given that the increasing number of sp^3 hybrid carbon sites in the functionalised hemisphere are less electronegative and therefore less electron accepting compared to sp^2 hybrids.

The extensive analysis of internal energy barriers and surface charge polarisation undertaken in this chapter so far provides a robust foundation to make candidate selections for a potential polarisation molecular switch. In order to do so, initial switch design parameters need to be considered - these parameters provide the criteria to measure potential switch viability for a single unit molecular switch. Following this, should the desire be to scale-up such a switch into a larger switching system, nanoparticle lattice formation is discussed for $Ca@C_{60}$ and alternative endohedral fullerenes.

5.4 Recommendations for a polarisation switch

The primary goal for the design of a feasible endohedral fullerene polarisation switch is the accurate measurement of a clearly defined change in surface charge polarisation as a result of toggling between two bi-stable states. The selected hydrogenated and fluorinated $Ca@C_{60}$ molecules have all demonstrated that the precise motion of the encapsulated ion corresponds to a shift in surface charge density, in the direction of calcium motion. At the ground state minima positions, this corresponds to two distinct polarisation states of the endohedral fullerene that could be measured if the fullerene was tethered or fixed in place, to ensure any molecular rotation was removed, thus enabling a polarisation measurement to take place.

There are three initial parameters to consider. Firstly, that the preparation of the relevant isomer of the functionalised endohedral fullerenes can be achieved with high yield and purity, so that there is certainty that the correct isomer is isolated. Secondly, that the internal energy barriers, modified through functionalisation, must create bi-stable states that are sufficiently high to hold the calcium in place so that a polarisation measurement on the fullerene cage surface can take place. In the authors' opinion, there is also a benefit to ensuring that such a measurement can take place at room-temperature, to minimise any cooling apparatus required (and therefore minimising costs) should the polarisation switch be fabricated. Finally, that the functionalised species does not distort or weaken the polarisation measurement.

Considering the fluorinated molecules first. All isomers have been shown to be produced with very high yield and purity. Functionalisation modifies the energy barriers such that the energy gap is between 0.12 eV (T-$Ca@C_{60}F_8$)

and 0.52 eV (S-Ca@$C_{60}F_6$) with 1,2-Ca@$C_{60}F_2$ and 1,2,3,4-Ca@$C_{60}F_4$ sitting within this range. However, greater functionalisation leads to a greater shift in the energy barriers into the left-hand hemisphere. This was clearly observed for 1,2,3,4-Ca@$C_{60}F_4$, S-Ca@$C_{60}F_6$ and T-Ca@$C_{60}F_8$ where the secondary minima were relatively close to the centre of the fullerene cage. The overall change in surface charge polarisation for the fluorinated series ranged from 0.51e (1,2-Ca@$C_{60}F_2$) to 0.23e (T-Ca@$C_{60}F_8$), however, the creation of positively charged sp^3 addition sites appear to add an attractive component to the overall electrostatics, attracting the surface charge in the wrong direction for switching purposes, and potentially weakening the effect of the calcium ion's interaction with the surface charge.

Taking all of these factors into account, 1,2-Ca@$C_{60}F_2$ is the only candidate that satisfies the defined switching criteria - a high yield / pure functionalised endohedral fullerene with a sufficient and minimally shifted energy barrier and energy gap between minima that leads to a clearly defined change in surface charge polarisation as calcium moves from the left to right hemispheres. A limitation of this fluorine functionalised endohedral fullerene is the potential distortion of a polarisation measurement due to the position of the negatively charged fluorine atoms on the fullerene cage - the chosen measurement device would need to be calibrated to take into account the negative charge residing on the fluorine atoms, which in the author's view adds complication to such a measurement process.

Now, considering the hydrogenated molecules. Currently, only 1,2-$C_{60}H_2$ can be currently produced in high yield and purity (>99%) [118]. Functionalisation modifies the energy barriers such that the energy gap is between 0.30 eV (1,2-Ca@$C_{60}H_2$) and 0.51 eV (S-Ca@$C_{60}H_6$) with 1,2,3,4-Ca@$C_{60}H_4$ and T-Ca@$C_{60}H_8$ sitting within this range. Greater functionalisation leads to only slight shifts in energy barriers into the non-functionalised

hemisphere and so both minima are located at a reasonable distance away from the centre of the fullerene cage, ensuring that the redistribution of surface charge due to calcium motion is clearly distinguishable between hemispheres. The overall change in surface charge polarisation for the hydrogenated series was consistently 0.60e ± 0.02e, demonstrating that a greater degree of hydrogenation had little effect on the change in polarisation charge as the calcium moved between hemispheres. This appears to be due to the sp^3 hybridised addition sites being negatively charged and so not distorting the motion of redistributing surface charge as the calcium moves.

Based on these factors, hydrogenated $Ca@C_{60}$ appears better suited for a polarisation switch compared to fluorinated $Ca@C_{60}$. However, the yield / purity requirement to produce such a polarisation switch indicates that only 1,2-$Ca@C_{60}H_2$ fully satisfies the defined switching criteria. Again, there is a potential limitation that the positively charged hydrogens could dampen a polarisation measurement, however, given the charge on hydrogen is +0.09e for 1,2-$Ca@C_{60}H_2$ compared to -0.18e for 1,2-$Ca@C_{60}F_2$, the author feels that this limitation can be overcome with an adequately resolved polarisation measurement device.

In conclusion, 1,2-$Ca@C_{60}H_2$ is considered the most viable choice and recommendation for a realistic polarisation switch given the switching criteria presented. Should a fluorinated molecule be of interest, this research indicates that 1,2-$Ca@C_{60}F_2$ could be a viable choice, however, further work will be required to understand the impact of the more complex surface charge redistribution as a result of the positive sp^3 addition sites on the fullerene cage.

5.5 Discussion: towards a multi-molecular polarisation switch

As discussed in the introduction, whilst interest in designing a single molecule switch is very active, the idea that these switches could be scaled up to multi-molecular switches as part of a larger and more complex switching system is fascinating with potential applications to memory devices and molecular transistors to achieve novel logic gates [1, 17]. Miller et al. (including DFT calculation contributions from this author), used a recent development in the theory of many-body interactions [151] to explore some known characteristics of endohedral fullerenes with a view to determining if they could form new nanolattice structures. Given this study's research and insight into the polarisation charge switching of functionalised $Ca@C_{60}$ through the controlled motion of the encapsulated calcium, there appears no reason why this couldn't be applied to other metals in groups I and II (e.g. M = Li, K, Na, Mg) given similar metallic properties.

Miller's electrostatic model simulated lattices that were represented by collections of non-overlapping charged dielectric spheres that were arranged into one of several selected 3D lattice structures, with two frequently observed binary (AB and AB_2) nanoparticle stoichiometries [47–49], of up to 5,000 particles. The formation of the binary lattice, AB or AB_2, requires there to be two types of endohedral fullerene particle, firstly A, a fullerene with an encapsulated metal atom, such as calcium or lithium, which generally has the effect of ionising the atom and at the same time adding electron density to the cage, well discussed in this thesis. Secondly, and in contrast, the introduction of a fluorine or chlorine atom which removes electron density from the cage and adds negative charge to the endohedral F or Cl atom [37]. An example of a potential lattice would be an AB structure consisting

of unit cells containing $Ca@C_{60}$ paired with $Cl@C_{60}$ with each final nanolattice remaining charge neutral. In principle, each AB pair should experience three separate electrostatic interactions, which are: (i) the charged core of A interacting with the charged core of B; (ii) an interaction between the charged cores and the charged cages; and (iii) an interaction between the charged cage of A and the charged cage of B. However, a range of experimental and theoretical studies have shown that fullerene molecules act as Faraday cages [152–157], which means that entities (other cores and cages) external to a given cage are shielded from any charge contained within the cage, i.e. the metal or halogen core. Therefore, electrostatic interactions in AB and AB_2 systems will be dominated by (iii), interactions between the charges on each A and B cage. Thus, each lattice with, for example, an AB pair in the form of $A@C_{60}{}^{q+}{\cdot}B@C_{60}{}^{q-}$, is treated as a collection of charged, dielectric spheres, for which the electrostatic theory is very well established [99, 151].

The energetics of the range of lattices, consisting of the AB and AB_2 stoichiometries, was explored as a function of the ratio of charge residing on cages associated with separate A and B endohedral $X@C_{60}$ fullerenes. The total interaction energy of each lattice type was determined from calculations on a combination of van der Waals, Coulomb, and charge induced multipolar interactions. The lattice types tested were NaCl, CsCl, ZnS, AlB_2, $MgZn_2$ and $SeAg_2$ shown in Figure 5.36 and coloured to show the difference in negative and positive charge on each particle pair with colour intensity showing regions of enhanced and accumulated charge due to polarisation.

It should be noted that the electrostatic calculations performed in this paper [46] fixed the encapsulated metal and halogen atoms to the centre of the fullerene cages, however, in reality (as demonstrated in this thesis),

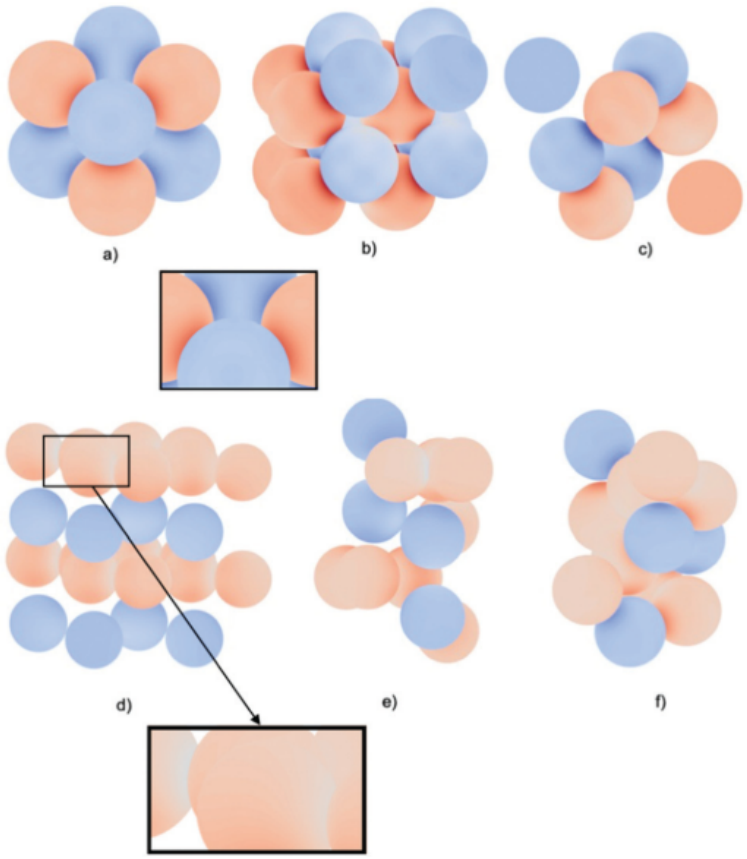

Figure 5.36: Section of each lattice type: (a) NaCl; (b) CsCl; (c) ZnS; (d) AlB_2; (e) $MgZn_2$; (f) $SeAg_2$. Shading on each particle depicts the calculated surface charge as being either negative (blue) or positive (red). Regions of more intense colouration correspond to enhanced charge due to the polarisation of bound charge and are shown in the enlarged images.

the metal would most likely reside in an off-centre position impacting the distribution of partial charge on the fullerene surface. The results presented by Miller et al. demonstrate that the stability of lattice structures are derived, in part, from electrostatic interactions between fullerenes, where the presence of certain endohedral atoms can induce either a negative or positive charge to reside on the cage. For AB and AB_2 structures, varying combinations of Coulomb, charge-induced and van der Waals interactions were shown to contribute to overall stability, and because the latter two interactions always enhance stability, their presence was shown to extend the range of charges over which lattices are stable.

Now considering this as part of a larger-scale switching system, using the knowledge obtained through this thesis's research, it seems conceivable that the proximity of the cation and anion in such a lattice structure would result in the modification of internal potential energies experienced by the encapsulated metal and halogen respectively, similar to how functionalisation directly modifies the internal energy barriers. Figure 5.36 clearly shows that the presence of a negatively charged anion in the lattice pair results in the polarisation of bound charge, asymmetrical distributions of surface charge on each sphere that would likely impact the internal potentials experienced by the encapsulated metal ions. Given the fixed positions of the pairs in the lattice structures, and therefore relatively fixed surface charge polarisation, the application of an electric field similar to the work performed by Foroutan-Nejad et al. [16] could result in measurable shifts in surface charge polarisation across a lattice or array of these molecular pairs. A key factor to consider is whether a change in polarisation, due to any applied stimulus e.g. electric field, would adversely impact the overall stability of the lattice structure. One would assume that a shift in surface charge polarisation will impact the overall electrostatics (van der Waals, Coulomb, and charge induced multipolar interactions), which could result in shifts between lattice arrangements. However, as a first consideration, this is an interesting avenue to explore to see how an endohedral metallofullerene such as $Ca@C_{60}$ could be part of a larger scale polarisation switching system. However, this is outside the scope of this research and therefore should be considered as part of future studies.

Chapter 6

Electrostatic analysis of the surface charge polarisation for a dipole inside an endohedral fullerene

6.1 A dipole within a dielectric sphere

A natural extension to the analytical solution presented in Chapter 3 is the derivation of an analytical solution for a dipole inside an endohedral fullerene. The geometric representation of a dipole within a dielectric sphere can be seen in figure 6.1.

Following the same methodology as section 3.2, the general solutions to the total potential field can be described as a summation of the contributions of the point charge and charged dielectric sphere potentials.

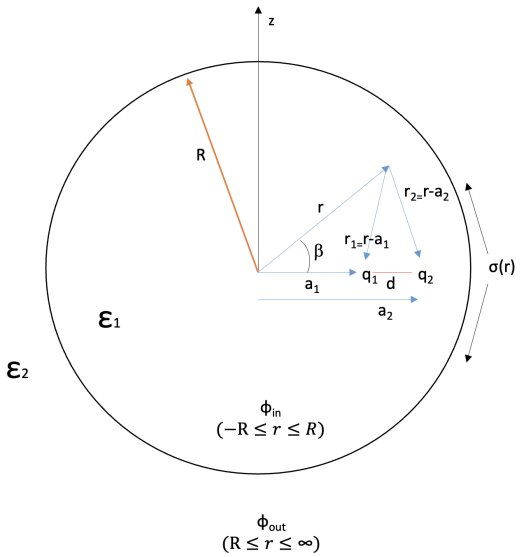

Figure 6.1: Geometric representation of a dipole within a dielectric sphere where $\sigma(r)$ is the surface charge density, $\phi(r)$ is the electric potential, q_1 and q_2 are the encapsulated point charges making up the dipole, R is the radius of the dielectric sphere, a_1 and a_2 are the lengths from the centre separated by a distance d, and r is the observation position.

$$\phi_{in}(r,\beta) = \phi_{q+}(r,\beta) + \phi_{q-}(r,\beta) + \phi_{sphere}(r,\beta)$$

$$\phi_{in}(r,\beta) = \frac{q_1}{4\pi\varepsilon_1 |r-a_1|} + \frac{q_2}{4\pi\varepsilon_1 |r-a_2|} + \sum_{l=0}^{\infty} A_l r^l P_l(cos\beta), \qquad 0 \le r \le R$$

$$\phi_{out}(r,\beta) = \frac{q_1}{4\pi\varepsilon_1 |r-a_1|} + \frac{q_2}{4\pi\varepsilon_1 |r-a_2|} + \sum_{l=0}^{\infty} \frac{B_l}{r^{l+1}} P_l(cos\beta), \qquad R \le r \le \infty \tag{6.1}$$

Expanding the Coulomb potential $\phi_q(r,\beta)$, in terms of Legendre polynomials and simplifying:

$$\phi(r,\beta)=\begin{cases} \frac{q_1}{4\pi\varepsilon_1 a_1}\sum_{l=0}^{\infty}\left(\frac{r}{a_1}\right)^l P_l(cos\beta)+\frac{q_2}{4\pi\varepsilon_1 a_2}\sum_{l=0}^{\infty}\left(\frac{r}{a_2}\right)^l P_l(cos\beta)+\sum_{l=0}^{\infty} A_l r^l P_l(cos\beta) & 0\le r\le a \\ \frac{q_1}{4\pi\varepsilon_1 r}\sum_{l=0}^{\infty}\left(\frac{a_1}{r}\right)^l P_l(cos\beta)+\frac{q_2}{4\pi\varepsilon_1 r}\sum_{l=0}^{\infty}\left(\frac{a_2}{r}\right)^l P_l(cos\beta)+\sum_{l=0}^{\infty} A_l r^l P_l(cos\beta) & a\le r\le R \\ \frac{q_1}{4\pi\varepsilon_1 r}\sum_{l=0}^{\infty}\left(\frac{a_1}{r}\right)^l P_l(cos\beta)+\frac{q_2}{4\pi\varepsilon_1 r}\sum_{l=0}^{\infty}\left(\frac{a_2}{r}\right)^l P_l(cos\beta)+\sum_{l=0}^{\infty} \frac{B_l}{r^{l+1}} P_l(cos\beta) & R\le r\le\infty \end{cases} \tag{6.2}$$

Using the boundary condition that the potentials and the fluxes normal to the spherical boundary are continuous at the boundary (see Chapter 2, Theoretical Methods, for a list of the systems' boundary conditions) and the orthogonality property of Legendre Polynomials, derives expressions for A_l and B_l.

$$\begin{aligned} A_l &= \frac{q_1}{4\pi}\left(\frac{\varepsilon_1-\varepsilon_2}{\varepsilon_1}\right)\left(\frac{l+1}{\varepsilon_2(l+1)+\varepsilon_1 l}\right)\frac{a_1^l}{R^{2l+1}} + \frac{q_2}{4\pi}\left(\frac{\varepsilon_1-\varepsilon_2}{\varepsilon_1}\right)\left(\frac{l+1}{\varepsilon_2(l+1)+\varepsilon_1 l}\right)\frac{a_2^l}{R^{2l+1}} \\ B_l &= \frac{q_1}{4\pi}\left(\frac{\varepsilon_1-\varepsilon_2}{\varepsilon_1}\right)\left(\frac{l+1}{\varepsilon_2(l+1)+\varepsilon_1 l}\right)a_1^l + \frac{q_2}{4\pi}\left(\frac{\varepsilon_1-\varepsilon_2}{\varepsilon_1}\right)\left(\frac{l+1}{\varepsilon_2(l+1)+\varepsilon_1 l}\right)a_2^l \end{aligned} \tag{6.3}$$

Substituting A_l and B_l into Eq. (6.2) leads to complete analytical expressions for the electrostatic potential:

$$\phi(r,\beta) = \begin{cases} \frac{q_1}{4\pi\varepsilon_1 a_1}\sum_{l=0}^{\infty}\left(\frac{r}{a_1}\right)^l P_l(cos\beta) + \frac{q_2}{4\pi\varepsilon_1 a_2}\sum_{l=0}^{\infty}\left(\frac{r}{a_2}\right)^l P_l(cos\beta) + \\ \frac{q_1}{4\pi}\sum_{l=0}^{\infty}\left(\frac{\varepsilon_1-\varepsilon_2}{\varepsilon_1}\right)\left(\frac{l+1}{\varepsilon_2(l+1)+\varepsilon_1 l}\right)\frac{a_1^l r^l}{R^{2l+1}}P_l(cos\beta) + \frac{q_2}{4\pi}\sum_{l=0}^{\infty}\left(\frac{\varepsilon_1-\varepsilon_2}{\varepsilon_1}\right)\left(\frac{l+1}{\varepsilon_2(l+1)+\varepsilon_1 l}\right)\frac{a_2^l r^l}{R^{2l+1}}P_l(cos\beta) & 0\le r\le a \\ \frac{q_1}{4\pi\varepsilon_1 r}\sum_{l=0}^{\infty}\left(\frac{a_1}{r}\right)^l P_l(cos\beta) - \frac{q_2}{4\pi\varepsilon_1 r}\sum_{l=0}^{\infty}\left(\frac{a_2}{r}\right)^l P_l(cos\beta) + \\ \frac{q_1}{4\pi}\sum_{l=0}^{\infty}\left(\frac{\varepsilon_1-\varepsilon_2}{\varepsilon_1}\right)\left(\frac{l+1}{\varepsilon_2(l+1)+\varepsilon_1 l}\right)\frac{a_1^l r^l}{R^{2l+1}}P_l(cos\beta) + \frac{q_2}{4\pi}\sum_{l=0}^{\infty}\left(\frac{\varepsilon_1-\varepsilon_2}{\varepsilon_1}\right)\left(\frac{l+1}{\varepsilon_2(l+1)+\varepsilon_1 l}\right)\frac{a_2^l r^l}{R^{2l+1}}P_l(cos\beta) & a\le r\le R \\ \frac{q_1}{4\pi}\sum_{l=0}^{\infty}\left(\frac{2l+1}{\varepsilon_2(l+1)+\varepsilon_1 l}\right)\frac{a_1^l}{r^{l+1}}P_l(cos\beta) + \frac{q_2}{4\pi}\sum_{l=0}^{\infty}\left(\frac{2l+1}{\varepsilon_2(l+1)+\varepsilon_1 l}\right)\frac{a_2^l}{r^{l+1}}P_l(cos\beta) & R\le r\le\infty \end{cases} \tag{6.4}$$

Simplifying by reducing the Coulomb potential, $\phi_q(r,\beta)$:

$$\phi(r,\beta) = \begin{cases} \frac{q_1}{4\pi\varepsilon_1|r-a_1|} + \frac{q_2}{4\pi\varepsilon_1|r-a_2|} + \frac{q_1}{4\pi}\sum_{l=0}^{\infty}\left(\frac{\varepsilon_1-\varepsilon_2}{\varepsilon_1}\right)\left(\frac{l+1}{\varepsilon_2(l+1)+\varepsilon_1 l}\right)\frac{a_1^l r^l}{R^{2l+1}}P_l(cos\beta) + \\ \frac{q_2}{4\pi}\sum_{l=0}^{\infty}\left(\frac{\varepsilon_1-\varepsilon_2}{\varepsilon_1}\right)\left(\frac{l+1}{\varepsilon_2(l+1)+\varepsilon_1 l}\right)\frac{a_2^l r^l}{R^{2l+1}}P_l(cos\beta) & r\le R \\ \sum_{l=0}^{\infty}\left[\frac{q_1}{4\pi}\left(\frac{2l+1}{\varepsilon_2(l+1)+\varepsilon_1 l}\right)\frac{a_1^l}{r^{l+1}} + \frac{q_2}{4\pi}\left(\frac{2l+1}{\varepsilon_2(l+1)+\varepsilon_1 l}\right)\frac{a_2^l}{r^{l+1}}\right]P_l(cos\beta) & R\le r\le\infty \end{cases} \tag{6.5}$$

Using the boundary condition that the normal component of the electric field is discontinuous due to the presence of a permanent and free charge on the surface of the sphere, an analytical expression for the surface charge density can be derived.

$$\sigma(R,\theta) = -\frac{q_1}{4\pi\left|R-a_1\right|^2} + \frac{q_1}{4\pi}\sum_{l=0}^{\infty}\left(\frac{\varepsilon_1 + l(3\varepsilon_1-\varepsilon_2)}{\varepsilon_1(\varepsilon_2+l(\varepsilon_1+\varepsilon_2)}\right)\frac{a_1^l(l+1)}{R^{l+2}}P_l(cos\beta)$$
$$-\frac{q_2}{4\pi\left|R-a_2\right|^2} + \frac{q_2}{4\pi}\sum_{l=0}^{\infty}\left(\frac{\varepsilon_1 + l(3\varepsilon_1-\varepsilon_2)}{\varepsilon_1(\varepsilon_2+l(\varepsilon_1+\varepsilon_2)}\right)\frac{a_2^l(l+1)}{R^{l+2}}P_l(cos\beta) \tag{6.6}$$

This result could also be derived by inspection as a linear combination of both point charges, given that the encapsulated point charges are separated by a fixed distance (to represent a dipole or linear diatomic molecule rather than two separate free charges), and do not interact. It should be noted that this simplified solution does not consider any rotation of the molecule, which should be taken into account in future research.

6.1.1 DFT validation using q^-q^+@C_{60} and HF@C_{60}

To visualise this analytical expression, the surface charge density was plotted for a geometric system of two point charges, q^+ and q^- separated by a bond length and partial charges calculated by geometry optimisation calculations on HF@C_{60} at the B3P86-D3 / cc-pVDZ level of theory. Note that this level of theory enables a direct comparison to the case of Ca@C_{60} in Chapter 3. However, for future studies it is strongly advised that a full computational parameter validation process is undertaken (similar to section 4.2), with reconciliation to experimentally calculated chemical properties of HF@C_{60} [158–161].

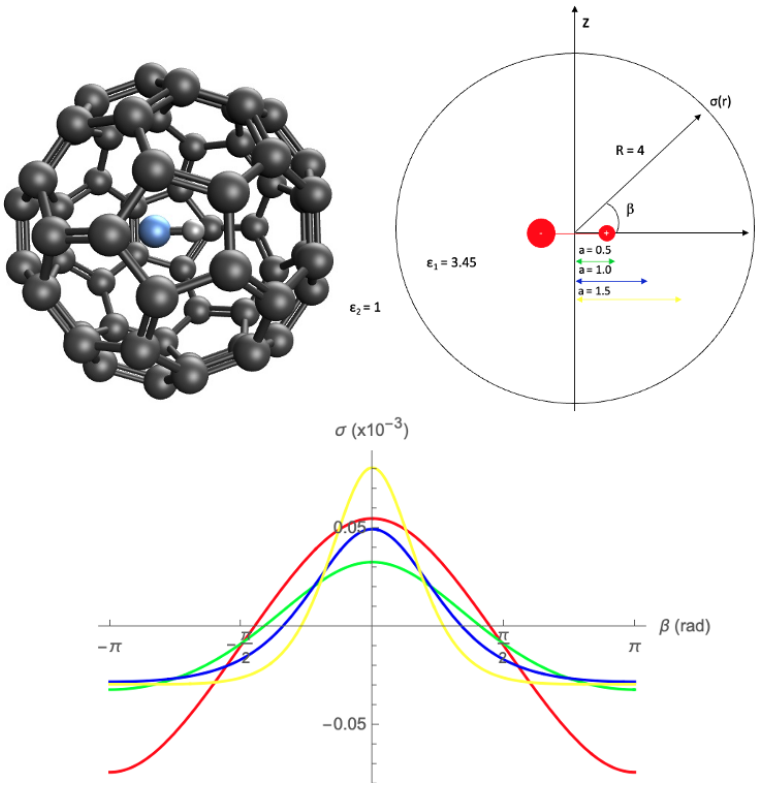

Figure 6.2: The top left illustration shows the optimised geometry of HF@C_{60}, the top right illustration defines the analogous simulated system of $q^{-0.25}q^{+0.25}$@C_{60}, including the angle from the axis of the point charge (β) and the distance of the point charges from the centre (note that only the initial position is shown). The bottom illustration shows the corresponding surface charge distributions for a dipole in a dielectric sphere of radius (R) 4Å and dielectric constant (ϵ_1) 3.45, immersed in a vacuum (ϵ_2=1), through the placement of two point charges, $q^{+0.25}$ and $q^{-0.25}$, separated by a bond length of 0.94Å. The surface charge distribution is plotted as a function of β for various positions of the mid-point of the $q^{-0.25}$-$q^{+0.25}$ dipole: a = 0Å (red), a = 0.5Å (green), a = 1.0Å (blue), and a = 1.5Å (yellow).

Compared to the case of the single point charge within a dielectric sphere, the surface charge density now has two counteracting components. This is best shown at a = 0Å (red line) where the dipole straddles the centre of the cage. The negative point charge repels the surface charge resulting in a positively charged hemisphere, and the positive charge attracts the surface charge into the right-hand hemisphere resulting in a negatively charged hemisphere. This demonstrates that at the centre of the cage, the dielectric sphere is polarised, compared to q@C_{60} where the surface charge density

is distributed evenly when the point charge is located at the centre of the fullerene cage. Geometry optimisation calculations for HF@C_{60} predict HF to straddle the centre of the cage in the ground state, with the fluorine being ever so slightly closer to the cage centre than the hydrogen, reinforcing the view that HF@C_{60} is a naturally polarised molecule.

Interestingly, as the dipole moves fully into the right hemisphere, at a = 0.5Å (green line) and a = 1.0Å (blue line), the degree of polarisation reduces as a result of the counterbalancing electrostatic interaction now occurring in the same hemisphere. It is only when the positive charge gets nearer to the boundary at a = 1.5Å (yellow line) does the surface charge polarisation increase again, as the positive charge is 0.94Å closer to the boundary than the negative charge, demonstrating again the sensitivity of surface charge at close separations to the point charge. However, the presence of the negative charge dampens the surface charge polarisation interaction, compared to the case of the single point charge within a dielectric sphere, resulting in much reduced surface charge density and degree of polarisation (approximately 10% compared to that of the single point charge).

Single point energy DFT calculations were performed using the validated computational parameters identified in chapter 4. The first set of calculations modelled two point charges, $q^{-0.25}$ and $q^{+0.25}$, encapsulated within C_{60}, with the initial central position being $q^{-0.25}$ in the left-hand hemisphere and $q^{+0.25}$ in the right-hand hemisphere (matching the positions in Figure 6.2), to provide a comparable analysis to the analytical model. The resulting output was visualised using the Ovito package [103] with gradient colouring from blue (negative) to red (positive) to clearly visualise the movement of charge across the cage surface.

At a = 0Å with the dipole straddling the cage centre, the molecule is po-

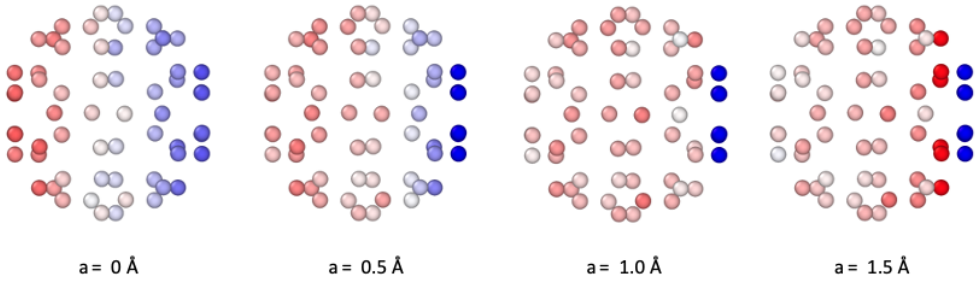

Figure 6.3: DFT calculated partial charges for a dipole inside C_{60}, $q^{-0.25}q^{+0.25}@C_{60}$, at the B3P86-D3 / cc-pVDZ level of theory. The point charges were separated by a fixed distance 0.94Å inside the particle and the midpoint of the dipole placed at various locations (a = 0Å – 1.5Å at 0.5Å intervals), moving from left to right hemispheres in the direction of the carbon 6-6 bond. Note that at a = 0Å the dipole straddles the centre, $q^{-0.25}$ in the left-hand hemisphere and $q^{+0.25}$ in the right-hand hemisphere, with each point charge equidistant from the centre of the fullerene cage.

larised with clear regions of positive charge on the left hemisphere and negative charge on the right hemisphere with a band of relatively neutrally charge carbons around the centre of the fullerene cage. As the dipole is displaced into the right hemisphere, both point charges are now inside the right hemisphere, and consequently the accumulation of negative charge increases due to the positive point charge being 0.94Å closer to the boundary compared to the negative point charge. This charge accumulation occurs across the hexagon (dark blue circles). Interestingly, as the dipole is further displaced at a = 1.0Å and a = 1.5Å the accumulation of negative charge on the hexagon remains similar, however, there is an appearance of a band of strongly positive charge surrounding the hexagon, caused by the negative point charge getting closer to the boundary as shown in figure 6.4:

This behaviour closely matches the analytical solution, the main difference being that the analytical approach does not spread the charge across discrete carbon sites, as the DFT results show, due to the model being of a smooth dielectric sphere. However, for the purposes of establishing whether the analytical approach correctly models behaviour, the close alignment

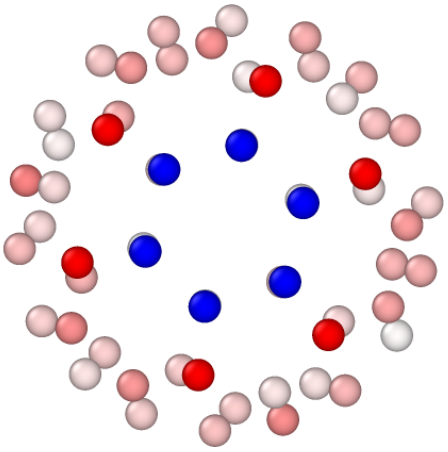

Figure 6.4: DFT calculated partial charges for a dipole inside C_{60}, $q^{-0.25}q^{+0.25}@C_{60}$, at a = 1.5Å, demonstrating the extreme negative and positive charge in the same hemisphere.

with DFT again provides good evidence of the validity of this work's first hypothesis, that the motion of a point charge encapsulated within C_{60} is also correlated to the distribution of charge density on the cage surface.

Taking this one step further, to establish the model's alignment with the endofullerene case, analytical and DFT calculations were undertaken to model $HF@C_{60}$. The main difference with these calculations was the variability of the strength of the H-F charges at different locations of the cage, as a result of the quantity of charge transferred from the H-F to the cage changes depending on the position of the dipole within the fullerene cage.

The analytical solution, in figure 6.5 shows that the unequal opposite charge strength causes subtle differences in curve width compared to figure 6.2 and a slightly reduced degree of polarisation, likely due to the slightly smaller negative charge on the fluorine. The profiles of each curve at the extremities (-π and π) are clustered together with similar surface charge densities, indicating that the surface charge is spread over a larger surface area, rather than being compacted.

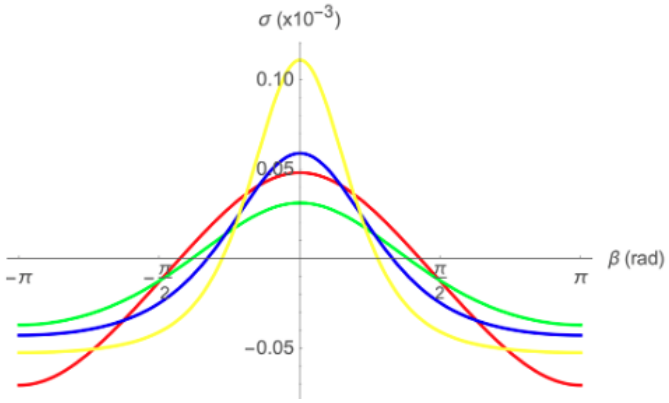

Figure 6.5: Surface charge distributions for a dipole in a dielectric sphere of radius (R) 4Å and dielectric constant (ϵ_1) 3.45, immersed in a vacuum (ϵ_2=1), through the placement of two point charges, separated by a fixed distance of 0.94Å. Corresponding surface charge distributions as a function of β for various positions of the mid-point of the dipole: a = 0Å / $q^{+0.25}q^{-0.21}$ (red), a = 0.5Å / $q^{+0.26}q^{-0.22}$ (green), a = 1.0Å / $q^{+0.28}q^{-0.23}$ (blue), a = 1.5Å / $q^{+0.30}q^{-0.25}$ (yellow).

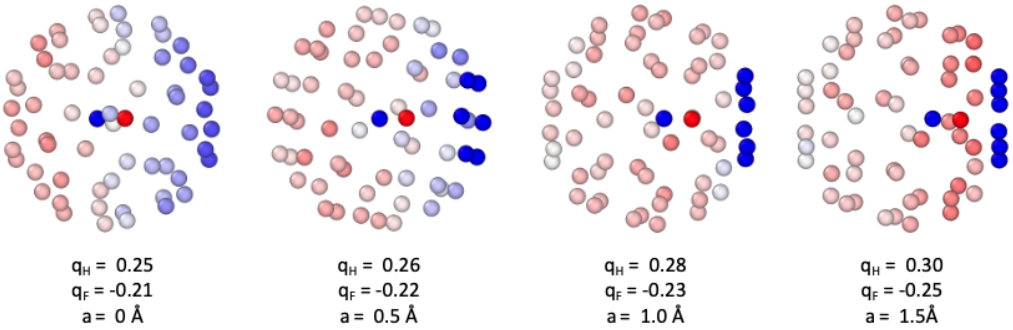

Figure 6.6: DFT derived surface charge distributions of HF@C_{60}, through the placement of H-F inside the particle (using optimised partial charge values), at various locations (a = 0Å - 1.5Å at 0.5Å intervals), moving into the left hemisphere in the direction of the optimised carbon 6-6 bond.

The DFT solution, in figure 6.6 shares similar characteristics to figure 6.3 with a small difference being a less pronounced positively charged ring of carbons surrounding the negatively charged hexagons. This is again likely due to the slightly unequal charges on the HF compared to the equal charges on q^+q^-, however, it is a negligible difference. What is very encouraging is that the DFT partial charge analysis provides good evidence that the analytical solution for a dipole trapped in a dielectric sphere presented is a useful and valid approach to model the surface charge polarisation

behaviour for a broader class of endohedral fullerene.

6.1.2 Discussion: HF@C_{60} as a polarisation switch

The main focus of this thesis was to investigate functionalised Ca@C_{60} as a route to developing a bistable polarisation switch. However, the extension of the electrostatic analytical solution has presented an alternative option, that of a dipole trapped inside C_{60}. HF@C_{70} is already known to possess switching capabilities, through dipole switching due to an applied electric field [16]. In this case, the bistable states were between two rotational minima, whereby each state represents different molecular properties that could be distinguishable via STM or spectroscopic methods e.g. IR or Raman spectroscopy. Given the work presented in this chapter, this switching between the two rotational states should also lead to a switching of polarisation charge density on the fullerene cage, which in turn could be measurable.

In addition and given there is good evidence that this should work for a dipole, there appears to be no reason why this approach could be further extended for the case of a three-body system such as Sc_3N@C_{60} [8] which has also been used as a molecular switch, based on different current-driven rotation orientations of the Sc_3N cluster within the fullerene cage. Based on the work in this thesis, these rotations should also lead to different orientations of "spinning" surface charge density on the fullerene cage surface. This would be a very interesting avenue to explore in future studies.

Chapter 7

Conclusion and Outlook

7.1 Conclusion

Through a combination of classical electrostatic analysis and DFT calculations, this research has validated two hypotheses:

1. That the motion of an encapsulated metal confined within a fullerene cage is strongly correlated to the distribution of charge density on the cage surface.

2. Appropriately selected functionalised endohedral fullerene isomers could form the basis of a polarisation switch.

Firstly, through a rigorous electrostatic analysis of a point charge encapsulated in a dielectric sphere, an analytical solution was presented and described how the surface charge polarisation responds to the precise position of an encapsulated point charge. The analytical solution shows that for a positive point charge, the surface charge "follows" the calcium across the fullerene cage, which enabled a clear demonstration of a switch in sur-

face charge polarisation between hemispheres. The solution was verified using DFT calculations on $Ca@C_{60}$ using computational parameters that were validated against experimental evidence. Partial charge visualisations, using the DDEC6 method, clearly showed a change in surface charge distribution as the calcium moved from the centre of the fullerene cage, where the surface charge density was evenly distributed throughout the cage, to an asymmetrical distribution of charge in one hemisphere as the calcium moved towards the boundary of that hemisphere. These results clearly showed that the motion of an encapsulated metal confined within a fullerene cage is strongly correlated to the distribution of charge density on the cage surface.

Secondly, through a rigorous selection of experimentally produced hydrogenated and fluorinated fullerenes, DFT calculations provided insight into how functionalisation affects the internal potential energy barriers experienced by the encapsulated calcium. In particular, how an energy gap is created between minima in the Mexican-hat potential, asymmetric as a result of functionalisation, and how increasing degrees of functionalisation impacts the position of the energy barriers within the fullerene cage. In addition, a partial charge analysis clearly demonstrated that the motion of encapsulated calcium confined within these functionalised fullerene cages was strongly correlated to the distribution of charge density on the cage surface, with measurements of changes in surface charge polarisation reinforcing these findings.

Thirdly, a consideration of initial switching criteria, enabled the selection of 1,2-$Ca@C_{60}H_2$ as the most promising candidate to develop a polarisation switch – a high yield / pure functionalised endohedral fullerene with a sufficient and minimally shifted energy barrier and energy gap between minima that leads to a clearly defined change in surface charge polarisa-

tion as calcium moves from the left to right hemispheres. It was noted that 1,2-Ca@$C_{60}F_2$ could be considered a viable choice should a fluorinated candidate be preferred, however, with noted limitations regarding a more complex surface charge environment that could impede the movement of surface charge across the fullerene cage, resulting in a more challenging polarisation measurement. A potential route to scalability was discussed, through the creation of stable binary endohedral fullerene lattices that could lead to novel large-scale molecular switching arrays and nanomaterials with novel optical and electronic properties

Finally, given active interest in dipolar endohedral fullerenes, the presented analytical electrostatic solution was extended to the case of a dipole encapsulated within a dielectric sphere to model HF@C_{60}. This demonstrated that a dipolar molecule that straddles the centre of the fullerene cage, such as HF@C_{60} in the ground state, is naturally polarised as a result of the electrostatic interaction between the respective dipole charges and the surface charge density. The solution was also verified using DFT calculations on HF@C_{60}.

7.2 Outlook

Further research should be undertaken to explore the classical electrostatics of a dielectric particle with fixed "patches" of charge on the particle surface, simulating the effect of fixed-site functionalisation. In addition, the extension to dipolar and multi-atomic encapsulated species should be investigated further to understand if these endohedral fullerenes could also be utilised as polarisation switches to compliment the rotation-based switch designs using HF@C_{70} and Sc_3N@C_{60}. The author believes that all the re-

quired electrostatic solutions are currently in the literature (including the analytical solution from this thesis) and that combining these approaches could lead to a greater understanding of the impact of functionalisation on the overall electrostatics of the system. The work undertaken by Miller et al. should also be extended to take into account the reality that encapsulated species within endohedral fullerenes are located off-centre with a corresponding asymmetrical distribution of surface charge density, and how the construction of binary lattice pairs impacts the internal position of the encapsulated cations and anions and the overall stability of different configurations of endohedral nanoparticle lattices.

And finally, 1,2-Ca@$C_{60}H_2$ should be fabricated to test whether the theoretical and computational analysis and predictions in this thesis result in a feasible and commercially viable polarisation switch. This author believes that further study into these particular areas could lead to novel nanomaterials with applications to develop new classes of memory devices, molecular transistors and logic gates.

Appendices

Appendix A

Summary tables

The particular polarisation properties measured using DFT were the position of the minima and maxima (X), the energy barrier from the left-hand (E_{bl}) and right-hand (E_{br}) minima, from which the energy gap (ΔE) is calculated, the partial charge on the calcium at the minima (δ_{Ca}) and the surface charge polarisation (Q). In addition, the molecules ground state multiplicity (M) was predicted between singlet and triple states. A summary of the DFT energy and charge calculations undertaken on these molecules can be seen below, firstly for selected hydrogenated molecules and then for selected fluorinated molecules.

A.1 $Ca@C_{60}H_n$ (n=2,4,6,8)

		Left		Max.	Right		
Molecule	**M**	**X**	$\mathbf{E}_{bl}$	**X**	**X**	$\mathbf{E}_{br}$	Δ**E** ($\mathbf{E}_{bl}$-$\mathbf{E}_{br}$)
1,2-$Ca@C_{60}H_2$	1	-1.14	1.09	0.00	1.14	0.79	0.30
1,2,3,4-$Ca@C_{60}H_4$	1	-1.13	0.89	0.09	1.07	0.55	0.35
S-$Ca@C_{60}H_6$	1	-1.15	0.98	-0.08	0.99	0.47	0.51
T-$Ca@C_{60}H_8$	1	-1.30	0.92	-0.29	0.72	0.48	0.44
$Ca@C_{60}$	1	-1.18	1.56	0.00	1.18	1.56	0.00

Table A.1: Energy barriers and positions of energy minima and maxima for the movement of calcium through the left and right hemispheres of selected hydrogenated $Ca@C_{60}$ molecules. The equivalent data for $Ca@C_{60}$ is also shown. Length units are Å and energy units are eV.

	Left			Max.		Right			
Molecule	**X**	δ_{Ca}	$\mathbf{Q}_l$	**X**	δ_{Ca}	**X**	δ_{Ca}	$\mathbf{Q}_r$	Δ**Q** ($\mathbf{Q}_l$-$\mathbf{Q}_r$)
1,2-$Ca@C_{60}H_2$	-1.14	1.50	-1.09	0.00	1.77	1.14	1.52	-0.48	-0.61
1,2,3,4-$Ca@C_{60}H_4$	-1.13	1.54	-1.09	0.09	1.71	1.07	1.56	-0.48	-0.61
S-$Ca@C_{60}H_6$	-1.15	1.50	-1.18	-0.08	1.73	0.99	1.56	-0.59	-0.59
T-$Ca@C_{60}H_8$	-1.30	1.47	-1.21	-0.29	1.70	0.72	1.52	-0.59	-0.62
$Ca@C_{60}$	-1.18	1.54	-1.11	0.00	1.79	1.18	1.43	-0.31	-0.80

Table A.2: Partial charges, surface charge polarisation, and positions of energy minima and maxima for the movement of calcium through the left and right hemispheres of selected hydrogenated $Ca@C_{60}$ molecules. The equivalent data for $Ca@C_{60}$ is also shown. Length units are Å and charge units are e.

A.2 $Ca@C_{60}F_n$ (n=2,4,6,8)

		Left		Max.	Right		
Molecule	**M**	**X**	$\mathbf{E}_{bl}$	**X**	**X**	$\mathbf{E}_{br}$	$\Delta\mathbf{E}$ ($\mathbf{E}_{bl}$-$\mathbf{E}_{br}$)
1,2-$Ca@C_{60}F_2$	1	-1.32	1.08	-0.18	0.90	0.82	0.26
1,2,3,4-$Ca@C_{60}F_4$	1	-1.61	0.77	-0.56	0.48	0.49	0.28
S-$Ca@C_{60}F_6$	1	-1.40	0.91	-0.56	0.42	0.40	0.52
T-$Ca@C_{60}F_8$	1	-1.59	0.65	-0.87	0.14	0.53	0.12
$Ca@C_{60}$	1	-1.18	1.56	0.00	1.18	1.56	0.00

Table A.3: Energy barriers and positions of energy minima and maxima for the movement of calcium through the left and right hemispheres of selected fluorinated $Ca@C_{60}$ molecules. The equivalent data for $Ca@C_{60}$ is also shown. Length units are Å and energy units are eV.

	Left			Max.		Right			
Molecule	**X**	δ_{Ca}	$\mathbf{Q}_l$	**X**	δ_{Ca}	**X**	δ_{Ca}	$\mathbf{Q}_r$	$\Delta\mathbf{Q}$ ($\mathbf{Q}_l$-$\mathbf{Q}_r$)
1,2-$Ca@C_{60}F_2$	-1.32	1.50	-0.88	0.18	1.73	0.90	1.49	-0.37	-0.51
1,2,3,4-$Ca@C_{60}F_4$	-1.61	1.54	-0.93	-0.56	1.69	0.48	1.52	-0.54	-0.39
S-$Ca@C_{60}F_6$	-1.40	1.59	-1.03	-0.56	1.67	0.42	1.49	-0.57	-0.46
T-$Ca@C_{60}F_8$	-1.59	1.54	-1.38	-0.87	1.68	0.14	1.45	-1.15	-0.23
$Ca@C_{60}$	-1.18	1.54	-1.11	0.00	1.79	1.18	1.43	-0.31	-0.80

Table A.4: Partial charges, surface charge polarisation, and positions of energy minima and maxima for the movement of calcium through the left and right hemispheres of selected hydrogenated $Ca@C_{60}$ molecules. The equivalent data for $Ca@C_{60}$ is also shown. Length units are Å and charge units are e.

Bibliography

(1) H. J. Chandler, M. Stefanou, E. E. B. Campbell and R. Schaub, *Nat. Commun.*, 2019, **10**, 2283.

(2) R. P. Feynman, *J. Microelectromechanical Syst.*, 1992, **1**, 60–66.

(3) N. Taniguchi, Proceeding ICPE, 1974, pp. 18–23.

(4) S. Bayda, M. Adeel, T. Tuccinardi, M. Cordani and F. Rizzolio, *Molecules*, 2019, **25**, 112.

(5) B. L. Feringa, *Angew. Chemie - Int. Ed.*, 2017, **56**, 11060–11078.

(6) E. R. Kay, D. A. Leigh and F. Zerbetto, *Angew. Chemie - Int. Ed.*, 2007, **46**, 72–191.

(7) W. Auwärter, K. Seufert, F. Bischoff, D. Ecija, S. Vijayaraghavan, S. Joshi, F. Klappenberger, N. Samudrala and J. V. Barth, *Nat. Nanotechnol.*, 2012, **7**, 41–46.

(8) T. Huang, J. Zhao, M. Feng, A. A. Popov, S. Yang, L. Dunsch and H. Petek, *Nano Lett*, 2011, **11**, 5327–5332.

(9) D. M. Eigler, C. P. Lutz and W. E. Rudge, *Nature*, 1991, **352**, 600–603.

(10) P. Liljeroth, J. Repp and G. Meyer, *Science*, 2007, **317**, 1203–1206.

(11) Y. Yasutake, Z. Shi, T. Okazaki, H. Shinohara and Y. Majima, *Nano Lett.*, 2005, **5**, 1057–1060.

(12) M. Iwamoto, D. Ogawa, Y. Yasutake, Y. Azuma, H. Umemoto, K. Ohashi, N. Izumi, H. Shinohara and Y. Majima, *J. Phys. Chem. C*, 2010, **114**, 14704–14709.

(13) G. J. Simpson, S. W. Hogan, M. Caffio, C. J. Adams, H. Früchtl, T. Van Mourik and R. Schaub, *Nano Lett.*, 2014, **14**, 634–639.

(14) M. J. Graham, J. M. Zadrozny, M. S. Fataftah and D. E. Freedman, *Chem. Mater.*, 2017, **29**, 1885–1897.

(15) T. Huang, J. Zhao, M. Feng, A. A. Popov, S. Yang, L. Dunsch and H. Petek, *Nano Lett*, 2011, **11**, 5327–5332.

(16) C. Foroutan-Nejad, V. Andrushchenko and M. Straka, *Phys. Chem. Chem. Phys.*, 2016, **18**, 32673–32677.

(17) G. Raggi, A. J. Stace and E. Bichoutskaia, *Phys. Chem. Chem. Phys.*, 2014, **16**, 23869–23873.

(18) W. Harneit, *Phys. Rev. A*, 2002, **65**, 032322.

(19) M. Arndt, O. Nairz, J. Vos-Andreae, C. Keller, G. Van Der Zouw and A. Zellinger, *Nature*, 1999, **401**, 680–682.

(20) H. W. Kroto, J. R. Heath, S. C. O'Brien, R. F. Curl and R. E. Smalley, *Nature*, 1985, **318**, 162–163.

(21) J. R. Heath, S. C. O'Brien, Q. Z. Y. Liu, R. F. Curl, F. K. Tittel, R. E. Smalley and H. W. Kroto, *J. Am. Chem. Soc.*, 1985, **107**, 7779–7780.

(22) W. Krätschmer, L. D. Lamb, K. Fostiropoulos and D. R. Huffman, *Nature*, 1990, **347**, 354–358.

(23) Y. Wang, D. Tománek and R. S. Ruoff, *Chem. Phys. Lett.*, 1993, **208**, 79–85.

(24) A. H. Chang, W. C. Ermler and R. M. Pitzer, *J. Chem. Phys.*, 1991, **94**, 5004–5010.

(25) D. S. Bethune, C. S. Yannoni, M. Hoinkis, M. d. Vries, J. R. Salem, M. S. Crowder and R. D. Johnson, *Zeitschrift für Phys. D Atoms, Mol. Clust.*, 1993, **26**, 153–158.

(26) J. Lu, X. Zhang and X. Zhao, *Solid State Commun.*, 1999, **110**, 565–568.

(27) F. D. Weiss, J. L. Elkind, S. C. O'Brien, R. F. Curl and R. E. Smalley, *J. Am. Chem. Soc.*, 1988, **110**, 4464–4465.

(28) L. M. Roth, Y. Huang, J. T. Schwedler, C. J. Cassady, D. Ben-Amotz, B. Kahr and B. S. Freiser, *J. Am. Chem. Soc.*, 1991, **113**, 6298–6299.

(29) H. Kroto, *Rev. Mod. Phys.*, 1997, **69**, 703–722.

(30) L. Wang, J. Alford, Y. Chai, M. Diener, J. Zhang, S. McClure, T. Guo, G. Scuseria and R. Smalley, *Chem. Phys. Lett.*, 1993, **207**, 354–359.

(31) A. Eilmes and P. Petelenz, *Chem. Phys.*, 1998, **237**, 67–72.

(32) Y. Chen, D. M. Poirier, M. B. Jost, C. Gu, T. R. Ohno, J. L. Martins, J. H. Weaver, L. P. Chibante and R. E. Smalley, *Phys. Rev. B*, 1992, **46**, 7961–7964.

(33) K. Zhang, C. Wang, M. Zhang, Z. Bai, F.-F. Xie, Y.-Z. Tan, Y. Guo, K.-J. Hu, L. Cao, S. Zhang, X. Tu, D. Pan, L. Kang, J. Chen, P. Wu, X. Wang, J. Wang, J. Liu, Y. Song, G. Wang, F. Song, W. Ji, S.-Y. Xie, S.-F. Shi, M. A. Reed and B. Wang, *Nat. Nanotechnol.*, 2020, **15**, 1019–1024.

(34) L.-S. Wang, J. M. Alford, Y. Chai, M. Diener and R. E. Smalley, *Zeitschrift für Phys. D Atoms, Mol. Clust.*, 1993, **26**, 297–299.

(35) G. Raggi, E. Besley and A. J. Stace, *Philos. Trans. R. Soc. A Math. Phys. Eng. Sci.*, 2016, **374**, 20150319.

(36) E. Brocławik and A. Eilmes, *J. Chem. Phys.*, 1998, **108**, 3498–3503.

(37) A. K. Srivastava, S. K. Pandey, A. K. Pandey and N. Misra, *Aust. J. Chem.*, 2018, **71**, 953–956.

(38) A. D. Becke, *Phys. Rev. A*, 1988, **38**, 3098–3100.

(39) C. Lee, W. Yang and R. G. Parr, *Phys. Rev. B*, 1988, **37**, 785–789.

(40) W. J. Hehre, K. Ditchfield and J. A. Pople, *J. Chem. Phys.*, 1972, **56**, 2257–2261.

(41) V. A. Rassolov, M. A. Ratner, J. A. Pople, P. C. Redfern and L. A. Curtiss, *J. Comput. Chem.*, 2001, **22**, 976–984.

(42) R. Ohmukai, M. Watanabe, H. Imajo, K. Hayasaka and S. Urabe, *Jpn. J. Appl. Phys.*, 1994, **33**, 311.

(43) T. Huang, J. Zhao, M. Feng, A. A. Popov, S. Yang, L. Dunsch and H. Petek, *Nano Lett*, 2011, **11**, 5327–5332.

(44) G. Raggi, A. J. Stace and E. Bichoutskaia, *Phys. Chem. Chem. Phys.*, 2013, **15**, 20115–20119.

(45) H. Zettergren, B. O. Forsberg and H. Cederquist, *Phys. Chem. Chem. Phys.*, 2012, **14**, 16360–16364.

(46) A. Miller, M. Halstead, E. Besley and A. J. Stace, *Phys. Chem. Chem. Phys.*, 2022, **24**, 10044–10052.

(47) R. Tan, H. Zhu, C. Cao and O. Chen, *Nanoscale*, 2016, **8**, 9944–9961.

(48) M. A. Boles, M. Engel and D. V. Talapin, *Chem. Rev.*, 2016, **116**, 11220–11289.

(49) A. M. Kalsin, M. Fialkowski, M. Paszewski, S. K. Smoukov, K. J. M. Bishop and B. A. Grzybowski, *Science*, 2006, **312**, 420–424.

(50) M. D. C. Gimenez-Lopez, A. Chuvilin, U. Kaiser and A. N. Khlobystov, *Chem. Commun.*, 2011, **47**, 2116–2118.

(51) In *A Chem. Guid. to Density Funct. Theory*, John Wiley & Sons, Ltd, 2001, ch. 1, pp. 3–18.

(52) D. R. Hartree, *Math. Proc. Cambridge Philos. Soc.*, 1928, **24**, 89–110.

(53) C. Möller and M. S. Plesset, *Phys. Rev.*, 1934, **46**, 618–622.

(54) J. Paldus, *J. Chem. Phys.*, 1974, **61**, 5321–5330.

(55) C. C. J. Roothaan, *Rev. Mod. Phys.*, 1951, **23**, 69–89.

(56) G. G. Hall and J. E. Lennard-Jones, *Proc. R. Soc. London. Ser. A. Math. Phys. Sci.*, 1951, **205**, 541–552.

(57) T. Koopmans, *Physica*, 1934, **1**, 104–113.

(58) In *A Chem. Guid. to Density Funct. Theory*, John Wiley & Sons, Ltd, 2001, ch. 3, pp. 29–32.

(59) P. Hohenberg and W. Kohn, *Phys. Rev.*, 1964, **136**, B864.

(60) S. Lehtola, *Int. J. Quantum Chem.*, 2019, **119**, e25968.

(61) In *A Chem. Guid. to Density Funct. Theory*, John Wiley & Sons, Ltd, 2001, ch. 7, pp. 93–116.

(62) A. Szabo and N. S. Ostlund, *Modern Quantum Chemistry*, Dover Publications, 1996.

(63) W. J. Hehre, R. Ditchfield and J. A. Pople, *J. Chem. Phys.*, 1972, **56**, 2257.

(64) T. H. Dunning, *J. Chem. Phys.*, 1989, **90**, 1007–1023.

(65) In *A Chem. Guid. to Density Funct. Theory*, John Wiley & Sons, Ltd, 2001, ch. 2, pp. 19–28.

(66) V. S. Fain and L. I. Rubanov, *Density Functional Theory for Beginners*, 1995.

(67) In *A Chem. Guid. to Density Funct. Theory*, John Wiley & Sons, Ltd, 2001, ch. 4, pp. 33–40.

(68) S. S. Iyengar, M. Ernzerhof, S. N. Maximoff and G. E. Scuseria, *Phys. Rev. A - At. Mol. Opt. Phys.*, 2001, **63**, 8.

(69) W. Kohn and L. J. Sham, *Phys. Rev.*, 1965, **140**, A1133.

(70) In *A Chem. Guid. to Density Funct. Theory*, John Wiley & Sons, Ltd, 2001, ch. 5, pp. 41–64.

(71) In *A Chem. Guid. to Density Funct. Theory*, John Wiley & Sons, Ltd, 2001, ch. 6, pp. 65–91.

(72) In *A Chem. Guid. to Density Funct. Theory*, John Wiley & Sons, Ltd, 2001, pp. 117–118.

(73) J. P. Perdew, A. Ruzsinszky, J. Tao, V. N. Staroverov, G. E. Scuseria and G. I. Csonka, *J. Chem. Phys.*, 2005, **123**, 62201.

(74) J. P. Perdew and K. Schmidt, *AIP Conf. Proc.*, 2001, **577**, 1–20.

(75) W. Kohn, *Phys. Rev. Lett.*, 1986, **56**, 2219–2220.

(76) G. Ortiz and P. Ballone, *Phys. Rev. B. Condens. Matter*, 1991, **43**, 6376–6387.

(77) J. P. Perdew, K. Burke and M. Ernzerhof, *Phys. Rev. Lett.*, 1996, **77**, 3865–3868.

(78) J. Tao, J. P. Perdew, V. N. Staroverov and G. E. Scuseria, *Phys. Rev. Lett.*, 2003, **91**, 146401.

(79) S. H. Vosko, L. Wilk and M. Nusair, *Can. J. Phys.*, 1980, **58**, 1200–1211.

(80) C. Adamo and V. Barone, *J. Chem. Phys.*, 1999, **110**, 6158–6170.

(81) N. Mardirossian and M. Head-Gordon, *Phys. Chem. Chem. Phys.*, 2014, **16**, 9904–9924.

(82) J. P. Perdew, *Phys. Rev. B*, 1986, **33**, 8822–8824.

(83) Q. Wu and W. Yang, *J. Chem. Phys.*, 2002, **116**, 515–524.

(84) S. Grimme, J. Antony, S. Ehrlich and H. Krieg, *J. Chem. Phys.*, 2010, **132**, 154104.

(85) S. Grimme, L. Goerigk, A. Najibi, A. Hansen, S. Ehrlich and C. Bauer, *Phys. Chem. Chem. Phys.*, 2017, **19**, 32184–32215.

(86) S. Grimme, S. Ehrlich and L. Goerigk, *J. Comput. Chem.*, 2011, **32**, 1456–1465.

(87) J. Gräfenstein and D. Cremer, *Phys. Chem. Chem. Phys.*, 2000, **2**, 2091–2103.

(88) P. Matczak and S. Wojtulewski, *J. Mol. Model.*, 2015, **21**, 1–20.

(89) L. W. Bertels, J. Lee and M. Head-Gordon, *J. Phys. Chem. Lett.*, 2019, **10**, 4170–4176.

(90) D. Stück and M. Head-Gordon, *J. Chem. Phys.*, 2013, **139**, 244109.

(91) J. Lee and M. Head-Gordon, *J. Chem. Theory Comput.*, 2018, **14**, 5203–5219.

(92) C. A. Jime, R. Rodríguez-Guzma and G. E. Scuseria, *J. Phys. Chem. A*, 2014, **118**, 9925–9940.

(93) P. Paul, K. C. Kim, D. Sun, P. D. Boyd and C. A. Reed, *J. Am. Chem. Soc.*, 2002, **124**, 4394–4401.

(94) Y. Shao, Z. Gan, E. Epifanovsky, A. T. Gilbert, M. Wormit, J. Kussmann, A. W. Lange, A. Behn, J. Deng, X. Feng, D. Ghosh, M. Goldey, P. R. Horn, L. D. Jacobson, I. Kaliman, R. Z. Khaliullin, T. Kus, A. Landau, J. Liu, E. I. Proynov, Y. M. Rhee, R. M. Richard, M. A. Rohrdanz, R. P. Steele, E. J. Sundstrom, H. L. Woodcock, P. M. Zimmerman, D. Zuev, B. Albrecht, E. Alguire, B. Austin, G. J. Beran, Y. A. Bernard, E. Berquist, K. Brandhorst, K. B. Bravaya, S. T. Brown, D. Casanova, C. M. Chang, Y. Chen, S. H. Chien, K. D. Closser, D. L. Crittenden, M. Diedenhofen, R. A. Distasio, H. Do, A. D. Dutoi, R. G. Edgar, S. Fatehi, L. Fusti-Molnar, A. Ghysels, A. Golubeva-Zadorozhnaya, J. Gomes, M. W. Hanson-Heine, P. H. Harbach, A. W. Hauser, E. G. Hohenstein, Z. C. Holden, T. C. Jagau, H. Ji, B. Kaduk, K. Khistyaev, J. Kim, J. Kim, R. A. King, P. Klunzinger, D. Kosenkov, T. Kowalczyk, C. M. Krauter, K. U. Lao, A. D. Laurent, K. V. Lawler, S. V. Levchenko, C. Y. Lin, F. Liu, E. Livshits, R. C. Lochan, A. Luenser, P. Manohar, S. F. Manzer, S. P. Mao, N. Mardirossian, A. V. Marenich, S. A. Maurer, N. J. Mayhall, E. Neuscamman, C. M. Oana, R. Olivares-Amaya, D. P. Oneill, J. A. Parkhill, T. M. Perrine, R. Peverati, A. Prociuk, D. R. Rehn, E. Rosta, N. J. Russ, S. M. Sharada, S. Sharma, D. W. Small, A. Sodt, T. Stein, D. Stück, Y. C. Su, A. J. Thom, T. Tsuchimochi, V. Vanovschi, L. Vogt, O. Vydrov, T. Wang, M. A. Watson, J. Wenzel, A. White, C. F. Williams, J. Yang, S. Yeganeh, S. R. Yost, Z. Q. You, I. Y. Zhang, X. Zhang, Y. Zhao, B. R. Brooks, G. K. Chan, D. M. Chipman, C. J. Cramer, W. A. Goddard, M. S. Gordon, W. J. Hehre, A. Klamt, H. F. Schaefer, M. W. Schmidt, C. D. Sherrill, D. G. Truhlar, A. Warshel, X. Xu, A. Aspuru-Guzik, R. Baer, A. T. Bell, N. A. Besley, J. D. Chai, A. Dreuw, B. D. Dunietz, T. R. Furlani,

S. R. Gwaltney, C. P. Hsu, Y. Jung, J. Kong, D. S. Lambrecht, W. Liang, C. Ochsenfeld, V. A. Rassolov, L. V. Slipchenko, J. E. Subotnik, T. Van Voorhis, J. M. Herbert, A. I. Krylov, P. M. Gill and M. Head-Gordon, *Mol. Phys.*, 2015, **113**, 184–215.

(95) J. C. Maxwell, *Philos. Trans. R. Soc. London*, 1865, **155**, 459–512.

(96) C. Pope, *http://people.tamu.edu/ c-pope/EM603/em603.pdf (Accessed on 22.09.2022).*

(97) D. Griffiths, *Introduction to Electrodynamics*, Fourth edition. Boston : Pearson, 2013.

(98) S. Deng and W. Cai, *Commun. Comput. Phys.*, 2007, **2**, 1007–1026.

(99) E. Bichoutskaia, A. L. Boatwright, A. Khachatourian and A. J. Stace, *J. Chem. Phys*, 2010, **133**, 24105.

(100) W. R. Inc., *Mathematica, Version 13.3*, Champaign, IL, 2023.

(101) A. J. Stace, A. L. Boatwright, A. Khachatourian and E. Bichoutskaia, *J. Colloid Interface Sci.*, 2011, **354**, 417–420.

(102) V. V. Batygin, D. t. Haar and I. N. Toptygin, *Problems in Electrodynamics*, ed. D. t. Haar, Academic Press, Pion Limited, 2nd, 1978, p. 38.

(103) A. Stukowski, *Model. Simul. Mater. Sci. Eng.*, 2009, **18**, 15010.

(104) A. V. Filippov, X. Chen, C. Harris, A. J. Stace and E. Besley, *J. Chem. Phys.*, 2019, **151**, 154113.

(105) C. C. Chancey and M. C. M. O'Brien, *The Jahn-Teller Effect in C60 and Other Icosahedral Complexes*, Princeton University Press, 1997.

(106) F. Physik, L.-S. Wang, J. M. Alford, Y. Chai, M. Diener and R. E. Smalley, *Z. Phys, D*, 1993, **26**, 297–299.

(107) R. E. Haufler, J. Conceicao, L. P. Chibante, Y. Chai, N. E. Byrne, S. Flanagan, M. M. Haley, S. C. O'Brien, C. Pan, Z. Xiao, W. E. Billups, M. A. Ciufolini, R. H. Hauge, J. L. Margrave, L. J. Wilson, R. F. Curl and R. E. Smalley, *J. Phys. Chem.*, 1990, **94**, 8634–8636.

(108) C. C. Henderson and P. A. Cahill, *Science*, 1993, **259**, 1885–1887.

(109) C. C. Henderson, C. M. Rohlfing, R. A. Assink and P. A. Cahill, *Angew. Chemie - Int. Ed.*, 1994, **33**, 786–788.

(110) M. S. Meier, B. R. Weedon and H. P. Spielmann, *J. Am. Chem. Soc.*, 1996, **118**, 11682–11683.

(111) P. Birkett, P. Hitchcock, H. Kroto, R. Taylor and D. Walton, *Nature*, 1992, **357**, 479–481.

(112) P. R. Birkett, A. G. Avent, A. D. Darwish, H. W. Kroto, R. Taylor and D. R. Walton, *J. Chem. Soc. Chem. Commun.*, 1993, 1230–1232.

(113) R. G. Bergosh, M. S. Meier, J. A. Laske Cooke, H. Peter Spielmann and B. R. Weedon, *J. Org. Chem.*, 1997, **62**, 7667–7672.

(114) A. A. Gakh, A. Y. Romanovich and A. Bax, *J. Am. Chem. Soc.*, 2003, **125**, 7902–7906.

(115) T. Wågberg, D. Johnels, A. Peera, M. Hedenström, Y. M. Schulga, Y. O. Tsybin, J. M. Purcell, A. G. Marshall, D. Noreus, T. Sato and A. V. Talyzin, *Org. Lett.*, 2005, **7**, 5557–5560.

(116) S. E. Shaheen, C. J. Brabec, N. S. Sariciftci, F. Padinger, T. Fromherz and J. C. Hummelen, *Appl. Phys. Lett.*, 2001, **78**, 841–843.

(117) K. Tokunaga, S. Ohmori, H. Kawabata and K. Matsushige, *Jpn. J. Appl. Phys.*, 2008, **47**, 1089–1093.

(118) M. D. Tzirakis, M. N. Alberti, L. C. Nye, T. Drewello and M. Orfanopoulos, *J. Org. Chem*, 2009, **74**, 5746–5749.

(119) S. M. Luzan, Y. O. Tsybin and A. V. Talyzin, *J. Phys. Chem. C*, 2011, **115**, 11484–11492.

(120) H. P. Spielmann, G.-w. Wang, M. S. Meier and B. R. Weedon, *J. Org. Chem.*, 1998, **63**, 9865–9871.

(121) O. V. Boltalina, A. D. Darwish, J. M. Street, R. Taylor and X.-W. Wei, *J. Chem. Soc., Perkin Trans. 2*, 2002, **2**, 251–256.

(122) A. G. Avent, A. D. Darwish, D. K. Heimbach, H. W. Kroto, M. F. Meidine, J. P. Parsons, C. Remars, R. Roers, O. Ohashi, R. Taylor and D. R. Walton, *J. Chem. Soc. Perkin Trans. 2*, 1994, **2**, 15–22.

(123) A. D. Darwish, A. G. Avent, R. Taylor and D. R. Walton, *J. Chem. Soc. Perkin Trans. 2*, 1996, **10**, 2051–2054.

(124) O. V. Boltalina, M. Bühl, A. Khong, M. Saunders, J. M. Street and R. Taylor, *J. Chem. Soc. Perkin Trans. 2*, 1999, 1475–1479.

(125) A. G. Avent, O. V. Boltalina, A. Y. Lukonin, J. M. Street and R. Taylor, *J. Chem. Soc. Perkin Trans. 2*, 2000, 1359–1361.

(126) O. V. Boltalina, V. Y. Markov, R. Taylor and M. P. Waugh, *Chem. Commun.*, 1996, 2549.

(127) G. Wang, Y. Li, F. Li and Y. Liu, *Lett. Org. Chem.*, 2005, **2**, 595–598.

(128) H. P. Spielmann, B. R. Weedon and M. S. Meier, *J. Org. Chem.*, 2000, **65**, 2755–2758.

(129) P. A. Cahill, *Chem. Phys. Lett.*, 1996, **254**, 257–262.

(130) F. Cataldo and S. Iglesias-Groth, *Fulleranes: The Hydrogenated Fullerenes*, Springer, 2010, p. 278.

(131) J. Lee and M. Head-Gordon, *Phys. Chem. Chem. Phys*, 2019, **21**, 4763.

(132) A. D. Becke, *J. Chem. Phys.*, 1993, **98**, 5648–5652.

(133) H. Kruse, L. Goerigk and S. Grimme, *J. Org. Chem.*, 2012, **77**, 10824–10834.

(134) F. Rastrelli, D. Frezzato, R. G. Lawler, Y. Li, N. J. Turro and A. Bagno, *Philos. Trans. R. Soc. A Math. Phys. Eng. Sci.*, 2013, **371**, 20110634.

(135) V. Filidou, S. Mamone, S. D. Karlen, H. L. Anderson, C. W. M. Kay, A. Bagno, F. Rastrelli, Y. Murata, X. Lei, Y. Li, J. Nicholas, M. H. Levitt, J. J. L. Morton, S. Simmons, K. Sd, A. Hl, A. Bagno, F. Rastrelli and Y. Murata, 2013, **371**, 20120475.

(136) J. Biskupek, S. T. Skowron, C. T. Stoppiello, G. A. Rance, S. Alom, K. L. Fung, R. J. Whitby, M. H. Levitt, Q. M. Ramasse, U. Kaiser, E. Besley and A. N. Khlobystov, *ACS Nano*, 2020, **14**, 11178–11189.

(137) S. Osuna, M. Swart and M. Solà, *J. Phys. Chem. A*, 2011, **115**, 3491–3496.

(138) A. Bauzá, D. Quiñonero, P. M. Deyaì and A. Frontera, *J. Phys. Chem. A*, 2013, **117**, 2651–2655.

(139) D. G. Truhlar, X. Xu, E. Papajak, J. Zheng and H. R. Leverentz, *J. Chem. Theory Comput.*, 2011, **7**, 3027–3034.

(140) N. Treitel, R. Shenhar, I. Aprahamian, T. Sheradsky and M. Rabinovitz, *Phys. Chem. Chem. Phys.*, 2004, **6**, 1113–1121.

(141) H. Yagi, N. Ogasawara, M. Zenki, T. Miyazaki and S. Hino, *Chem. Phys. Lett.*, 2016, **651**, 124–126.

(142) F. Rohmund, A. V. Bulgakov, M. Hedén, A. Lassesson and E. E. Campbell, *Chem. Phys. Lett.*, 2000, **323**, 173–179.

(143) R. S. Mulliken, *J. Chem. Phys.*, 1955, **23**, 1833–1840.

(144) C. M. Breneman and K. B. Wiberg, *J. Comput. Chem.*, 1990, **11**, 361–373.

(145) A. V. Marenich, S. V. Jerome, C. J. Cramer and D. G. Truhlar, *J. Chem. Theory Comput.*, 2012, **8**, 527–541.

(146) D. Vassetti and F. Labat, *Int. J. Quantum Chem.*, 2021, **121**, 1–14.

(147) A. V. Marenich, C. J. Cramer and D. G. Truhlar, *J. Chem. Theory Comput.*, 2013, **9**, 609–620.

(148) L. S. Dodda, J. Z. Vilseck, K. J. Cutrona and W. L. Jorgensen, *J. Chem. Theory Comput.*, 2015, **11**, 4273–4282.

(149) T. A. Manz and N. G. Limas, *RSC Adv.*, 2016, **6**, 47771–47801.

(150) Y. Yamada, A. V. Kuklin, S. Sato, F. Esaka, N. Sumi, C. Zhang, M. Sasaki, E. Kwon, Y. Kasama, P. V. Avramov and S. Sakai, *Carbon*, 2018, **133**, 23–30.

(151) E. B. Lindgren, A. J. Stace, E. Polack, Y. Maday, B. Stamm and E. Besley, *J. Comput. Phys.*, 2018, **371**, 712–731.

(152) B. Pietzak, M. Waiblinger, T. Almeida Murphy, A. Weidinger, M. Höhne, E. Dietel and A. Hirsch, *Chem. Phys. Lett.*, 1997, **279**, 259–263.

(153) P. Delaney and J. C. Greer, *Appl. Phys. Lett.*, 2004, **84**, 431–433.

(154) S. Lo, A. V. Korol and A. V. Solov'Yov, *J. Phys. B At. Mol. Opt. Phys.*, 2007, **40**, 3973–3981.

(155) G. Gao and H. S. Kang, *Chem. Phys. Lett.*, 2008, **462**, 72–74.

(156) A. V. Marenich, C. J. Cramer and D. G. Truhlar, *Chem. Sci.*, 2013, **4**, 2349–2356.

(157) M. Moshinsky, *Chem. Eur. J.*, 2020, **26**, 804–808.

(158) S. Vidal, M. Izquierdo, S. Alom, M. Garcia-Borràs, S. Filippone, S. Osuna, M. Solà, R. J. Whitby and N. Martín, *Chem. Commun.*, 2017, **53**, 10993–10996.

(159) S. P. Jarvis, H. Sang, F. Junqueira, O. Gordon, J. E. Hodgkinson, A. Saywell, P. Rahe, S. Mamone, S. Taylor, A. Sweetman, J. Leaf, D. A. Duncan, T. L. Lee, P. K. Thakur, G. Hoffman, R. J. Whitby, M. H. Levitt, G. Held, L. Kantorovich, P. Moriarty and R. G. Jones, *Commun. Chem.*, 2021, **4**, 1–7.

(160) A. Krachmalnicoff, R. Bounds, S. Mamone, S. Alom, M. Concistrè, B. Meier, K. Kouril, M. E. Light, M. R. Johnson, S. Rols, A. J. Horsewill, A. Shugai, U. Nagel, T. Rõõm, M. Carravetta, M. H. Levitt and R. J. Whitby, *Nat. Chem.*, 2016, **8**, 953–957.

(161) J. Biskupek, S. T. Skowron, C. T. Stoppiello, G. A. Rance, S. Alom, K. L. Fung, R. J. Whitby, M. H. Levitt, Q. M. Ramasse, U. Kaiser, E. Besley and A. N. Khlobystov, *ACS Nano*, 2020, **14**, 11178–11189.